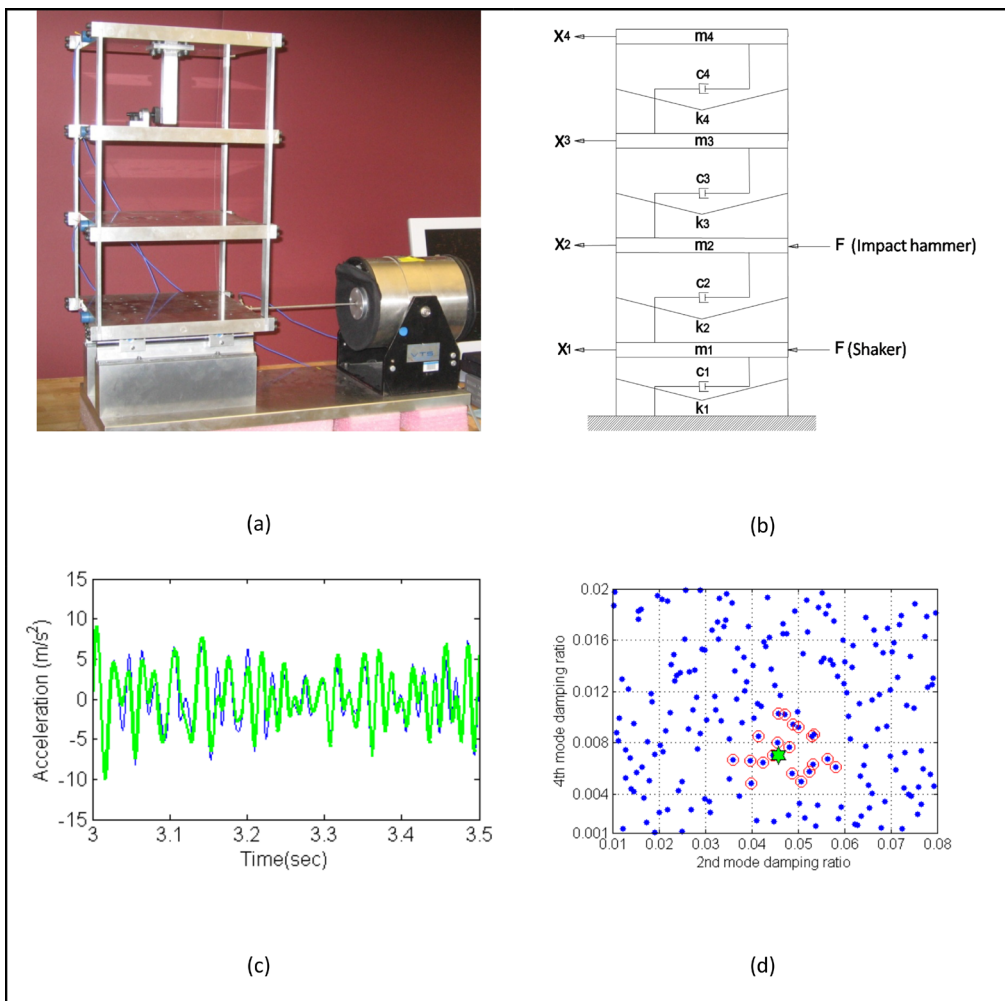


LA-14489

Approved for public release;
distribution is unlimited.

Feature Extraction for Structural Dynamics Model Validation



About the cover:

- (a) Three-story structure used to demonstrate features that can be used in structural dynamics model verification and validation studies.
- (b) A representation of the three-story structure numerical model.
- (c) A comparison of time-histories measured on the top floor of the structure (blue line) to those calculated with the numerical model (green line). A random excitations was applied to the structure with the shaker and a digital representation of the measured input was used as the excitation source in the numerical simulation.
- (d) Results of a model calibrations study used to identify the best modal damping parameters to use in the numerical model. Blue dots indicate the 200 parameter sets sampled with the Latin hypercube design. Red circles indicate the pairs of damping ratios that yield the lowest twenty RSME values of residual error between the measured and predicted responses. The green star indicates the calibrated damping ratios obtained from a Gaussian Process Model for Simulation Analysis that most accurately reproduces the measured response.

Los Alamos National Laboratory, an Affirmative Action/
Equal Opportunity Employer, is operated by Los Alamos
National Security, LLC, for the National Nuclear Security
Administration of the U.S. Department of Energy under
contract DE-AC52-06NA25396.



This report was prepared as an account of work sponsored by an agency of the U.S. Government. Neither Los Alamos National Security, LLC, the U.S. Government nor any agency thereof, nor any of their employees make any warranty, express or implied, or assume any legal liability or responsibility for the accuracy, completeness, or usefulness of any information, apparatus, product, or process disclosed, or represent that its use would not infringe privately owned rights. Reference herein to any specific commercial product, process, or service by trade name, trademark, manufacturer, or otherwise does not necessarily constitute or imply its endorsement, recommendation, or favoring by Los Alamos National Security, LLC, the U.S. Government, or any agency thereof. The views and opinions of authors expressed herein do not necessarily state or reflect those of Los Alamos National Security, LLC, the U.S. Government, or any agency thereof. Los Alamos National Laboratory strongly supports academic freedom and a researcher's right to publish; as an institution, however, the Laboratory does not endorse the viewpoint of a publication or guarantee its technical correctness.

LA-14489
Issued: May 2016

Enhanced Verification Test Suite for Physics Simulation Codes

Mayuko Nishio, Yokohama National University, Japan
François Hemez, Los Alamos National Laboratory, XTD-IDA
Chris Stull, Los Alamos National Laboratory, AET-6
Charles Farrar, Los Alamos National Laboratory, NSEC
Gyuhae Park, Chonnam National University, South Korea
Phil Cornwell, Rose Hulman Institute of Technology
Elói Figueiredo, Universidade Lusófona, Portugal
D.J. Luscher, Los Alamos National Laboratory, T-3
Keith Worden, University of Sheffield, UK



This page is left blank intentionally.

Table of Contents

1. INTRODUCTION	1
1.1.2 Model Validation Philosophy	2
1.2. What Does It Take To Be Predictive?	3
1.3. The Evolution of Structural Dynamics	4
1.4. Model Updating vs. Model Validation	4
1.5. Research Directions.....	7
Uncertainty Quantification	7
Sampling and Fast Probability Integration	7
Generation of Fast Running Meta-Models	8
Statistical Hypothesis Testing.....	8
Feature Extraction.....	8
1.6. Focus of this Report.....	9
2. FEATURES FOR MODEL VALIDATION AND UNCERTAINTY QUANTIFICATION	10
3. EXPERIMENTAL DATA ACQUISITION	13
3.1. Test-Bed Structure Description.....	13
3.2. Data Acquisition.....	15
4. NUMERICAL MODEL AND CALCULATION.....	18
4.1. Four Degree-of-Freedom Lumped-Mass Model	18
4.2. Numerical Calculations	21
4.3. Overlay of Time-Histories.....	24
4.3.1. Linear System	24
4.3.2. Nonlinear System	26
5. FEATURES FOR STRUCTURAL DYNAMICS MODEL VALIDATION	28
5.1. Modal Properties	29
5.2. Waveform Analysis	31
5.2.1. Basic Statistics.....	32
5.2.2. Normal Probability Plot and Probability Density Distribution.....	35
5.2.3. Crest Factor and K-Factor	39
5.2.4. 10% Duration and Exponential Decaying Function Fitting	40
5.2.5. Temporal Moments	42
5.2.6. Autocorrelation Function and Correlation Coefficient.....	48
5.3. Frequency domain analysis	50
5.3.1. Frequency Response Function and Coherence Function.....	50
5.3.2. Power Spectral Density	55
5.3.3. Response Spectra.....	57

5.3.4.	Cepstrum.....	58
5.3.5.	Holder Exponent.....	60
5.4.	Time Series Analysis.....	63
5.4.1.	Autoregressive Model	63
5.4.2.	Autoregressive with Exogeneous Input Model	71
5.4.3.	AR-ARX Model	74
6.	EXAMPLE OF MODEL VALIDATION USING EXTRACTED FEATURES	77
6.1.	Procedure of Feature Comparison and Uncertainty Analysis	77
6.1.1.	Feature Comparison Using Mahalanobis Distance.....	77
6.1.2.	Uncertainty Analysis of Model Parameters.....	78
6.1.2.1.	Global sensitivity of response features to model parameters	78
6.1.2.2.	Inference uncertainty quantification using the GPM/SA software.....	79
6.2.	Application to the Linear System Model Validation	79
6.2.1.	Experimental Data Sets.....	79
6.2.2.	Numerical Predictions	79
6.2.3.	Feature Extraction and Mahalanobis Distance Calculation.....	82
6.2.4.	Consistency Check of the Mahalanobis Distance Comparison	84
6.2.5.	Uncertainty Analysis and Model Calibration	85
6.2.5.1.	Global sensitivity analysis of response features to the damping ratios	85
6.2.5.2.	Calibration of the damping ratios	87
6.3.	Application to the Nonlinear System Model Validation	92
6.3.1.	Experimental Data and Numerical Runs	92
6.3.2.	Feature Selection and Mahalanobis Distance Comparison	94
7.	CONCLUSIONS	97
8.	BIBLIOGRAPHY	99

List of Figures

Figure 1	Conceptual view of model validation.....	3
Figure 2	Matrix of model validation experiments.	5
Figure 3	Testing configuration of the LANL threaded assembly.	6
Figure 4	Strain responses (sensor 1) for two tests.	6
Figure 5	Eight degree-of-freedom spring-mass system.	10
Figure 6	Measured mode shape and a quadratic approximation obtained by a least squares fit to the measured data.....	11
Figure 7	Set-up of the three-story structure.	13
Figure 8	Basic dimensions of the three-story structure.	14
Figure 9	Structural details used to add nonlinearity.	14
Figure 10	Four DOF shear-building model of the test-bed structure.	19
Figure 11	Force-displacement relation for relative displacement between second and third floors.20	

Figure 12	Time-histories for random excitations applied to the linear system.....	25
Figure 13	Time-histories for chirp excitations applied to the linear system.....	25
Figure 14	Time-histories for harmonic excitations applied to the linear system.....	25
Figure 15	Time-histories for shaker transient excitations applied to the linear system.....	26
Figure 16	Time-histories for impact hammer excitations applied to the linear system.....	26
Figure 17	Time-histories for random excitations applied to the nonlinear system.....	27
Figure 18	Time-histories for chirp excitations applied to the nonlinear system.....	27
Figure 19	Time-histories for harmonic excitations applied to the nonlinear system.....	27
Figure 20	Time-histories for shaker transient excitations applied to the nonlinear system.....	28
Figure 21	Time-histories for impact hammer excitations applied to the nonlinear system.....	28
Figure 22	Comparison of estimated mode shapes from the experimental modal analysis.....	31
Figure 23	MAC comparing mode shapes obtained by the experimental modal analysis.....	31
Figure 24	Extracted peak amplitude, mean, and STD in the random and chirp responses in the linear system.....	33
Figure 25	Basic statistics of random responses from the linear system	34
Figure 26	Basic statistics from random responses in the nonlinear system.....	35
Figure 27	NPPs from the linear system.	37
Figure 28	NPPs from the nonlinear system.	38
Figure 29	Estimated PDFs.	38
Figure 30	Crest factor.....	40
Figure 31	K-factor; (a) Linear system, (b) Nonlinear system.....	40
Figure 32	10% duration of transient signal T1_lin.	41
Figure 33	10% durations from transient signals; a) Shaker transient excitation, b) Impact hammer excitation.....	41
Figure 34	Estimated exponentially decaying function of transient signal T1_lin.	42
Figure 35	Estimated coefficients Y ₀ and a of the Exponential decaying functions; (a) Shaker transient excitation, (b) Impact hammer excitation.	42
Figure 36	First three temporal moments on time-histories; a) T1_lin, b) R1_lin.....	43
Figure 37	First five temporal moments of the linear system subjected to a transient input.	45
Figure 38	First five temporal moments of the linear system subjected to a random input.....	46
Figure 39	First five temporal moments of random signal in nonlinear system.	47
Figure 40	Autocorrelation functions of random signals in the linear system.	49
Figure 41	Autocorrelation functions of random signal in nonlinear system.	49
Figure 42	Correlation coefficients of random signals; (a) Linear system, (b) Nonlinear system....	50
Figure 43	FRF and Coherence function from random data in linear system.....	53
Figure 44	FRF and Coherence function from random data in nonlinear system.....	53
Figure 45	Overlay of FRFs and coherence functions from experimental data in linear system; (a) Linearity from random signals, (b) Reciprocity from impact hammer signals.....	53
Figure 46	Linearity checks in the nonlinear system; (a) Experimental data, (b) Numerical data from model N1, (c) Numerical data from model N2.....	54
Figure 47	Reciprocity checks in the nonlinear system; (a) Experimental data, (b) Numerical data from model N1, (c) Numerical data from model N2.....	55
Figure 48	PSDs of the experimental data when harmonic excitations are applied to the linear and nonlinear systems.	56
Figure 49	PSDs from the experimental and numerical data when harmonic excitations are applied to the nonlinear system	57
Figure 50	Response spectra corresponding to a random excitation; (a) Linear system), (b) Nonlinear system.	58
Figure 51	Cepstrum of harmonic signals in the nonlinear system.....	59
Figure 52	Overlays of the logarithm of the Fourier spectra and the “lifter” spectra.	60

Figure 53	Holder exponent derived from the responses of the nonlinear system, and the time-histories indicating extracted singularity points; a) R1_nonlin, b) R1_nonlin_num1, c) R1_nonlin_num2,	62
Figure 54	Calculated AIC for AR model of the random signal.....	64
Figure 55	Estimated PAF for AR models from the random signal.	65
Figure 56	Estimated AR parameters for the linear system.	66
Figure 57	Overlays of original data and time-series from AR model of the linear system.	66
Figure 59	NPPs of estimated residual errors from AR model of the linear system.....	67
Figure 60	PSDs of estimated residual errors from AR model of the linear system.....	68
Figure 61	Estimated AR parameters for the nonlinear system.....	68
Figure 62	Overlays of original data and time-history from AR model in the nonlinear system.	69
Figure 63	Estimated residual errors of AR model in the nonlinear system.....	70
Figure 64	NPPs of estimated residual errors of AR model in the nonlinear system.	71
Figure 65	Estimated ARX parameters for the linear system; (a) AR parameters, (b) X parameters.....	72
Figure 66	Overlays of original data and time-history from ARX model in the linear system.....	73
Figure 67	NPPs of estimated residual errors of ARX model in the linear system.....	74
Figure 68	Estimated AR-ARX parameters using estimated residual error from AR (60) model estimation in the linear model.....	75
Figure 69	Overlays of original data and time-history from AR-ARX model in the linear system..	76
Figure 70	NPPs of estimated residual errors of AR-ARX model in the linear system.....	76
Figure 71	Parameter sets sampled by Latin hypercube for the linear model (200 runs).	80
Figure 72	RMSE values of time-histories for the 200 runs of the linear model.....	81
Figure 73	Overlay of the measured and simulated time-histories	81
Figure 74	Mahalanobis distances for feature vectors defined with five basic statistics	82
Figure 75	Mahalanobis distances for feature vectors defined with the first five temporal moments.	82
Figure 76	Mahalanobis distances obtained with a single type of response features.....	83
Figure 77	Mahalanobis distances for feature vectors defined with the peak amplitude and standard deviation.	84
Figure 78	RMSE values of numerical predictions obtained with the calibrated damping ratios and different input forces.	85
Figure 79	Mahalanobis distances for feature vectors defined with the peak amplitude and standard deviation of time-history responses.	85
Figure 80	Comparison of measured and predicted PCA generalized coordinates of the fourteen- feature vectors.	89
Figure 81	Posterior probability distribution of damping ratios of the linear model.	90
Figure 82	Mahalanobis distances with and without calibrated damping ratios.	91
Figure 83	Values of damping ratios used for sampling and calibration.	91
Figure 84	RMSE of time-histories for the 400 simulations of the nonlinear model.....	93
Figure 85	Comparisons of experimental (blue) and numerical (red) time-histories.....	93
Figure 86	Segments defined for feature extraction in each time-history.....	94
Figure 87	Mahalanobis distances for feature vectors defined with the standard deviations of Segment #1-#64.	95
Figure 88	Comparison of feature vectors	95
Figure 89	Two-dimensional space of model parameters (Gap; Δ) sampled by the Latin hypercube design.	96

List of Tables

Table 1	Random Excitation Data	16
Table 2	Chirp Excitation Data	16
Table 3	Single-Frequency Harmonic Excitation Data	16
Table 4	Shaker Transient Excitation Data	16
Table 5	Impact Hammer Excitation Data	17
Table 6	Linear Model Damping Parameters	22
Table 7	Nonlinear Model Parameters	22
Table 8	Numerical Data Sets for the Random Excitations	22
Table 9	Numerical Data Sets for the Chirp Excitations	22
Table 10	Numerical Data Sets for the Harmonic Excitations	23
Table 11	Numerical Data Sets for the Shaker Transient Excitations	23
Table 12	Numerical Data Sets for the Impact Hammer Excitations	23
Table 13	Resonant Frequencies (Hz) from Experimental and Numerical Modal Analysis.....	30
Table 14	Damping Ratio (%) from Experimental Modal Analysis	30
Table 15	Definition of the Basic Signal Statistics	32
Table 16	Definitions of the first five temporal moments	43
Table 17	Prior ranges of the Second- and Fourth-Mode Damping Ratios for the Linear Model ..	80
Table 18	Sampling of Model Parameters for the Estimation of R ² -Statistics.....	86
Table 19	R ² Relative Influence that Damping Ratios Exercise on Response Features.....	87
Table 20	Principle Component Analysis of the Feature Vector of 14 Features.....	88
Table 21	Statistics of two calibrated damping ratios	90
Table 22	Prior Ranges of Parameters (Gap ; Δ ; k_B) of the Nonlinear Model	93

ACRONYMS

Acronym	Definition
AIC	Akaike's information criterion
ANOVA	Analysis-of-Variance
AR	autoregressive model
ARMA	autoregressive moving average
ARX	AutoRegressive with eXogeneous input
ASC	Advanced Scientific Computing
DoE	Design-of-Experiment
DOF	degree-of-freedom
FE	finite element
FFT	(Fast) Fourier transform
FRF	frequency response function
FRF	frequency response function
GPM/SA	Gaussian Process Modeling for Simulation Analysis
LANL	Los Alamos National Laboratory
MAC	modal assurance criterion
MCMC	Markov Chain Monte Carlo
MDOF	multi-degree-of-freedom
MV	Model Validation
NPP	normal probability plot
PAF	autocorrelation function
PCA	Principal Component Analysis
PDE	partial differential equation
PDF	probability distribution function
PSD	power spectral density
RMS	root mean square
RMSE	root mean squared error
RMSE	root-mean-square of residual errors
SDOF	single degree-of-freedom
SHM	structural health monitoring
STD	standard deviation
SVD	singular value decomposition
UQ	uncertainty quantification
UQ	Uncertainty Quantification

FEATURE EXTRACTION FOR STRUCTURAL DYNAMICS MODEL VALIDATION

by

Mayuko Nishio¹, François Hemez², Chris Stull³, Charles Farrar⁴, Gyuhae Park⁵, Phil Cornwell⁶, Elói Figueiredo⁷, D.J. Luscher⁸, Keith Worden⁹

¹Dept. of Civil Engineering, Yokohama National University, Japan

²Integrated Design and Assessment Group, Los Alamos National Laboratory

³Nondestructive Testing and Evaluation Group, Los Alamos National Laboratory

⁴Engineering Institute, Los Alamos National Laboratory

⁵Chonnam National University, South Korea

⁶Rose Hulman Institute of Technology

⁷Universidade Lusófona, Portugal

⁸Fluid Dynamics and Solid Mechanics Group, Los Alamos National Laboratory

⁹University of Sheffield, UK

1. INTRODUCTION

In many fields of computational science, numerical models are developed for predicting the response of a system when the phenomenon of interest cannot be studied by direct measurement or when numerical simulations are cheaper than experimental testing. Such phenomena that cannot be easily or economically studied through experimental observation include failure resulting from catastrophic loading events or any other response occurring in the tails of the probability density functions.

Nevertheless, developing sophisticated physics-based models does not necessarily guarantee accuracy and predictability. It must somehow be verified that the assumptions involved in the successive steps of idealization, discretization, and modeling yield satisfactory predictions. This process is known as *model validation* and is usually carried out by comparing the predictions of a model, or family of models, to experimental data. The distinction is made here between model validation and *model verification*, in which the latter aims to ensure that the numerical formulations associated with a particular algorithm have been implemented correctly and yield the appropriate level of accuracy. Model verification is usually focused on comparing the model output to analytical, closed-form solutions. The distinction between validation and verification is often succinctly summarized as:

Verification determines if we are solving the equations correctly while validation assesses if we are solving the correct equations.

As one proceeds with the validation process, if the agreement between measurements and predictions is not satisfactory, input variables of the models can be optimized to improve the predictive quality of the numerical simulation, subject to the assumption that the basic modeling approach is appropriate for the intended purpose of the model. In structural dynamics, the

conventional approach to solving inverse problems continues to rely on finite element model-updating technology that has been extensively studied for many decades (Mottershead and Friswell, 1993). Most techniques documented in the literature are formulated in the frequency domain and apply to linear systems and stationary responses. It is only in the recent past (1990–2000) that serious attempts have been made at extending this technology to nonlinear systems and transient signals (Hemez and Doebling, 2000).

As structural dynamics becomes increasingly non-modal, stochastic and nonlinear, finite element model-updating technology must adopt the broader notions of model validation and uncertainty quantification. For example, particular re-sampling procedures must be implemented to propagate uncertainty through a forward calculation, and non-modal features must be defined to analyze nonlinear data sets. The latter topic is the focus of this report, but first, some more general comments regarding the concept of model validation will be discussed.

1.1.2 Model Validation Philosophy

The prediction of dynamic system response is strongly influenced by the nature of the particular partial differential equations (PDEs) that are used to model how the system will respond to a given input. When complex phenomena are studied, the evolution from the system's initial conditions typically exhibits a separation-of-scales behavior. An example lies in the modeling of wildfires where small-scale phenomena must account for the turbulent nature of fire, while large-scale phenomena exhibit coherent structures that mathematical operators such as the Laplacian may represent with satisfactory accuracy. In structural dynamics, this certainly applies to the phenomena by which energy is dissipated in a structure. For example, the Coulomb damping model provides a deterministic description of large-scale behavior, while the phenomenological behavior is highly stochastic and represented by the so-called “stick-and-slip” model at the microscopic level. Statistical models explain these behaviors by coupling mean-field theories to large deviation principles that characterize the system's most probable states.

The previous paragraph identifies an important point: the total predictability that may be expected from a particular model depends on the purpose intended for that model. Generally, the traditional approach for model validation is stated as follows:

“My model is valid because it reproduces the experimental measurements (or observations) with adequate accuracy...”

Nevertheless, reproducing experimental data does not guarantee predictability away from the region in the design space related to the experimental data. Also, this approach may be irrelevant when it comes to phenomenological models or statistically accurate models that do not provide deterministic outputs. Similar trends can be identified in other scientific communities such as physics, statistical sciences, biology, and climate science. Furthermore, it can be observed that the tools being applied to model validation problems are quite different from the tools generally used by structural dynamics analysts. In Fig. 1, a description is provided of the techniques used to validate computer simulations.

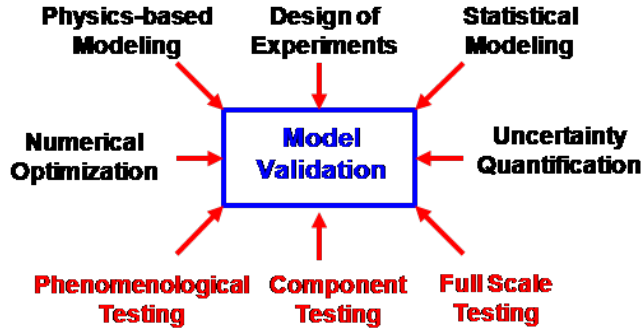


Figure 1: Conceptual view of model validation.

It is the authors' opinion that the focus of the research in model validation should be shifted from validating deterministic models to validating statistically accurate models. Such a shift in focus in which sources of uncertainty (e.g., variability in the environment, manufacturing tolerances, etc.) are now accounted for, allows one to capture the full spectrum of behavior of the systems being analyzed (from nominal response to catastrophic failure). In analyzing engineered systems that are manufactured in large numbers (i.e., automotive or airplane engines) modeling activities often attempt to capture trends in the population, as opposed to the behavior of a single unit. Therefore, the concept of model validation should be strongly coupled to uncertainty quantification (UQ), a relationship that has generally been overlooked by conventional finite element model-updating technologies.

1.2. What Does It Take To Be Predictive?

Even if very complex numerical simulations could be performed on today's most powerful computing platforms, a central question remains: What does it take to be predictive? The five elements generally mentioned as being critical to assess the predictive accuracy of a model are: 1) the geometry; 2) the physics; 3) the sources of uncertainty; 4) the model sensitivities; and 5) the output of the model.

Approximating the geometry and physics of a system remains an issue of importance in many scientific and engineering fields such as wildfire modeling, traffic modeling and global climate prediction. In structural dynamics, however, the capabilities are generally available to represent most geometry at a very fine precision level. Similarly, the physics of the systems dealt with are well-described, at least at the continuum level, by the equations of solid and fluid dynamics. Therefore, this discussion will focus on other aspects of predictive modeling (although it is acknowledged that significant research efforts are still exploring areas such as multi-scale, high-fidelity material modeling).

Propagating uncertainty through a computational model and calculating its sensitivities (or estimating the statistical correlation of an output response y_i to an input variable p_i) may offer significant computational challenges when nonlinear, stochastic models are involved. Similarly, defining the predictions of a model assumes that relevant features and metrics can adequately assess its purpose. Analysts dealing with complex numerical simulations that generate several gigabytes of output may be overwhelmed by the amount of data produced. Data compression and pattern recognition tools then become key components of the analysis and validation process.

1.3. The Evolution of Structural Dynamics

When analyzing the dynamic response of a complex system using the finite element method, it is not acceptable to neglect the contribution of an important class of components, joints, or interfaces. In the past, the influence of such neglected components on the system's dynamics response were accounted for by “tuning” or calibrating parameters in the model to agree with the experimental data. For example, the damping ratio (modal or other) was determined in an *ad hoc* manner using experimental data obtained from past experience or through experimental testing of the fully assembled system. Then the identified damping properties were added to the model to improve its predictive accuracy. At present, some of the full-scale testing capabilities that formerly existed at the U.S. national laboratories and many other facilities in the automotive, aerospace, and civil engineering communities, are no longer functional. Therefore, it is not always possible to reconcile a model with experimental measurements for *all* environments. In the future, models will be constructed with limited use of these expensive, full-scale experimental data sets.

The current trends in modeling and analysis must be added to the evolution of testing facilities and practices. Consider a pacemaker used to improve the regularity of a patient’s heartbeat. Although this system should not be referred to as a “structure” (because its primary purpose is not to carry loads), structural dynamics clearly plays a central role in its reliability analysis, and in the thermal and mechanical modeling of this device. This example illustrates that structural dynamics, with its interaction with other scientific and engineering domains and emergent technologies, will become increasingly nonlinear, non-structural, non-modal, high-bandwidth, and employ multi-physics approaches.

In these conditions, can the concept of finite element model-updating that has been developed for linear, modal dynamics be generalized? Is model-updating the correct answer to model validation? What “features” other than the conventional frequency response functions (FRFs), mode shapes, and resonant frequencies can be extracted from the data to characterize the response of a nonlinear system? How does one quantify the total uncertainty of an experiment? How does one propagate the parametric uncertainty of a numerical simulation, in either the forward direction (i.e., from input variables of the model to its predictions) or the inverse direction (i.e., from measurements back to input variables)? These are some of the questions that the model validation and uncertainty quantification disciplines are currently trying to address.

1.4. Model Updating vs. Model Validation

We argue that model validation should be thought of as a broader concept than model updating. A finite element model is not necessarily validated after its predictions have been compared to experimental data and parameters of the model have been updated. Instead, it is generally agreed upon that new, well-thought-out strategies must be established for model validation. These strategies should integrate tools such as component testing, full-scale testing, test-analysis correlation, designs-of-computer-experiments, statistical sensitivity analysis, uncertainty quantification, and finite element model updating (Fig. 1).

For validating computer models, it is generally agreed upon that errors caused by our imperfect knowledge of separable physics (i.e., effects that can be decoupled from each other) should be identified first. Examples include, but are not restricted to, material modeling, energy dissipation mechanisms, excitation forces, and the representation of boundary conditions. Numerical errors that result from the mathematical idealization and discretization of a geometry can also be

decoupled from other sources of error, to some extent. Then, the sources of variability and modeling errors that might result from the successive steps of system integration can be identified and corrected. At the separable physics or continuum levels, phenomena are generally complex, but well-controlled testing procedures can be defined. At the sub-assembly or full-scale levels, however, testing becomes more difficult; testing procedures and environments are somewhat less controlled, and variability may be a concern. However, fewer unknowns remain to be inferred from the experimental data.

In addition to recognizing that a model must be gradually validated, attention should also be paid to the operating conditions and the model's purpose. Clearly, two different experiments and (probably) two different models must be developed when the same component is subjected to random vibrations or shock response. The purpose of a model (i.e., what the model needs to predict) is also of paramount importance because it dictates the selection of response features and test-analysis metrics on which the validation should focus. As a result, model validation should be thought of in terms of a matrix of experiments rather than a single test-analysis correlation study. An example is provided in Fig. 2 that illustrates the coupling between models and applied loads. To be complete, a third axis representing the model's purpose should be added.

An example of a practical implementation of this paradigm is the validation of complex engineering simulations performed at Los Alamos National Laboratory (LANL) for the Advanced Scientific Computing (ASC) program. The application illustrated in Figs. 3 and 4 represents the highly transient response of a threaded joint assembly caused by explosive loading. The associated finite element model features 1.4 million elements, 480 contact pairs and more than 6 million degrees of freedom. Nonlinearity arises in the form of pre-load, contact mechanics, material modeling, and thermal coupling. When running on a 3 Tera-flop ASC platform (i.e., a computer that performs 3×10^9 floating point operations per second) with 504 dedicated processors, one hour of central processing unit (CPU) time is required to simulate 10^{-3} s of structural response.

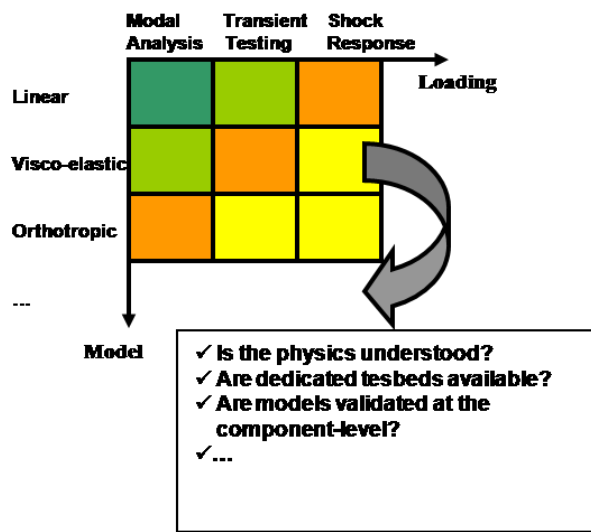


Figure 2: Matrix of model validation experiments.

Full-scale, explosive testing is also performed and multiple experimental data sets are available to estimate the repeatability of the experiment. Design-of-experiments, statistical analysis, and model validation are then implemented to identify specific joint properties as well as the degree

of variability of the assembly. A photo of the system instrumented before detonation is given in Fig. 3. Figure 4 depicts the variability obtained when testing structures assembled with different tolerances. Preliminary results are given in (Butler, Doebling, Hemez, and Sohn, 2001), and further discussion is presented in (Maupin, Hylok, Rutherford, and Anderson, 2005), (Hylok, Rutherford, Maupin, Anderson, and Groethe, 2005), and (Rutherford, Maupin, Hylok, and Anderson, 2005).



Figure 3: Testing configuration of the LANL threaded assembly.

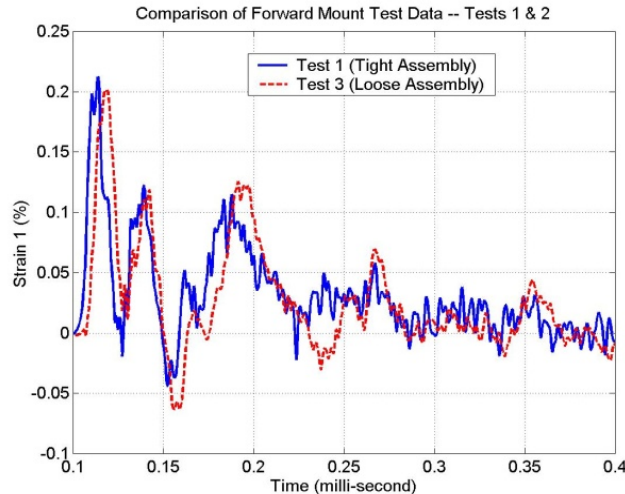


Figure 4: Strain responses (sensor 1) for two tests.

Despite recent advances in the definition and execution of model validation, the ultimate task of assessing whether the predictions of a simulation are correct remains challenging, regardless of whether it has been calibrated or not. This state of the assessment process is related to the old mathematical dilemma between interpolation and extrapolation. As such, one can argue that model validation does not exist. There is only model “invalidation” as demonstrated by Pearson’s work on hypothesis testing (Neyman and Pearson, 1933); that is, a model may be considered correct as long as it cannot be proved wrong. Practically, this implies that:

Test-analysis correlation must be capable of discriminating discrepancies caused by environmental variability and experimental and modeling uncertainty, from those caused by parametric modeling errors;

The goal of model-updating should not be to calibrate the numerical simulation such that its predictions reproduce the experimental data sets, but to arrive at predictions whose statistical distribution match the distribution of physical measurements;

Data sets not used during the updating step are required to assess the predictive quality of a model; and

Probabilities should be assigned to each model developed to reflect the degree of confidence (or lack of confidence) in its predictions.

In this work, the first three points above are illustrated. Statistical analysis of sensitivity is implemented to assess parametric variability relative to other sources of experimental or modeling errors (Point 1). The joint probability distribution of the model's input variables is inferred from experimental variability such that, when sampled, predictions of the finite element model match experimental measurements in a statistical sense (Point 2). Finally, the predictive quality of the model is assessed using data sets not used during calibration (Point 3). Point 4 is not illustrated because this study does not consider the development of multiple, competing models. It is easy to envision, however, how probabilities could be assigned to competing models based on the statistics when executing Points 2 and 3. (A follow-up study to address Point 4 has been initiated.)

1.5. Research Directions

To conclude this introductory discussion, five issues are briefly introduced that the authors believe are critical to the success of model updating, uncertainty quantification and model validation for linear and nonlinear dynamics.

Uncertainty Quantification

The success of any model validation procedure depends on the ability to quantify uncertainty. The current approach in structural dynamics is to analyze the error of the model output. This approach is not efficient for identifying the sources of discrepancy between experimental and numerical results. Instead, uncertainty should be incorporated at the beginning of the analysis, then propagated through the forward calculation. One potential approach is statistical inference based on the Bayes' theorem that estimates the posterior probability of model variables (Hanson, Cunningham, and Saquib, 1998). A posterior probability distribution is "constrained" by the experimental data such that, when sampled, the statistics of the model predictions should match those of the experimental measurements. What is important, therefore, is not necessarily that the correlated model reproduces the responses measured during a single test, but that it predicts the response levels with the same probability of occurrence as those inferred from the experimental data. Stressing the importance of uncertainty quantification for test-analysis correlation contributes to de-emphasize parametric calibration, to the benefit of performing more replicates during physical testing and more rigorously quantifying the statistics of prediction uncertainty.

Sampling and Fast Probability Integration

The notions discussed here rely strongly on the capability to propagate uncertainty and/or variability throughout an analysis. For large-scale or multi-physics simulations featuring nonlinear models, Monte Carlo sampling remains computationally too inefficient when it comes

to predicting unlikely or catastrophic events, which is one of the main reasons for carrying out an analysis. Stochastic finite element techniques (Red-Horse, Paez, Field, and Romero, 2000) and fast probability integration methods (Nessus, 1996) must therefore be developed and interfaced with engineering codes. Accelerated sampling methods such as Latin Hypercube sampling (McKay, Beckman, and Conover, 1979), Taguchi arrays, and orthogonal array sampling (Hedayat, Sloane, and Stufken, 1999) are efficient alternatives.

Generation of Fast Running Meta-Models

Efficient numerical optimization requires that the objective functions be obtained at a low computational cost. Therefore, fast-running models, also referred to as surrogates, meta-models, or emulators must be developed to replace the computationally expensive, large-scale simulations. One difficulty of fitting meta-models is efficient sampling such that sufficient information is generated in regions where the response feature's probability is maximum. This issue has been the focus of recent advances in the statistics community (McKay, 1999). It remains, however, somewhat of a "catch-22" situation because it is often desirable to develop accurate meta-models in regions of the design space where the probability of response features is a maximum, while these probabilities are estimated by performing a statistical analysis, which requires the availability of meta-models.

The second direction of open research is the implementation of probabilistic meta-models when the objective of model validation is to account for sources of variability in the experiment and numerical model. Stochastic processes can also be included to propagate other sources of discrepancy between experimental and analytical data. Examples are numerical and truncation errors, as well as bounds of total uncertainty for the physical experiments. This procedure, well-known in the geo-physics community, is progressively being tested and applied in structural dynamics (Rutherford, 1999).

Statistical Hypothesis Testing

Another issue of open research is the problem of establishing a correlation between multiple data sets. By this we mean, "assessing the degree to which two populations of data are consistent with each other." Such statistical consistency can be assessed, for example, using the Mahalanobis distance for multivariate analysis and a standard Hotelling's T^2 test. These statistics, however, only compare the mean values of two distributions. One possibility available to test both mean values and the variance/ covariance structure is to resort to an entropy metric. An example is Kullback-Leibler's relative entropy, defined as the expected value of the ratio between the probability density functions of two populations. These statistics are attractive because they are independent of the parent distribution.

The computational requirements associated with this procedure, however, rapidly become cumbersome, even when analyzing moderately-sized finite element models. This problem arises because the joint probability distribution of multiple response features considered for test-analysis correlation must be assessed for each candidate design evaluated during the optimization. This, however, is the only possibility to guarantee, at a given confidence level, that the numerical simulation is validated in the context of uncertainty quantification.

Feature Extraction

Large computer simulations tend to generate enormous amounts of output that must be synthesized into a small number of indicators for analysis. This step is referred to as data

reduction or feature extraction (Bishop, 1995). These features are typically used to define the test-analysis correlation metrics optimized to improve the predictive accuracy of the model when either calibration or inference uncertainty quantification is performed. The main issue in feature extraction is to define indicators that provide meaningful insight regarding the ability of the model to capture the dynamics being investigated. Dimensionality is also an important consideration. One would prefer to analyze low-dimensional features to make it easier to compare measurements and predictions, in addition to easing the computational burden associated with statistical convergence. Features that are used to analyze nonlinear, transient data sets include: the root-mean-square error of a time series; principal component decomposition; the shock response spectrum; auto-regressive model-based features; the power spectral density; higher-order statistical moments; and probability density functions.

1.6. Focus of this Report

This report focuses on defining and illustrating various features that can be used for structural dynamics model validation studies, and also on presenting an example where such features are extracted to improve the predictive capability of linear and nonlinear models.

This report begins with a general discussion of response features, followed by a description of the test-bed structure (including an overview of the excitation methods and data acquisition system), and the numerical models developed to simulate the response of this structure. The majority of this report then defines the respective features that have been suggested in previous studies for assessing linear and nonlinear structural dynamics. The discussion includes the process necessary to extract these features from either experimentally or numerically generated data sets, and issues that must be considered when extracting response features are also summarized. Finally, an example is presented illustrating how such features are used in the statistical comparison between numerical and experimental responses for the structural dynamics model validation.

2. FEATURES FOR MODEL VALIDATION AND UNCERTAINTY QUANTIFICATION

A response feature is a quantity extracted from the dynamic response data that is used to compare the measured system response to the response predicted by the model (Farrar and Worden, 2012). Fundamentally, the feature extraction process is based on processing the data waveforms or spectra of these waveforms (often by extracting statistics from these data), or fitting some model, either physics- or data-based, to the response data. The parameters and/or the predictive errors associated with these models then become the response features. Ideally one should select features that are correlated with the physical phenomena that the model is intended to predict. Low-dimensional features are preferable to high-dimensional features to facilitate test-analysis comparison and make it easier to estimate converged statistics. Finally, it should be emphasized that there is no single feature that will be applicable to all structural dynamics predictive modeling scenarios. If multiple aspects of the system response are of interest, the model validation process may require different features to be extracted from the data in an effort to validate different aspects of the modeling process.

One must be cognizant of the feature's dimension (i.e., the number of scalar quantities that are necessary to describe the feature). As an example, a mode shape might be used as a feature. For the eight degree-of-freedom (DOF) spring-mass system shown in Fig. 5 with an accelerometer mounted on every mass, one can develop an estimate of the mode shape based on the measured response to a dynamic excitation. This estimate would produce an 8-dimensional feature vector indicated by the circles shown in Fig. 6. However, not all of the values in this feature vector are independent of each other. Therefore, the "effective dimension" may be significantly less than the dimension of the mode shape vector. To illustrate this point, we can fit a quadratic function to the discrete mode shape amplitudes and accurately represent the mode shape with only three constants that represent the quadratic function as shown in Fig. 6. It may be concluded that the effective dimension of this feature vector is three. The fact that the effective dimension is smaller than the dimension of the original feature vector implies that there is correlation between the different elements of the 8-dimension feature vector.

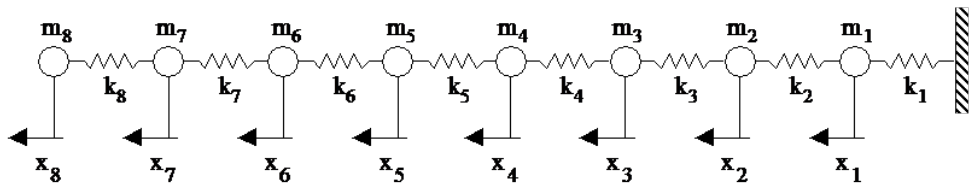


Figure 5: Eight degree-of-freedom spring-mass system.

The approaches to quantify the effective dimension of a feature vector range from well-established procedures such as principal component analysis (Bishop, 1995), to more sophisticated procedures such as factor analysis (Fukunaga, 1990), and Sammon mapping (Ripley, 1996). In many cases the process of quantifying the actual dimension of a feature vector is still a research topic for experts working in the fields of information technology and machine learning. Because of statistical modeling issues, it is generally desirable to have feature vectors with as low a dimension as possible.

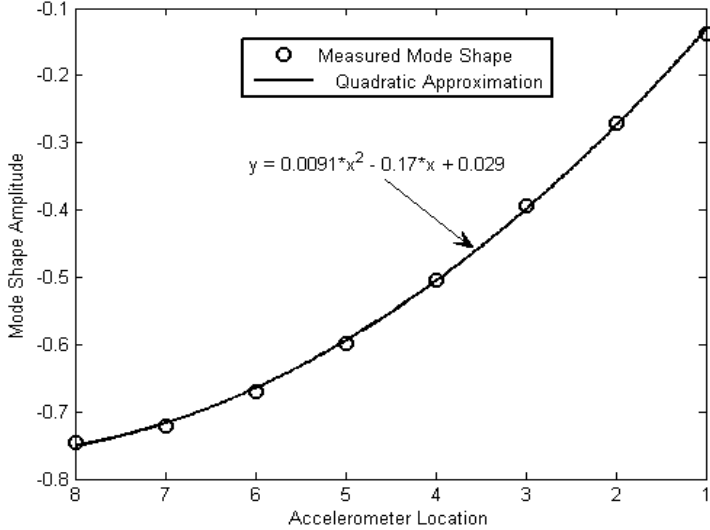


Figure 6: Measured mode shape and a quadratic approximation obtained by a least squares fit to the measured data.

In an effort to obtain a low-dimensional feature vector, procedures are developed to fuse data from multiple sensors and compress these data. A common example of data fusion is the extraction of mode shapes from the relative amplitude and phase information contained in vibration data from a sensor array. Similarly, the extraction of resonant frequencies from acceleration time histories can be thought of as data compression. As an example, consider a 1024-point time series collected from a sensor or simulated at a node in a finite element model. Using a fast Fourier transform algorithm, the power spectral density function can be calculated and estimates of the system's resonant frequencies can be identified from peaks in the power spectral density (PSD). If ten resonant frequency peaks are identified and these parameters are used as response features, then the feature extraction process has condensed the 1024-point time series into a ten-dimension feature vector.

Various forms of data normalization are also employed during the feature extraction process in an effort to separate changes in the response caused by the simulation of varying operational and environmental conditions from those caused by the modeling uncertainty. Such normalization steps would be similar to those commonly implemented, for example, in the field of structural health monitoring (SHM) where it is necessary to isolate changes in the response features caused by environmental variability from those caused by structural damage. The process of forming a frequency response function (FRF) whereby the measured or simulated responses are effectively normalized by the input force can be viewed as a data normalization process. However, the assumption that these FRFs are representative of the system's dynamic characteristics relies implicitly on the structure exhibiting the properties of stationarity, linearity and reciprocity. These assumptions may not apply to the response of a nonlinear system, in which case other forms of data normalization may have to be devised.

Another important consideration is that one must not confuse a *feature* with a *metric*. A metric is some quantity that defines the similarity or difference between two features or two populations of features. In this report, metrics are used exclusively for the purpose of test-analysis correlation. In general, metrics are some type of norm, such as the Euclidean distance between two vectors (also referred to as the L₂ norm), a statistical test, or some form of a correlation measure between two

data sets. A feature can be extracted from a single data set while a metric quantifies the difference or distance between features extracted from two different data sets.

Finally, the concept of feature extraction must be distinguished from feature selection. Feature extraction is the mathematical process of calculating a specific feature based on some set of data. Feature selection, on the other hand, is the process of determining which feature is best for a specific problem. While the former is almost always done through some mathematically rigorous process, the latter can employ a wide range of techniques from mathematically rigorous to heuristic or intuitive.

3. EXPERIMENTAL DATA ACQUISITION

A structure that can be tested in a well-controlled laboratory setting is used to illustrate the feature extraction process and subsequent model validation and calibration processes. In this model validation study, both linear and nonlinear system modeling are treated; therefore, the test-bed structure can also introduce and control the nonlinear behavior. The description of the structure and the data acquisition are explained in this chapter.

3.1. Test-Bed Structure Description

The three-story structure shown in Fig. 7(a) is the test-bed structure used in this study. The structure consists of aluminum columns and plates assembled using bolted joints (Figueiredo, Park, Figueiras, Farrar, and Worden, 2009). The size of each floor plate is $0.305 \times 0.305 \times 0.025$ m, and each is connected to floors above and/or below by four aluminum columns ($0.177 \times 0.025 \times 0.006$ m). The structure slides on rails that allow movement in the x -direction only; therefore it can accurately be represented as a four DOF system. Figure 8 shows, schematically, the basic dimensions of the test-bed structure.

Additionally, a center column ($0.150 \times 0.025 \times 0.025$ m) is suspended from the 3rd floor, and a bumper mechanism is attached to the 2nd floor as shown in Fig. 7(b) and Fig. 9. Depending on the amplitude of oscillation and the gap between the column and the bumper, a level of nonlinearity is introduced into the system as a result of the impacting between the column and the bumper mechanism. This nonlinearity is intended to produce a small perturbation to an essentially stationary process, causing a nonlinear phenomenon called intermittency (Holger and Schreiber, 1997), where the system alternates between two conditions in an irregular way. The position of the bumper can be adjusted to vary the extent of impacting that occurs during a particular excitation. This design was motivated by several real-world examples where bending and shear cracks open and close under dynamic loads. Note that the stiffness between the 2nd and 3rd floors becomes higher when the bumper contacts the column; additionally, the impact causes energy dissipation.

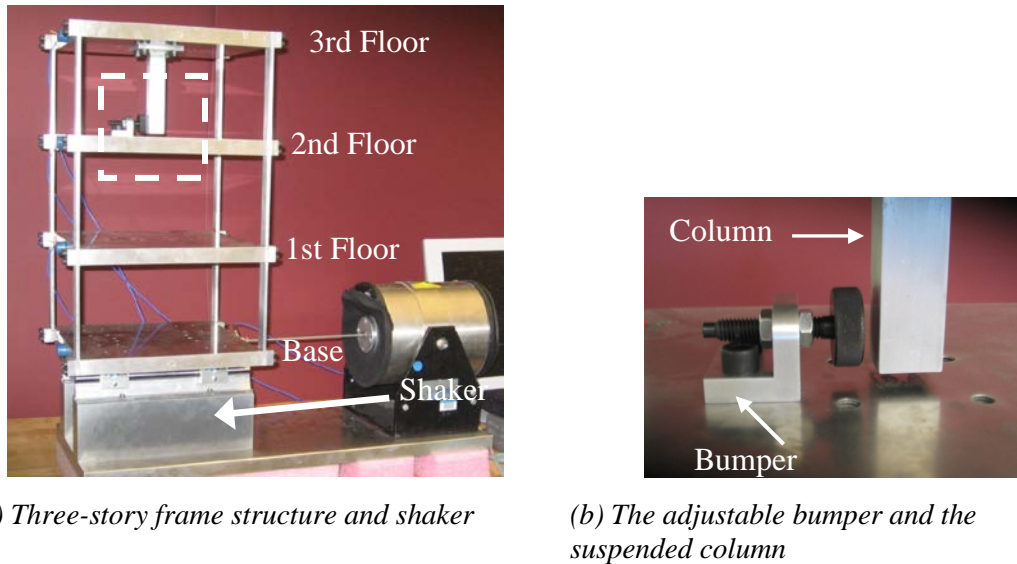


Figure 7: Set-up of the three-story structure.

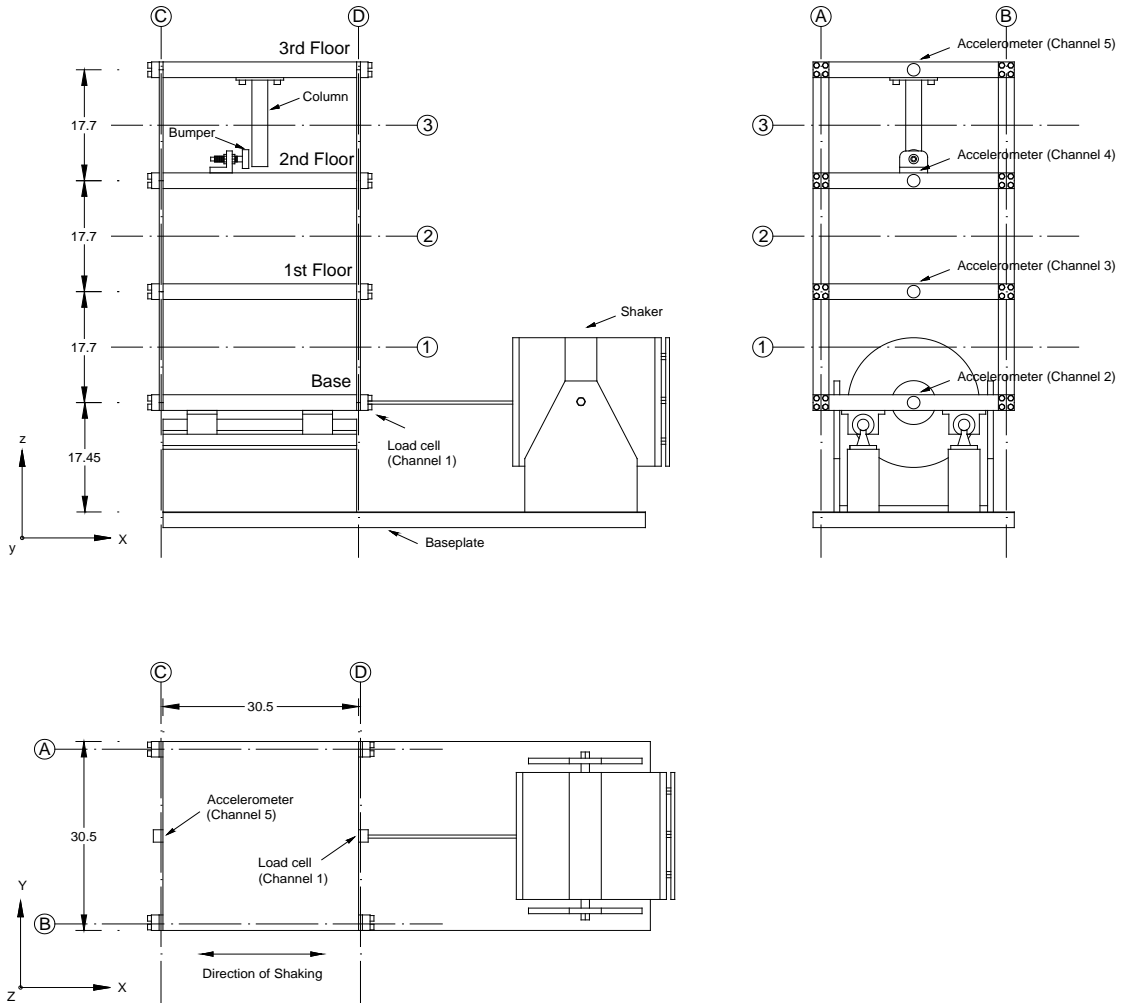


Figure 8: Basic dimensions of the three-story structure (unit: cm).

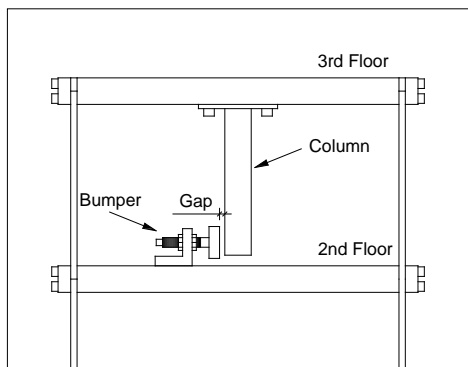


Figure 9: Structural details used to add nonlinearity.

3.2. Data Acquisition

Various input and response time-history data from different excitations were collected in an effort to illustrate the various types of features that may be used in structural dynamics validation. An electrodynamic shaker provided a lateral excitation to the base floor along the centerline of the structure. The structure and shaker were mounted together on a common base plate and the entire system rested on rigid foam. The foam was intended to minimize extraneous sources of unmeasured excitation from being introduced through the base of the system. The input signals were Random, Chirp, Harmonic, and Transient using both a shaker and an impact hammer. The force transducer (Channel #1 in Fig. 8) with a nominal sensitivity of 2.2 mV/N was attached at the end of a stinger to measure the input force from the shaker to the structure. When using the impact hammer, the stinger and the force transducer used to connect the shaker are removed from the structure, and an impacting force is applied to the 1st floor of the structure. The impact hammer used here was a PCB model 086D20. The force was measured with a sensitivity 0.23 mV/N. To measure the structure's response, four accelerometers (from Channel #2 to Channel #5 in Fig. 8) with nominal sensitivities of 1000 mV/g were attached at the centerline of each floor on the opposite side from the excitation location. A Dactron Spectrabook dynamic data acquisition system was used to collect data. The output channel of this system, which provides the drive signal to the shaker, was connected to a Techron 5530 power amplifier that in turn drives the shaker.

For the random excitation, the analog sensor signals were discretized with 4096 time domain data points sampled at 640 Hz. These sampling parameters yield data windows that were 6.4 s in duration. A band-limited random excitation in the range of 20–200 Hz was used as an input signal to avoid the rigid-body modes of the structure that are present below 20 Hz. Two different excitation levels, 2.5 V RMS and 1.5 V RMS, were used to perform a linearity check.

Chirp excitations were also applied with the same experimental setup as in the random excitation. The frequency range of these input signals was 20–250 Hz, and the excitation levels were also 2.5V RMS and 1.5V RMS. The input and response measurements were discretized with 4096 points acquired at a sampling frequency of 640 Hz.

Two single-frequency harmonic excitations were applied at 54 Hz and 71 Hz, respectively. These frequencies were approximately equal to the 3rd and 4th mode resonant frequencies of the test-bed structure. These tests were also conducted at two excitation levels corresponding to 2.5V RMS and 1.5V RMS. The acquired data consist of 16,384 points collected at a sampling frequency of 2560 Hz.

For one of the transient excitations, the impulse signals were applied to the test-bed structure with the shaker. The excitation period of transient signal was 0.05 s in order to excite all major resonant frequencies of the structure that occur in the range of 0 to 150 Hz. The excitation levels were 5.0V RMS and 2.5V RMS in this case. Moreover, 10.0 V RMS and 5.0V RMS excitations were applied to the nonlinear system to generate impacts between the suspended column and the bumper. The length of data records was 1024 points with the sampling frequency of 640 Hz.

An impact hammer was also used for transient excitations. The impacts were applied to the 1st floor, and the 3rd floor was excited in the opposite direction for checking reciprocity. For the reciprocity tests, the Channel #5 accelerometer was placed on the previous excited point at the 1st floor. The tip of the impact hammer was chosen to produce a flat input spectrum in the range 0 to

150 Hz. The data acquisition sampling frequency was 320 Hz; the length of each data recorded was 1024 points.

For all of these excitation types, data were acquired both from the linear and the nonlinear systems. For the linear system, the gap between the suspended column and the bumper in Fig. 9 was set wide enough (approximately 10 mm) so impact events would not occur. In order to introduce the nonlinearity, the gap was adjusted to 0.1 mm using a feeler gage. The acquired data are summarized in Table 1 to Table 5. Note that ten time-histories were acquired in all cases, and each time-history data set consists of data from the five sensors (Channel #1 to Channel #5 in Fig. 8).

Table 1: Random Excitation Data

Data name	Excitation level	Bumper
R1_lin	2.5V RMS	w/o
R2_lin	1.5V RMS	w/o
R1_nonlin	2.5V RMS	with
R2_nonlin	1.5V RMS	with
4096 time domain data points acquired at a sampling frequency of 640 Hz.		

Table 2: Chirp Excitation Data

Data name	Excitation level	Bumper
C1_lin	2.5V RMS	w/o
C2_lin	1.5V RMS	w/o
C1_nonlin	2.5V RMS	with
C2_nonlin	1.5V RMS	with
4096 time domain data points acquired at a sampling frequency of 640 Hz.		

Table 3: Single-Frequency Harmonic Excitation Data

Data name	Excitation level	Bumper
H1_lin	2.5V RMS	w/o
H2_lin	1.5V RMS	w/o
H1_nonlin	2.5V RMS	with
H2_nonlin	1.5V RMS	with
H3_nonlin	2.5V RMS	with
16384 time domain data points acquired at a sampling frequency of 2560 Hz. Input frequency of H1 and H2 is 71 Hz; and H3 is 54 Hz.		

Table 4: Shaker Transient Excitation Data

Data name	Excitation level	Bumper
T1_lin	5V RMS	w/o

T2_lin	2.5V RMS	w/o
T1_nonlin	5.0V RMS	with
T2_nonlin	10.0V RMS	with
1024 time domain data points acquired at a sampling frequency of 640 Hz		

Table 5: Impact Hammer Excitation Data

Data name	Excited floor	Bumper
I1_lin	1st	w/o
I2_lin	3rd	w/o
I1_nonlin	1st	with
I2_nonlin	3rd	with
1024 time domain data points acquired at a sampling frequency of 320 Hz		

4. NUMERICAL MODEL AND CALCULATION

The numerical modeling and response calculations for the test-bed structure are presented in this chapter. A lumped-mass model is adopted in this study. In most detailed numerical analyses of structures, a finite element (FE) model is often employed to predict the system's behavior particularly when one needs to model the detailed responses at joints or interfaces and complicated nonlinear response phenomena. In using detailed FE models, there can be a significant number of uncertain parameters that must be assigned, including loading conditions, material and geometric properties, system connectivity, and boundary conditions. Also, the specification of initial conditions and temporal and spatial discretization in the solution procedure requires the definition of additional parameters that may contribute further to sources of variability with the predictions. On the other hand, simple lumped-mass models can provide adequate predictions of the pertinent system response characteristics in lieu of detailed FE models. These models make it possible to simplify the number of model and solution parameters that need to be specified, which allows one to more directly study the model validation problem. The results of this study can be extended to more detailed FE modeling noting that the issue of variability in spatial discretization (often referred to as "mesh convergence") has not been addressed.

4.1. Four Degree-of-Freedom Lumped-Mass Model

Figure 10 shows a four-DOF lumped-mass model of the test-bed structure. The mass of i^{th} story is designated m_i ($i = 1, \dots, 4$), and they are coupled by the columns with stiffness k_i ($i = 1, \dots, 4$) and the dampers with damping coefficients c_i ($i = 1, \dots, 4$). Notice that the model includes the base mass m_1 that slides on the rails. The spring and damper with stiffness and damping values k_1 and c_1 are intended to simulate the friction between the rails and the bottom floor of the structure. The numerical values of m_i were determined from actual measured masses of the various structural elements. The stiffness k_i (except k_1) can be assigned as the summation of the bending stiffness of the four columns with rotation at either end of the column restrained; calculated on the basis of Euler-Bernoulli beam-theory ($12EI/L^3$), where I is the cross-sectional area moment of inertia, L is the between-floor distance, and E is the nominal Young's Modulus of aluminum (65 GPa).

For a shear-building model, the equations of motion can be described in a matrix notation as follows:

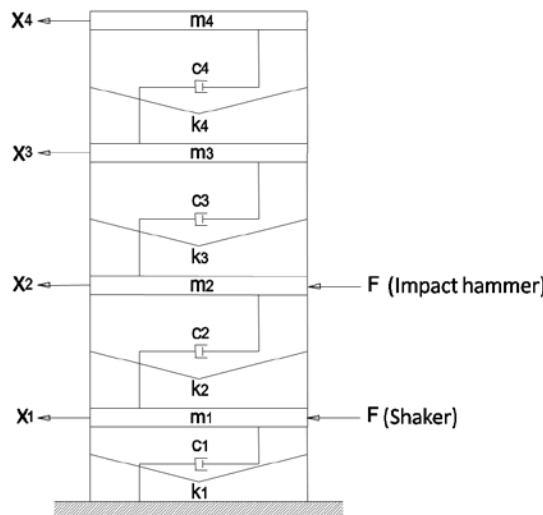


Figure 10: Four DOF shear-building model of the test-bed structure.

$$[M]\{\ddot{x}\} + [C]\{\dot{x}\} + [K]\{x\} = \{F(t)\}, \quad (1)$$

where the [M], [C], and [K] are the mass, damping, and stiffness matrixes of the system, respectively. The vector {F(t)} is the input force vector, and {x} is the vector of unknown displacements at the nodal coordinates. The mass and stiffness matrices are given by

$$[M] = \begin{bmatrix} m_1 & 0 & 0 & 0 \\ 0 & m_2 & 0 & 0 \\ 0 & 0 & m_3 & 0 \\ 0 & 0 & 0 & m_4 \end{bmatrix} \quad [K] = \begin{bmatrix} k_1 + k_2 & -k_2 & 0 & 0 \\ -k_2 & k_2 + k_3 & -k_3 & 0 \\ 0 & -k_3 & k_3 + k_4 & -k_4 \\ 0 & 0 & -k_4 & k_4 \end{bmatrix} \quad (2)$$

where $m_1 = 6.54$ kg ("mass of the base plate" + 4 × "mass of half of the column" + 4 × "mass of the column screw block"), $m_2 = 6.66$ kg ("mass of the 1st floor plate" + 4 × "mass of the column" + 4 × "mass of the column screw blocks"), $m_3 = 6.86$ kg ("mass of the 2nd floor plate" + 4 × "mass of the column" + 4 × "mass of the column screw blocks" + "mass of the bumper"), $m_4 = 6.8$ kg ("mass of the 3rd floor plate" + 4 × "mass of half of the column" + 4 × "mass of the column screw blocks" + "mass of the suspended column"). The stiffness k_2 , k_3 , and k_4 are calculated as 399,790 N/m, which are the summation of the bending stiffness of the four columns. For the stiffness k_1 , a relatively low value $k_1 = 10$ N/m is assigned compared with other stiffness because the friction between the rails and the structure can be negligible in this structure.

The equations of motion can then be uncoupled with the modal damping assumption (Naeim and Kelly, 1999), in which [C] can be evaluated from the following modal damping matrix

$$[C^M] = \begin{bmatrix} 2\zeta_1\omega_1 M_1 & 0 & 0 & 0 \\ 0 & 2\zeta_2\omega_2 M_2 & 0 & 0 \\ 0 & 0 & 2\zeta_3\omega_3 M_3 & 0 \\ 0 & 0 & 0 & 2\zeta_4\omega_4 M_4 \end{bmatrix}, \quad (3)$$

where ζ_k , ω_k , and M_k are the damping ratio, resonant frequency and modal mass associated with the k th mode ($k = 1, \dots, 4$). The modal damping ratios are empirical values that are often estimated from experimental data assuming the structure responds as a linear system, or assigned based on past experimental observations made on similar structures. The damping matrix [C] and the modal damping matrix $[C^M]$ are related by

$$[C^M] = [\phi]^T [C] [\phi], \quad (4)$$

where $[\phi]$ is the mode shape matrix. As a consequence, the damping matrix [C] can be determined by

$$[C] = [[\phi]^T]^{-1} [C^M] [\phi]^{-1}. \quad (5)$$

The impact nonlinearity between the 2nd and 3rd floors is described by way of a bilinear model. During the period when the bumper on the 2nd floor contacts the suspended column on the 3rd floor, the bending stiffness of the column is added to the stiffness k_4 . For this model, the relationship between the relative displacement $X = x_4 - x_3$ and the internal force to the 2nd or 3rd floors was represented by the nonlinear load-displacement relationship indicated in Fig. 11. The initial slope of this curve, k_c , is equal to the stiffness k_4 ; i.e., the summation of the bending stiffness of the four columns located between the 2nd or 3rd floors. When the bumper contacts the suspended column, the stiffness k_4 changes from k_c to $k_c + k_b$, where k_b is the bending stiffness of the suspended column. The aluminum suspended column is the box cantilever beam with the square outer cross-section; 0.025 m on a side, with the wall thickness of 0.003 m. The length of column L is 0.130 m; therefore, the bending stiffness of cantilever beam is calculated as $k_b^E = 1.925E+6$ N/m on the basis of the Euler-Bernoulli beam-theory ($3EI/L^3$). On the other hand, the suspended column can also be considered as a deep beam because its thickness-length ratio is around 0.2. In this case, the bending stiffness becomes $k_b^T = 1.770E+6$ N/m by assuming Timoshenko beam theory, which is calculated by:

$$k_b^T = \left(\frac{L^3}{3EI} + \frac{L}{G\kappa A} \right)^{-1}, \quad (6)$$

where G is the modulus of rigidity, A is the area of cross-section, and κ is the shear correction factor. Actually, the decision regarding which of these models to use is also an issue for *Model Validation*; and it should be based on an investigation of the sensitivity of response predictions from these different models to the measured system response in the context of the models intended purpose. Here, the difference between the values of k_b^E and k_b^T is approximately 8%. Also, it was observed in a qualitative manner that the structure's calculated time-history responses were insensitive to these different stiffness models. Therefore, for simplicity, the bending stiffness from the *Euler-Bernoulli* beam-theory k_b^E was adopted for k_b in this report. Additionally, the use of a k_b^E eliminates the shear correction factor κ as an additional uncertain parameter.

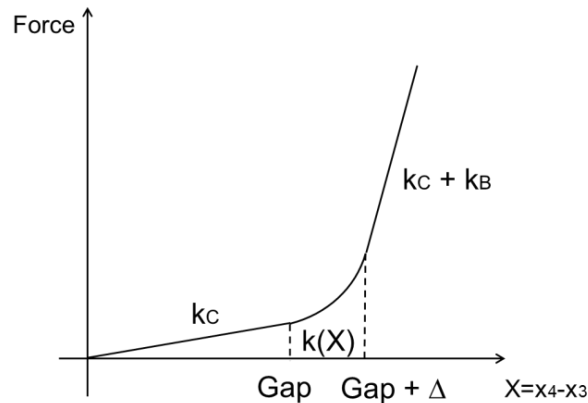


Figure 11: Force-displacement relation for relative displacement between second and third floors.

Furthermore, it was not expected that the stiffness would change abruptly from k_c to $k_c + k_b$ when X exceeded the initial gap in the bumper mechanism, and thus, a smooth transition region was

defined over a distance Δ to model the change between two stiffness-states as shown in Fig. 11. Using the relative displacement $X = x_4 - x_3$, the stiffness k_4 can then be described as

$$k_4 = \begin{cases} k_C & X \leq Gap \\ k(X) & Gap < X < Gap + \Delta \\ k_C + k_B & X \geq Gap + \Delta \end{cases} . \quad (6)$$

The stiffness within the range $Gap < X < Gap + \Delta$ is a function of X , and was modeled by a linear function to satisfy C_1 -continuity at $X = Gap$ and $X = Gap + \Delta$, as given by

$$\begin{aligned} k(X) &= AX + B \\ A &= \frac{k_B}{\Delta}, \quad B = k_C - k_B \frac{Gap}{\Delta} \end{aligned} . \quad (7)$$

4.2. Numerical Calculations

For comparative purposes in the feature extraction study, various numerical run sets are obtained with varying uncertain parameters of the lumped-mass model. One of uncertain model parameters in the linear model is damping matrix $[C]$, corresponding to the damping ratios ζ_k . As mentioned in the previous section, the modal damping ratios can be estimated from experimental data; however, it is difficult to derive accurate values based exclusively on the structure's geometric and material properties. Thus, this value is often specified based on previous observations with similar structures and anticipated load levels; e.g., an accepted range for metal structures damping is between 0.01 to 0.05, and that for concrete structures is between 0.05 to 0.10 (Weaver and Johnston, 1987). Additionally, there are parameters that influence the impact behavior in the nonlinear model: specifically the values for Gap and Δ in Fig. 11, and these values are difficult to define *a priori*. In particular, value Δ is very uncertain because it depends on how one adjusts the bumper system. If a smaller numerical value of Δ is specified, the influence of impact events on the time-histories becomes larger. Damping ratios ζ_k and Δ are thus treated as the uncertain parameters in the subsequent feature extraction study.

To calculate linear system responses, two numerical models were prepared that had different damping ratio patterns as given in Table 6. The damping ratios of Model #L1 were 0.01 in the first to fourth mode, whereas for Model #L2, the second mode damping ratio of 0.05 was prescribed. The values for Model #L1 were generally acceptable values for a metal structure, and those for Model #L2 were based on the results of the experimental modal analysis, which was carried out in a previous study using the same structure (Figueiredo et al., 2009). In this study, the second mode damping ratio showed a high value compared with the other modal damping values. For the nonlinear system calculations, two values of Δ , 0.5mm and 0.1mm, were applied using the identified damping ratios in the experimental modal analysis (the values in Model #L2). The parameters for nonlinear Model #N1 and #N2 are given in Table 7.

The numerical simulations are summarized in Tables 8-12. Notice that the measured input force data acquired by the transducer was used as the input force vector $\{F(t)\}$ in each calculation. The number of data points and the sampling frequency are the same as those of each experimental data set, and each data set has ten time-histories from all sensor channels. The Runge-Kutta numerical integration method (ODE45 in Matlab) was used for these response calculations. Additionally, the responses calculated by the differential equation solver were then interpolated

using the “DEVAL” command in Matlab so the numerical responses were obtained at a sampling frequency equivalent to that corresponding to the experimental results.

Table 6: Linear Model Damping Parameters

Mode #	Model #L1	Model #L2
First Modal Damping Ratio	0.01	0.01
Second Modal Damping Ratio	0.01	0.05
Third Modal Damping Ratio	0.01	0.01
Fourth Modal Damping Ratio	0.01	0.01

Table 7: Nonlinear Model Parameters

	Model #N1	Model #N2
Delta Δ (mm)	0.5	0.1
First Modal Damping Ratio	0.01	
Second Modal Damping Ratio	0.05	
Third Modal Damping Ratio	0.01	
Fourth Modal Damping Ratio	0.01	

Table 8: Numerical Data Sets for the Random Excitations

Response Data Name	Input force	Model #
R1_lin_num1	R1_lin	L1
R1_lin_num2		L2
R2_lin_num1	R2_lin	L1
R2_lin_num2		L2
R1_nonlin_num1	R1_nonlin	N1
R1_nonlin_num2		N2
R2_nonlin_num1	R2_nonlin	N1
R2_nonlin_num2		N2

4096 time domain data points acquired at a sampling frequency of 640 Hz.

Table 9: Numerical Data Sets for the Chirp Excitations

Response Data Name	Input force	Model #
C1_lin_num1	C1_lin	L1
C1_lin_num2		L2
C2_lin_num1	C2_lin	L1
C2_lin_num2		L2
C1_nonlin_num1	C1_nonlin	N1
C1_nonlin_num2		N2

C2_nonlin_num1	C2_nonlin	N1
C2_nonlin_num2		N2
4096 time domain data points acquired at a sampling frequency of 640 Hz.		

Table 10: Numerical Data Sets for the Harmonic Excitations

Response Data Name	Input force	Model #
H1_lin_num1	H1_lin	L1
H1_lin_num2		L2
H2_lin_num1	H2_lin	L1
H2_lin_num2		L2
H1_nonlin_num1	H1_nonlin	N1
H1_nonlin_num2		N2
H2_nonlin_num1	H2_nonlin	N1
H2_nonlin_num2		N2
H3_nonlin_num1	H3_nonlin	N1
H3_nonlin_num2		N2
16384 time domain data points acquired at a sampling frequency of 2560 Hz.		

Table 11: Numerical Data Sets for the Shaker Transient Excitations

Response Data Name	Input Force	Model #
T1_lin_num1	T1_lin	L1
T1_lin_num2		L2
T2_lin_num1	T2_lin	L1
T2_lin_num2		L2
T1_nonlin_num1	T1_nonlin	N1
T1_nonlin_num2		N2
T2_nonlin_num1	T2_nonlin	N1
T2_nonlin_num2		N2
1024 time domain data points acquired at a sampling frequency of 640 Hz.		

Table 12: Numerical Data Sets for the Impact Hammer Excitations

Data Name	Input Force	Model #
I1_lin_num1	I1_lin	L1
I1_lin_num2		L2
I2_lin_num1	I2_lin	L1
I2_lin_num2		L2
I1_nonlin_num1	I1_nonlin	N1

I1_nonlin_num2		N2
I2_nonlin_num1	I2_nonlin	N1
I2_nonlin_num2		N2
1024 time domain data points, and the sampling frequency of 320 Hz.		

4.3. Overlay of Time-Histories

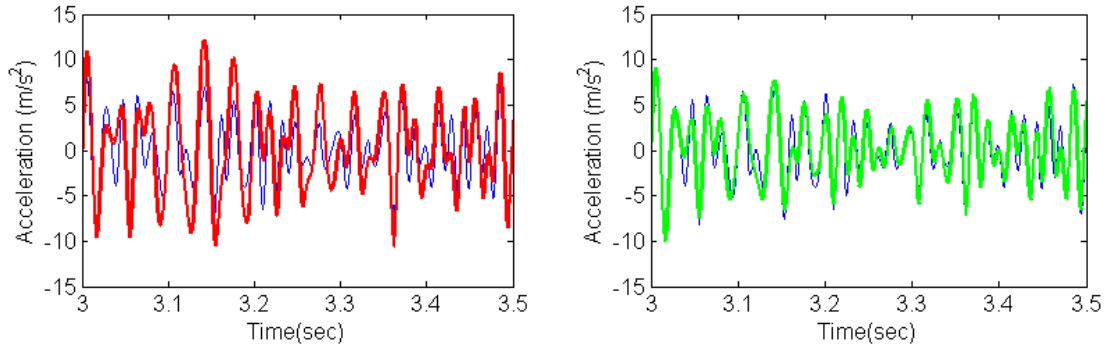
Simple comparisons of the numerical runs with the experimental data are performed by overlaying the response time-histories. However, it should be noted that the time-histories are high-dimensional features resulting in comparisons that are somewhat subjective and qualitative. These comparisons still provide some assessment of the numerical models' validity.

4.3.1. Linear System

Figures 12–16 show overlays of numerical and experimental responses from the linear system corresponding to the different excitation types. All time-histories represent accelerations from Channel #5 (third floor) and are the first of ten generated histories (History#1). Notice that the red lines indicate the numerical runs from Model #L1, and the green lines are the runs from Model #L2, and blue lines are experimental data in all figures.

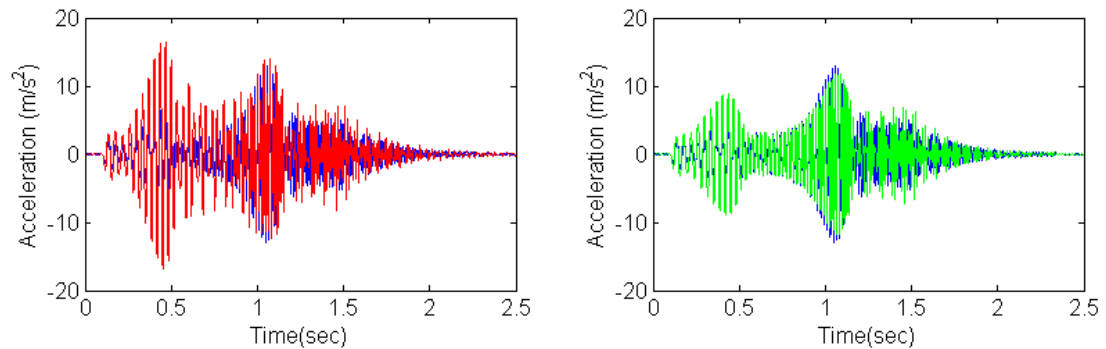
When examining the results from the random excitations, the time-history from Model #L2 (Fig. 12(b)) shows better agreement with the experimental data as compared to the result from Model #L1 (Fig. 12(a)), which exhibits larger amplitudes than those in the experimental data. This result is related to the difference in the second mode damping ratio, which in Model #L2 is larger than that in #L1. This point is also observed in the case of chirp excitation; at the time of around 0.5 sec in Fig. 13(a) and (b) where it can be seen that the amplitude of response from Model #L2 (green) is much closer to the experimental data than that from #L1 (red). Notice that as the chirp input signal approached the second mode resonant frequency (around 30 Hz) at approximately 0.5 sec the influence of the second mode damping ratio can be clearly seen. In the results corresponding to the harmonic excitation (Fig. 14), there is no apparent difference between two numerical runs because the frequency of input signal (71 Hz) corresponds not to the second mode, but to the fourth mode resonant frequency of the system. The influence of the different damping values can also be seen in the results corresponding to the transient and hammer excitations. In the numerical time-histories from the case of the transient excitation, as presented in Fig. 15, there is a difference in the decay speed of response resulting from the different damping ratios. On the other hand, there is little difference between time-histories from Model #L1 and #L2 in the case of impact hammer excitation as shown in Fig. 16. The explanation for this result was that hammer impact was applied to the first floor; therefore, the second mode was not significantly excited as compared to the case of transient excitation.

The results of time-history overlays qualitatively indicate that the damping ratios assigned in Model #L2 more appropriately represent the damping characteristic of the linear test-bed structure than those used with Model #L1.



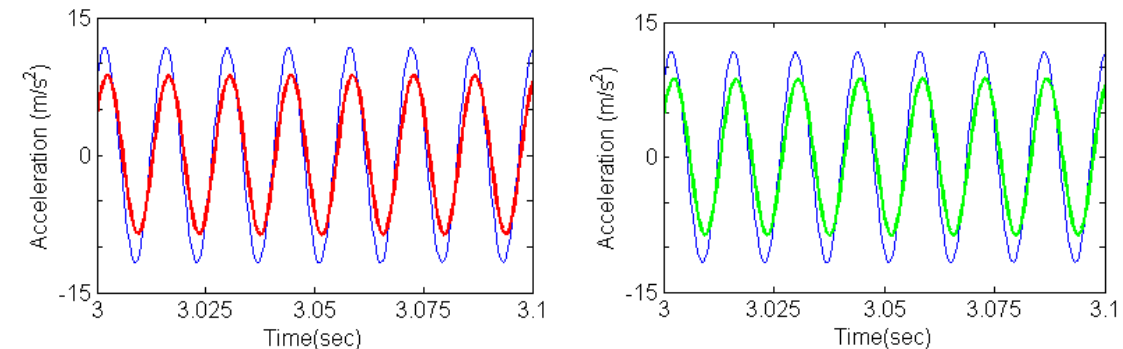
(a) "R1_lin_num1" (Red) and "R1_lin" (Blue) (b) "R1_lin_num2" (Green) and "R1_lin"

Figure 12: Time-histories for random excitations applied to the linear system.



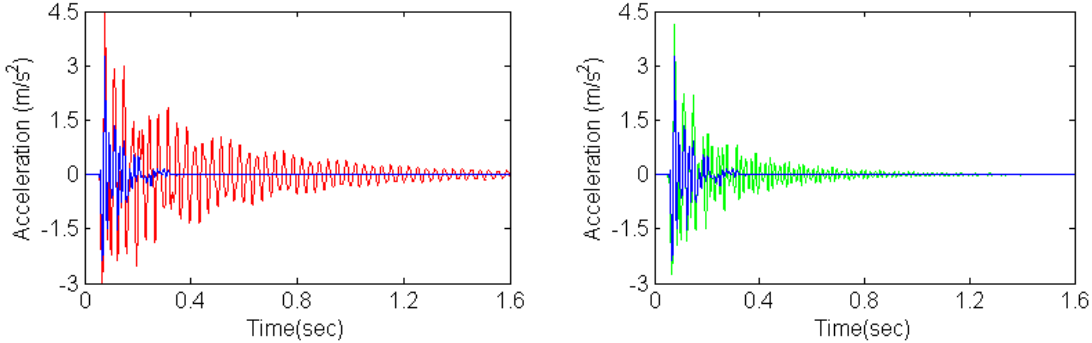
(a) "C1_lin_num1" (Red) and "C1_lin" (Blue) (b) "C1_lin_num2" (Green) and "C1_lin"

Figure 13: Time-histories for chirp excitations applied to the linear system.



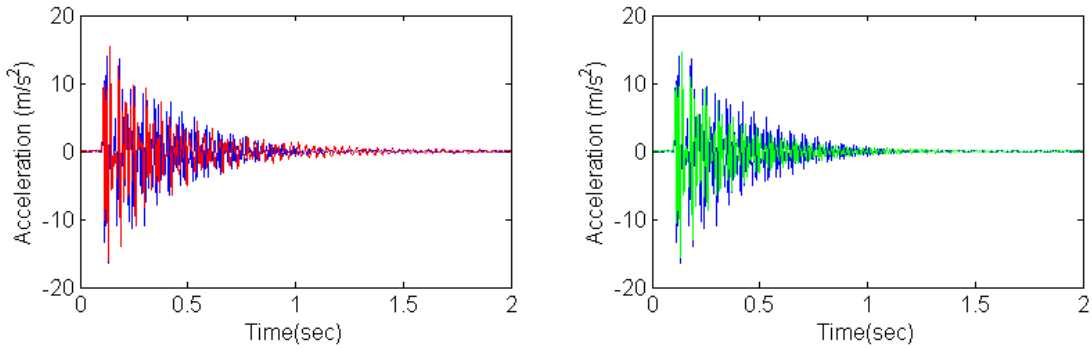
(a) "H1_lin_num1" (Red) and "H1_lin" (Blue) (b) "H1_lin_num2" (Green) and "H1_lin"

Figure 14: Time-histories for harmonic excitations applied to the linear system.



(a) “*T1_lin_num1*” (Red) and “*T1_lin*” (Blue) (b) “*T1_lin_num2*” (Green) and “*T1_lin*”

Figure 15: Time-histories for shaker transient excitations applied to the linear system.



(a) “*I1_lin_num1*” (Red) and “*I1_lin*” (Blue) (b) “*I1_lin_num2*” (Green) and “*I1_lin*”

Figure 16: Time-histories for impact hammer excitations applied to the linear system.

4.3.2. Nonlinear System

Figures 17–21 show the overlays of time-histories from the nonlinear system with the bumper mechanism. All of them are the time-histories from Channel #5 (third floor) in History #1. The red lines indicate numerical data from Model #N1 and the green lines are the numerical data from Model #N2. The red and green dots shown in the figures indicate the impact events when the bumper contacts the column; i.e., the relative displacement X becomes larger than Gap in Fig. 11. The time-histories given by blue lines represent the experimental data.

From the results corresponding to the random, chirp, and harmonic excitations (Fig. 17 to Fig. 19), it can be seen that the numerical outputs from Model#N1 shows better agreement with the experimental data than those from Model #N2. The amplitudes of responses from Model #N2 are much larger than those observed in the experimental data especially during the impact events. It can be said that the value Δ mainly influences the amplitude of the response during the impact event, and the value $\Delta = 0.5$ mm is considered to be a more appropriate value to describe the nonlinearity of the test-bed structure. On the other hand, the numerical runs corresponding to the two types of transient excitations (Fig. 20 and Fig. 21) indicate that few impact events occur, making it difficult to investigate the validity of the nonlinear models using these data.

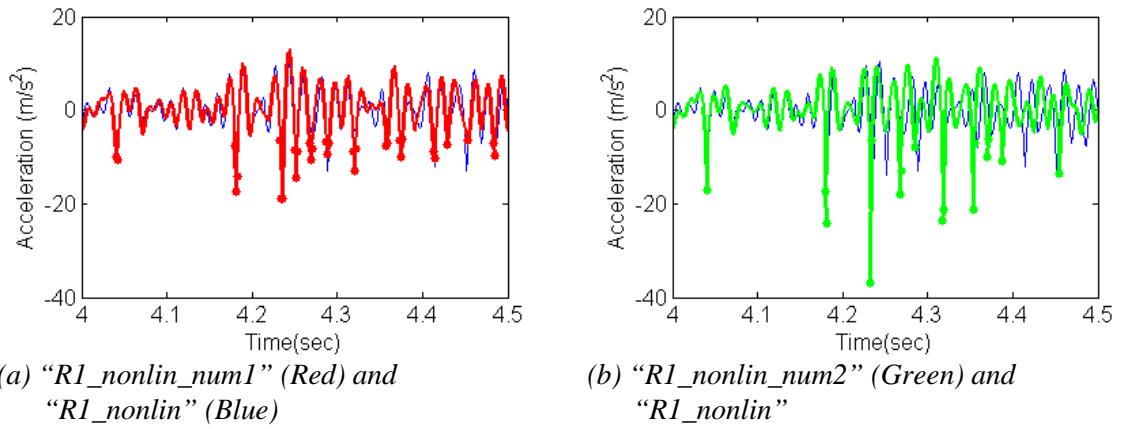


Figure 17: Time-histories for random excitations applied to the nonlinear system.

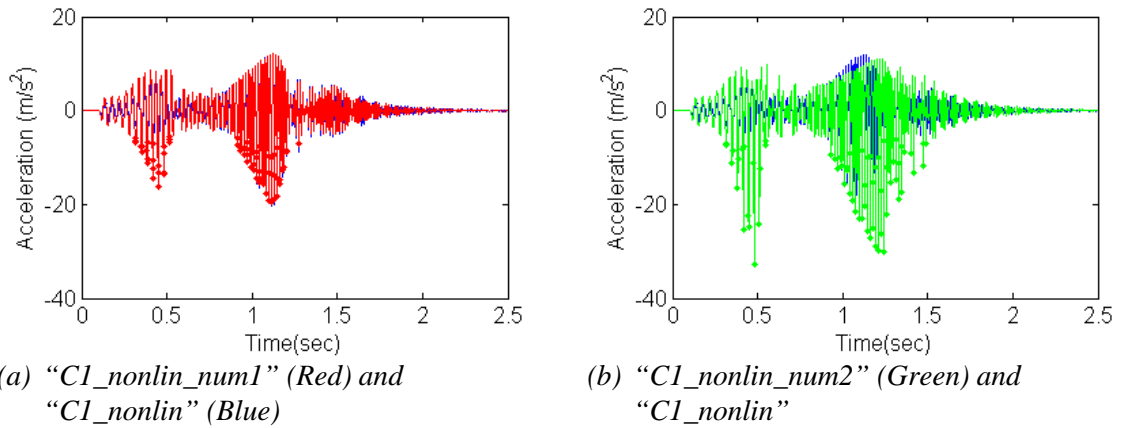


Figure 18: Time-histories for chirp excitations applied to the nonlinear system.

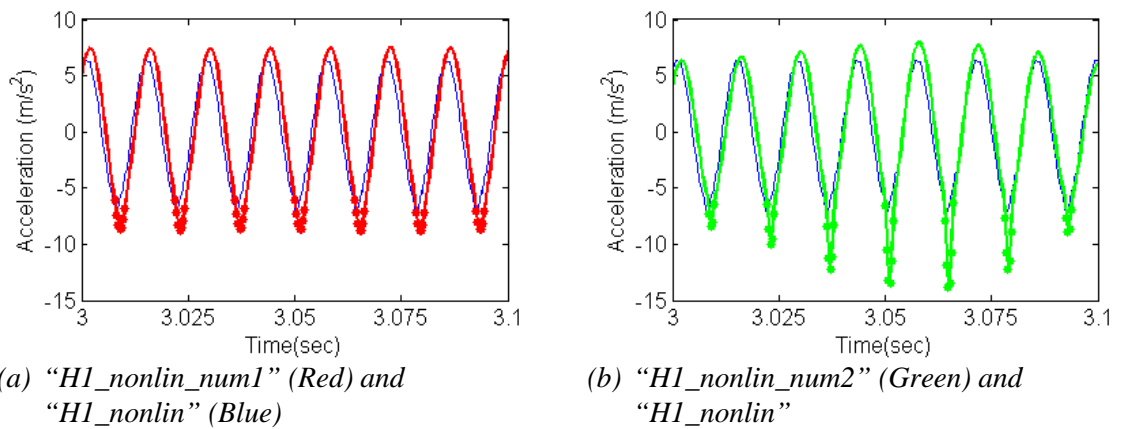


Figure 19: Time-histories for harmonic excitations applied to the nonlinear system.

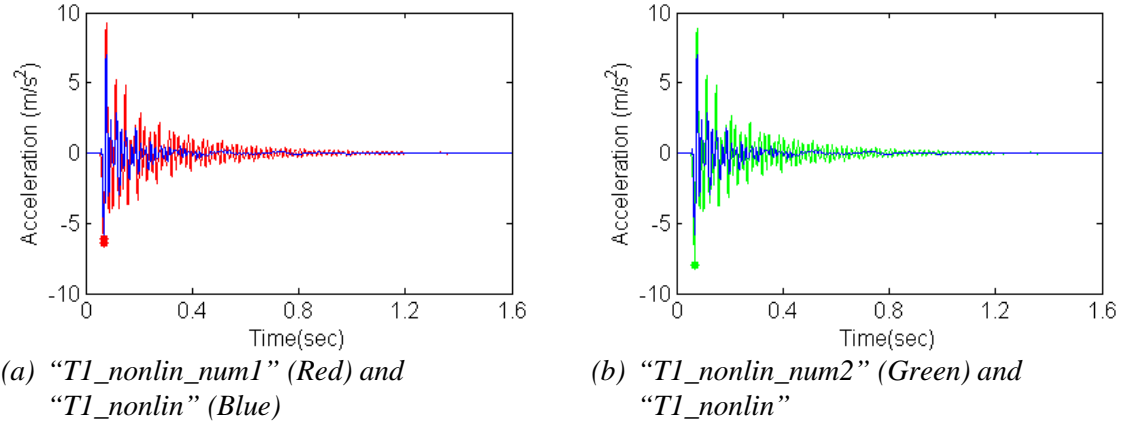


Figure 20: Time-histories for shaker transient excitations applied to the nonlinear system.

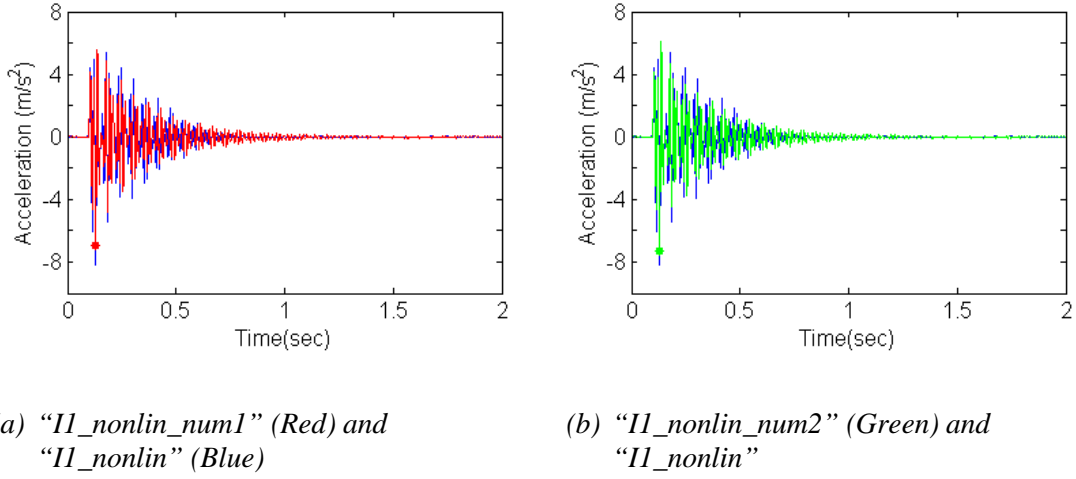


Figure 21: Time-histories for impact hammer excitations applied to the nonlinear system.

5. FEATURES FOR STRUCTURAL DYNAMICS MODEL VALIDATION

In this section some features used in the model validation process are introduced. One issue to consider when selecting a particular feature is its sensitivity to the target model parameters that most influence the numerical outputs, which may be different depending on the intended purpose of the analysis. The feature dimensionality is another consideration that must be addressed when quantifying the similarity or difference between measured and experimental values and when quantifying the statistical distribution of the features. Furthermore, feature selection should reflect the type of response that is being considered, e.g., linear or nonlinear, stationary or non-stationary. Some of features used for various types of structural dynamics analyses are summarized below:

Stationary and Gaussian vibrations: modal parameters, frequency spectrum (power spectrum, transfer function), waveform (basic signal statistics, normal probability plot).

Transient dynamics and mechanical shock response: waveform (decrement and exponential decay measures), temporal moments, shock response spectrum.

General-purpose time-series analysis: AR, ARMA, ARX, AR-ARX models, time-frequency transforms, wavelet transform, principal component decomposition.

Unstable, chaotic, multiple-scale dynamics: Holder exponent, state-space maps, time-frequency and higher-order transforms, symmetric dot pattern, fractal analysis.

For the discussions herein the models are developed to predict the linear and nonlinear response of the test-bed three-story structure. The target uncertain parameters being investigated are the damping ratios and the nonlinearity modeling parameter Δ .

5.1. Modal Properties

Modal parameters are widely employed as features in linear structural dynamics model updating and structural condition assessment of linear systems (Doebling et al., 1996). The motivation behind the use of these parameters as features for structural dynamics model validation is that modal parameters (i.e., resonant frequencies, modal damping ratios, and mode shapes) are the functions of mass, damping, and stiffness of a structure. Therefore, a comparison of these parameters extracted from numerical and experimental data can be used to validate most aspects of a linear structural dynamics model.

There are two approaches in modal analysis: 1) the numerical modal analysis (Clough and Penzien, 1993), and 2) the experimental modal analysis (Maia and Silva, 1997). In the numerical modal analysis approach, the resonant frequencies and the mode shapes are derived from calculated eigenvalues and eigenvectors using the mass matrix [M] and the stiffness matrix [K] of a numerical model. Most often the damping matrix is neglected in these calculations. This analysis is often carried out for the first step to check the validity of a constructed numerical model. In the experimental modal analysis, the parameters are typically determined from the FRF or the impulse response functions estimated from measured input and output data (Maia and Silva, 1997). The peaks in FRFs indicate resonant frequencies, and the damping ratios can be derived from the width of the FRF around each peak. Relative amplitude and phase information at the peaks of the FRF can be used to estimate the mode shapes. The model parameters are estimated by curve-fitting the parametric forms of the FRF to the FRFs derived from measured input and response time histories. In this study, the parameters were estimated by a rational-fraction polynomial curve-fitting method using Forsythe Orthogonal Polynomials (Richardson and Formenti, 1982); this algorithm is available in LANL's SHMTools software (SHMTools website).

Tables 13 and 14 summarize estimated resonant frequencies and damping ratios obtained from experimental and numerical data, corresponding to the random excitations: R1_lin, R1_lin_num1, and R1_lin_num2. Notice that the first mode of the test-bed structure is the rigid body mode associated with the structure sliding on the rails; therefore, the results are only presented for the second, third, and fourth modes. In the experimental modal analysis, FRFs were derived by using seven averages of a 1024 point window, with 50% overlap, and a Hanning window. The curve-fitting was then applied to the frequency band 20–80 Hz of the experimentally measured FRFs. Notice that the indicated values in Tables 13 and 14 are the averages of the results obtained from the ten time-histories.

In Table 13, it is first seen that the results of the experimental modal analysis applied to the numerical outputs under the random excitation, R1_lin_num1 and R1_lin_num2, show agreement with the values from the numerical modal analysis, as would be expected. However, both models

yield slightly higher values than the resonant frequencies estimated from the experimental data R1_lin, although the difference is quite small (less than 1.5%).

In Table 14 the estimated damping ratios obtained by the experimental modal analysis to data from the two numerical runs show good agreement with the damping ratios assigned in Model#L1 and Model#L2, which are presented in Table 6. When compared with the values from the experimental data, it can be confirmed that the damping ratios of Model #L2 are much closer to those of the actual structure. However, the second mode damping ratio is significantly higher than the value obtained from the experimental data.

Table 13: Resonant Frequencies (Hz) from Experimental and Numerical Modal Analysis

Mode #	Experimental Modal Analysis			Numerical Modal Analysis
	R1_lin	R1_lin_num1	R1_lin_num2	
Second	29.40	29.82	29.83	29.80
Third	54.25	54.88	54.88	54.92
Fourth	71.34	71.62	71.62	71.61

Table 14: Damping Ratio (%) from Experimental Modal Analysis

Mode #	Experimental Modal Analysis		
	R1_lin	R1_lin_num1	R1_lin_num2
Second	3.26	1.39	5.08
Third	1.07	1.18	1.18
Fourth	0.73	1.16	1.16

Figure 22 shows the comparisons of mode shapes obtained from the same numerical runs and from the experimental data. Results from the two numerical runs almost completely overlap, but appear to disagree with the results from the experimental data. One common technique for making quantitative comparisons of mode shapes is the modal assurance criterion (MAC) (Allemand, 2003), which is defined as follows:

$$MAC_{ij} = \frac{(\{\phi_N\}_i^T \{\phi_E\}_j)^2}{(\{\phi_N\}_i^T \{\phi_N\}_i)(\{\phi_E\}_j^T \{\phi_E\}_j)}, \quad (8)$$

where subscripts *N* and *E* refer to numerical and experimental, respectively, and *i* and *j* indicate the particular mode shape vectors that are being compared. The MAC value is bounded between 0 and 1 with values close to 1 indicating close correlation. Examination of Eq. 8 shows that the MAC values are not influenced by a constant scaling of one mode shape. This insensitivity to a constant scaling parameter can be seen in Fig. 23 where the MAC values comparing the same modes extracted from experimental and numerical data are all very close to 1 even though differences in Modes two and four can be seen in Fig. 22. Although the amplitudes for Modes two and four in Fig. 22 are different, the shapes are only different by constant scaling factor.

Upon observing the modal properties from both the numerical runs and the experimental data, it can be said that the response from Model #L2 is more similar to the response measured on the

structure. However, these parameters have some limitation as features for use in the model validation. First, they are the function of mass and stiffness parameters of a linear system, and for response from a stationary excitation process. Moreover, the modal parameter estimation process is influenced by noise in the measured data, and variability in the testing procedures, the FRF estimation process, and the curve-fitting process. For instance, one should notice that using a Hanning window to estimate FRFs tends to bias damping ratio estimates and yields values higher than those that are actually present (Maia and Silva, 1997). As will be the case with most features used for model validation purposes, one must be cognizant of the assumptions that are being made when extracting modal parameters using experimental modal analysis procedures, and the sources of variability associated with those parameter estimation techniques.

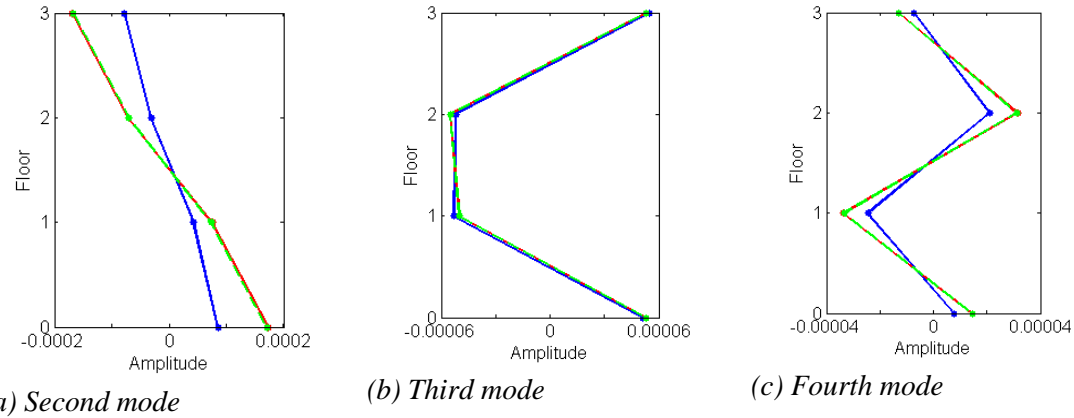


Figure 22: Comparison of estimated mode shapes from the experimental modal analysis (Blue: R1_lin, Red: R1_lin_num1, Green: R1_lin_num2).

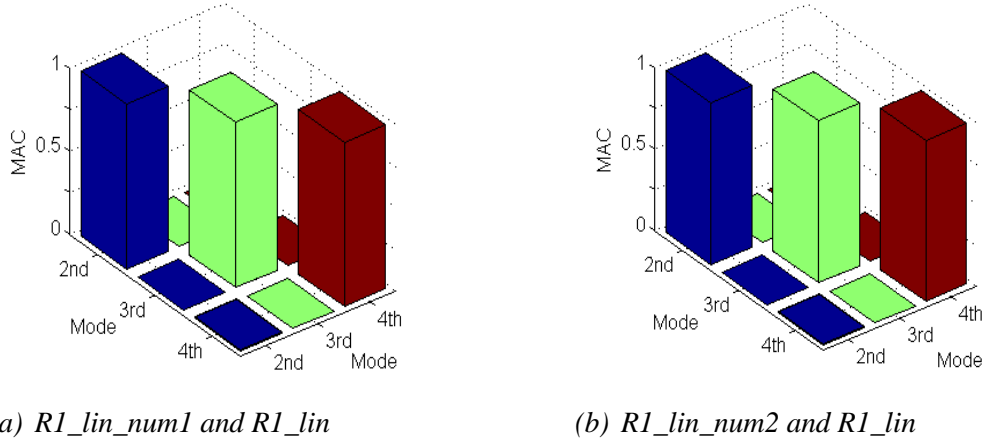


Figure 23: MAC comparing mode shapes obtained by the experimental modal analysis.

5.2. Waveform Analysis

Features from the waveform analysis can directly compare the time-histories in a quantifiable manner. Various waveform analysis techniques are presented here. All of these techniques can be applied to the responses from both linear and nonlinear systems as well as stationary and non-stationary processes. Many of these features were developed for a specific type of response (e.g., the basic statistics for random responses, Crest/K-factors for harmonic signals, and temporal moments for transient responses).

5.2.1. Basic Statistics

The peak amplitude, mean, root mean square (RMS), standard deviation (STD), skewness, and kurtosis are often used as features to quantify the waveform of time-history data (Walpole et al., 2012). Definitions of the basic signal statistics for data x_i ($i=1, \dots, N$) are presented in Table 15. Notice that the RMS value becomes equal to the STD when the mean value μ_x is zero. The statistical measures of mean and STD define a normal distribution, whereas measures of skewness and kurtosis are often used for the evaluation of normality because they take on the values of 0 and 3, respectively, for a normal distribution. It is also possible to use these same features to compare the waveform even though the signal does not have a normal distribution.

Table 15: Definition of the Basic Signal Statistics

Peak amplitude: X^{peak}	$X^{\text{peak}} = \max x_i $
Mean: μ_x	$\mu_x = \frac{1}{N} \sum_{i=1}^N x_i$
Root Mean Square: X^{rms}	$X^{\text{rms}} = \sqrt{\frac{1}{N} \sum_{i=1}^N (x_i)^2}$
Standard Deviation: σ_x	$\sigma_x = \sqrt{\frac{1}{N} \sum_{i=1}^N (x_i - \mu_x)^2}$
Skewness: S_x	$S_x = \frac{1}{\sigma_x^3} \cdot \frac{1}{N} \sum_{i=1}^N (x_i - \mu_x)^3$
Kurtosis: K_x	$K_x = \frac{1}{\sigma_x^4} \cdot \frac{1}{N} \sum_{i=1}^N (x_i - \mu_x)^4$

Figure 24 shows peak amplitude X^{peak} , mean μ_x and STD σ_x from the random and chirp responses from the linear system. The STD and mean value are sensitive to the global amplitude and bias (or constant offset) of a waveform. The peak amplitude gives more local characteristic of the signal. Therefore, it is considered to be more suitable to use with the chirp signal to investigate the amplitude at the most responsive frequency, which is a local characteristic. When using these features for waveform comparison, the length and sampling frequency of the signal should be constant.

Figure 25 presents the plots of basic statistics from random responses of the linear system; the error bars indicate ± 1 standard deviation (STD) from the mean of the respective statistic obtained from the ten time histories. When a normally-distributed random input signal is applied to a linear system, the responses will also be normally distributed signals (Wirshing, et al., 1995). Accordingly, the skewness, and kurtosis show the appropriate values that are consistent with this assumption (i.e., the values are close to 0 and 3, respectively). However, significant sensitivities of these features to the different of models (between R1_lin_num1 and R1_lin_num2) are not seen. On the other hand, the peak amplitude, STD, and RMS (almost the same as STD because the means of signals are near zero) indicate the waveform similarity between the numerical run and the experimental data. Because these three features are related to the amplitude of signal, they can reflect differences in the damping ratios used in the different models. From these results, it can then be seen that the damping parameters in Model #L2 are much closer to those exhibited by the actual test-bed structure than the damping values specified for Model #L1.

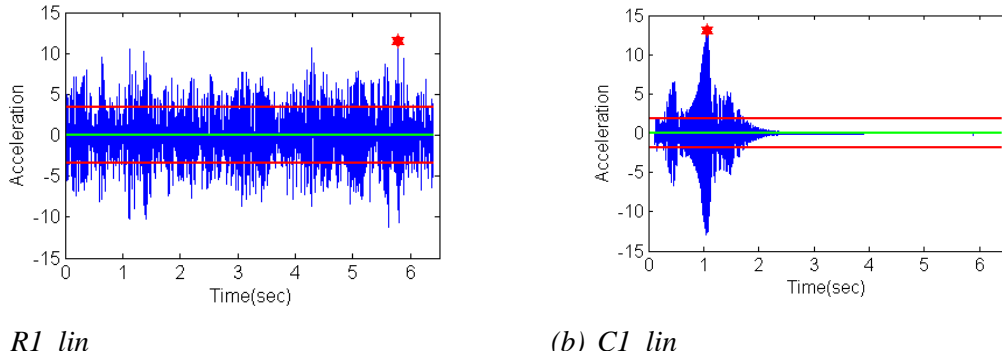


Figure 24: Extracted peak amplitude (red star), mean (green line), and STD (red lines) in the random and chirp responses in the linear system.

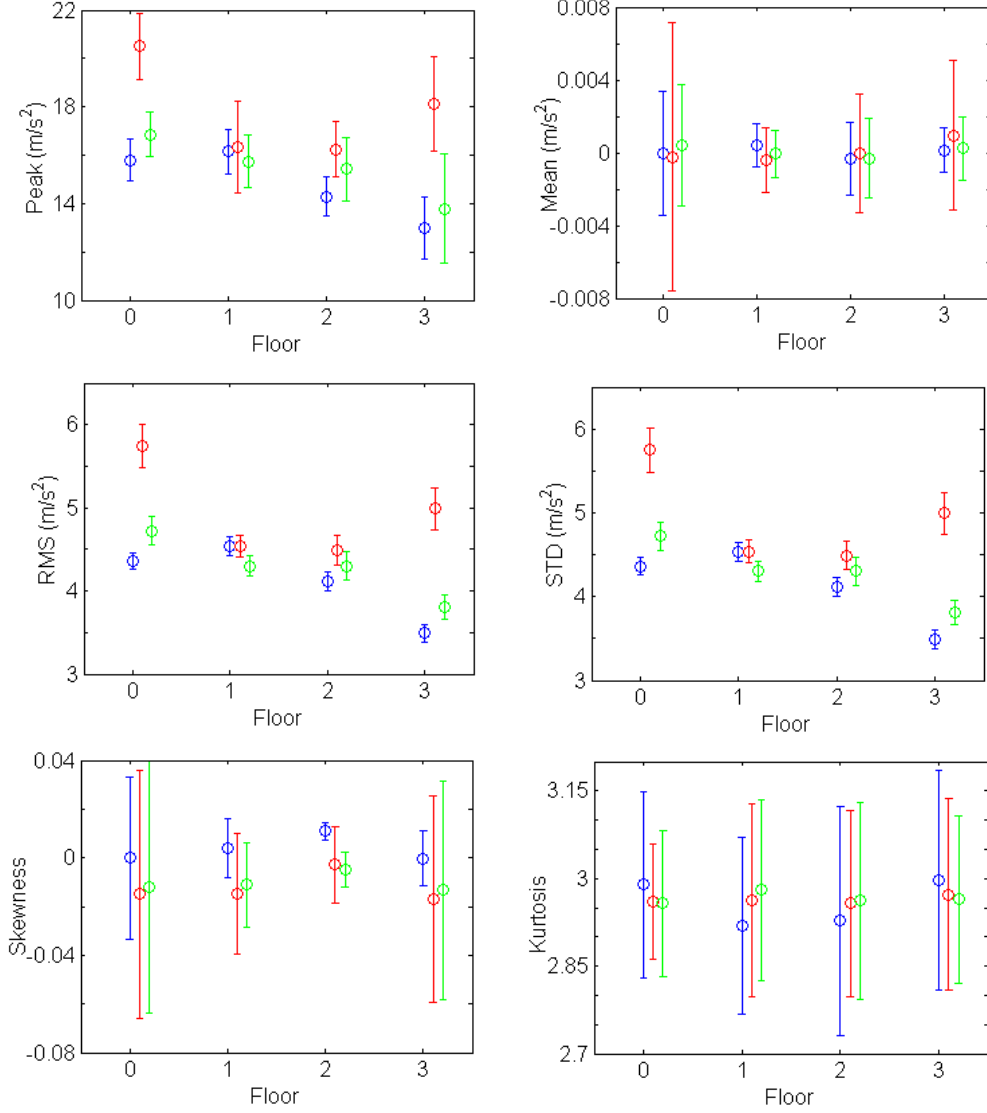


Figure 25: Basic statistics of random responses from the linear system (Red: R1_lin, Blue: R1_lin_num1, Green: R1_lin_num2)

For the nonlinear system, not only the peak amplitude, RMS and STD, but also the skewness and kurtosis show the sensitivities to differences in the parameter Δ , as shown in Fig. 26. It can be seen that all of these features from R1_nonlin_num1 (Model #N1) show values closer to those from the experimental data compared to the values from R1_nonlin_num2 (Model #N2). In the plots of the RMS and STD, the result of each of the four floors shows similar sensitivity to the difference in modelling and therefore these two features can globally indicate the differences between these two models. On the other hand, the skewness and kurtosis from R1_nonlin_num2 (Model #N2) are much higher when compared with the other numerical run and the experimental data. These results indicate that the Model #N1 provides a predicted response that is closer to the experimental one. Further investigation is needed to determine if these features can provide measures of model validity with appropriate sensitivities. It can also be seen that the parameter Δ influences the amplitude of response associated with the impact events. These impact events are a very local phenomena in space and time. As such, the peak amplitude can provide information

regarding the validity of parameter Δ and also the location of the bumper mechanism in the actual structure.

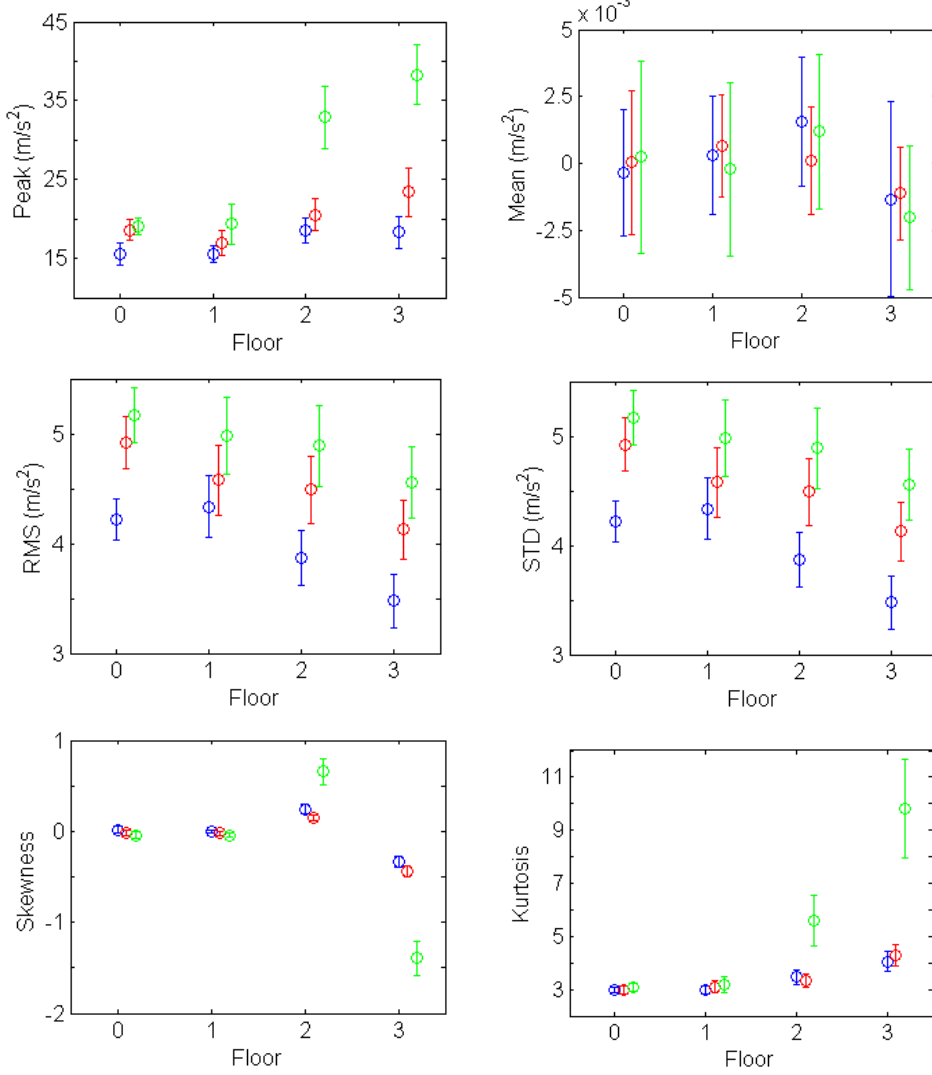


Figure 26: Basic statistics from random responses in the nonlinear system (Red: R1_nonlin, Blue: R1_nonlin_num1, Green: R1_nonlin_num2).

In general, these basic statistics provide a global measure of the waveform characteristics. Therefore, one must consider if the target model parameter to be validated are sensitive to the global waveform properties. All of the basic statistics are one-dimensional. Therefore, it is expected that several of these statistics can be combined into a multi-dimensional feature vector to better validate uncertain model parameters.

5.2.2. Normal Probability Plot and Probability Density Distribution

As previously mentioned, when the input is a normally distributed random signal, the response of a linear system will also have a normal distribution. Therefore, the normal probability plot (NPP) and probability distribution function (PDF) will be used to assess the normality of the response (Chambers et al., 1983).

To construct an NPP, the n acceleration amplitudes forming the input or response time history are first rank-ordered from smallest to largest. Next, the sequential order is normalized by the total number of points, and the j th rank-ordered point is calculated as $j/(n+1)$. The amplitude is then plotted against the corresponding normalized value with the vertical axis of the plot scaled for the assumed distribution. If the data correspond to the assumed distribution, a linear plot will result; but if the data are related to another PDF, they will introduce curvature in the plot. The slope of a plot indicates the range of distributions, and these plots help to understand the distribution of outliers (Montgomery, 1996).

Non-parametric PDF estimation is another technique used to assess the underlying distribution of the data. In statistics, the histogram density estimator and the kernel density estimator are two common techniques used to estimate an unknown underlying PDF of a random variable based on sampled data. Although the former is the oldest and most widely used form of density estimation, the latter provides a more general and improved treatment of the problem, and therefore is used in this study. When data from a sample of a population is given, the kernel density estimator draws inferences about the entire population being studied (Silverman, 1986). Considering a series from a random variable with n observations, x_1, \dots, x_n , the estimated density distribution $f(x)$ is given at any point x by

$$f(x) = \frac{1}{nh} \sum_{i=1}^n K\left(\frac{x - x_i}{h}\right), \quad (9)$$

where $K(\cdot)$ is the kernel function and h is the bandwidth, also called the smoothing parameter. Although there are many choices among kernels $K(\cdot)$, a standard Gaussian function with a zero mean and unit variance is adopted here:

$$K(x) = \frac{1}{\sqrt{2\pi}} e^{-\frac{1}{2}x^2}. \quad (10)$$

One of the most important factors for a good kernel density estimator is the choice of the smoothing parameter h . The quality of the kernel estimate depends less on the shape of the kernel function than on the value of its bandwidth. A value of h that is too small, for example, is not useful because such values lead to “spiky” estimates, and the kernel density estimate is said to be undersmoothed. On the other hand, large values of h lead to flat estimates and the kernel density estimate is said to be oversmoothed. Several techniques to estimate the optimum value for h can be found in (Browman, 1984). For comparisons between waveforms from numerical and experimental responses, these factors should be kept constant.

Figures 27 and 28 show NPPs of the responses associated with random excitations applied to the linear and nonlinear systems, respectively. In addition, Fig. 29(a) and (b) illustrate the individual estimates of PDFs based on the kernel density estimator are derived from the same random responses. From the NPPs in the linear case in Fig. 27, all data points fall close to the dashed line as would be expected because, as previously mentioned, the outputs of a linear system subjected to a normally distributed random input should also show a normal distribution. Examining the slope of each line, the result from “R1_lin_num2” is closer to that of the experimental data compared to the result from “R1_lin_num1”. The agreement between the distributions of the numerical run and the experimental data can also be investigated by the profiles of estimated PDFs as shown in Fig. 29(a). It can be said that the estimated PDF from _lin_num2 (Model #L2) is much closer to that from the experimental data.

When subject to a normally distributed random input, the response data from the nonlinear systems are not expected to have a normal distribution. In Fig. 28, the NPPs show the bilinear behaviors, in which the plots less than -5m/s^2 are not distributed on the dashed lines, but on the other line. Such bilinear responses are caused because the system oscillates between two different linear stiffness states; with and without the stiffness of the bumper mechanism. Therefore, the profile of the NPP indicates a characteristic of the nonlinear responses. Comparing the NPP profile of the response under the impact events, the slope in the result of R1_nonlin_num2 (Model #N2) is obviously larger than that of the experimental data. The same discussion is applicable in the estimated PDFs shown in Fig. 29(b). The longer tail associated with the estimated distribution in R1_nonlin_num2 indicates that the calculated run from Model #N2 overestimates the amplitudes during the impact events due to the small value of Δ . Also here, it can be said that the response from Model #N1 is closer to that from the experimental data in the case of the nonlinear system.

It can then be concluded that the NPP and the PDF can provide a measure of the validity of the linear and nonlinear models when the random responses are analyzed. However, these features are of high-dimension; therefore, other lower dimensional features should be extracted. For instance, one can calculate the slope of the linear line of the NPP, which yields a one-dimensional feature. For the nonlinear system, the range of the tails of estimated PDF is a function of the bumper mechanism. One should note that the features for extracting the characteristics of distribution tails represent the global nonlinearity (i.e., there is no time or frequency information associated with these features.)

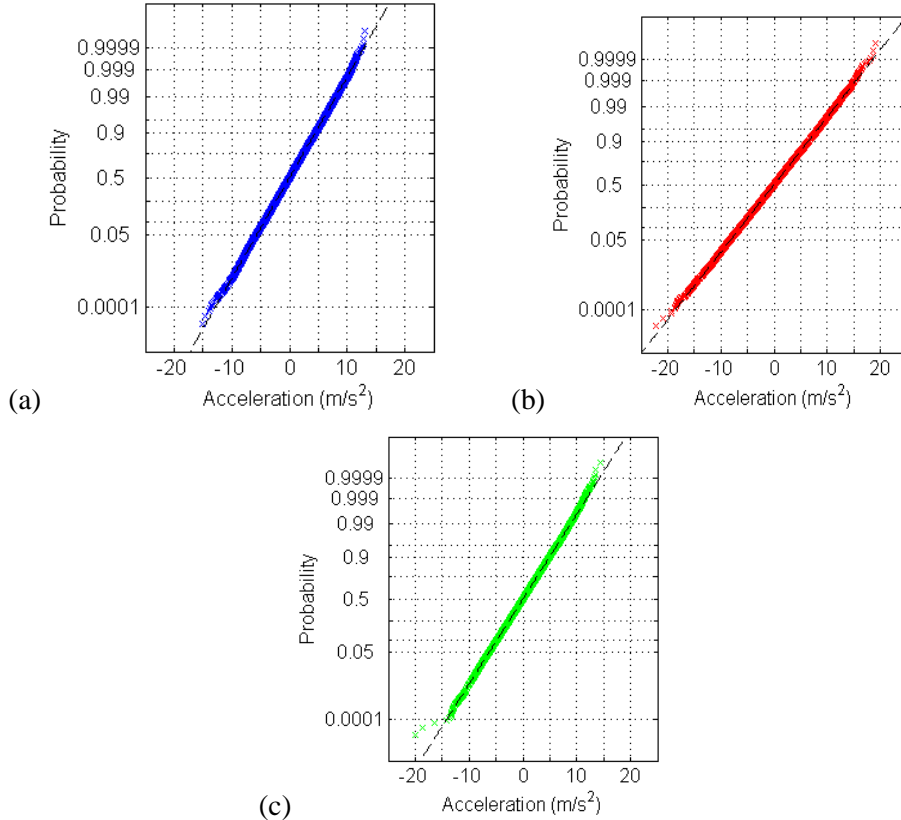


Figure 27: NPPs from the linear system; (a) R1_lin, (b) “_lin_num1, (c) R1_lin_num2.

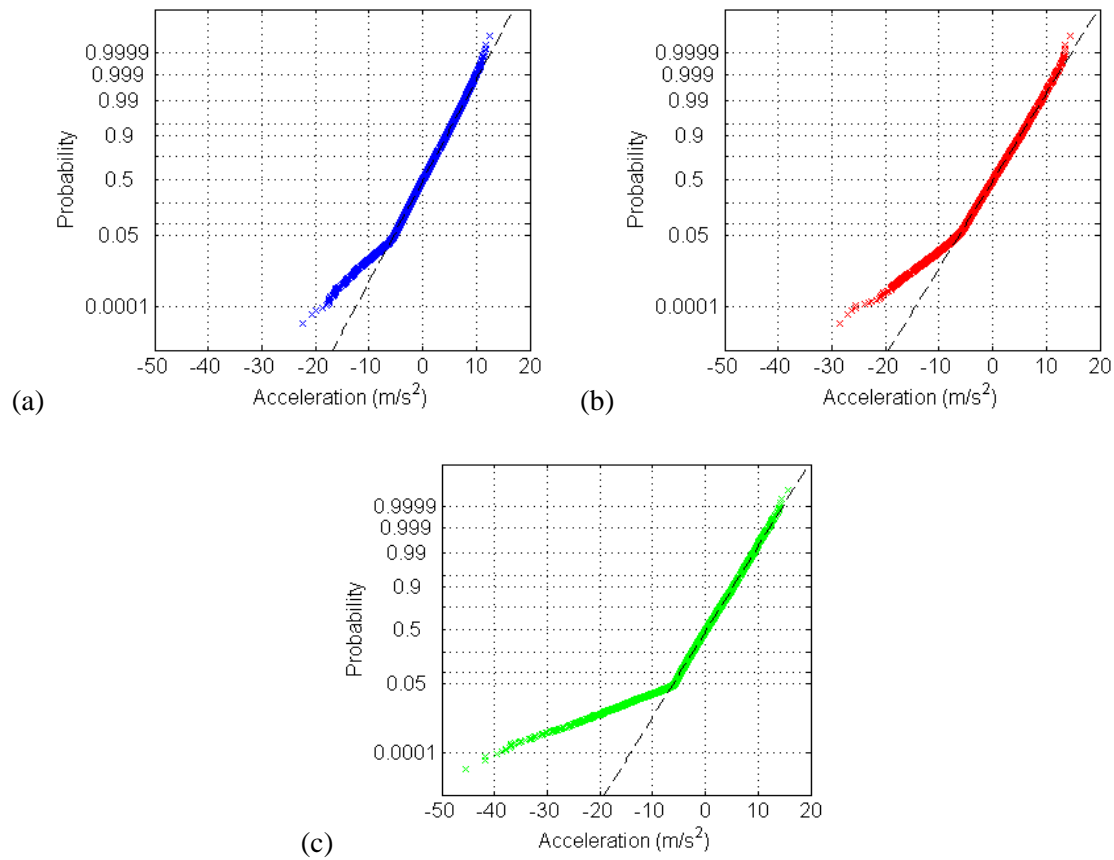


Figure 28: NPPs from the nonlinear system; (a) $R1_nonlin$, (b) $R1_nonlin_num1$, (c) $R1_nonlin_num2$.

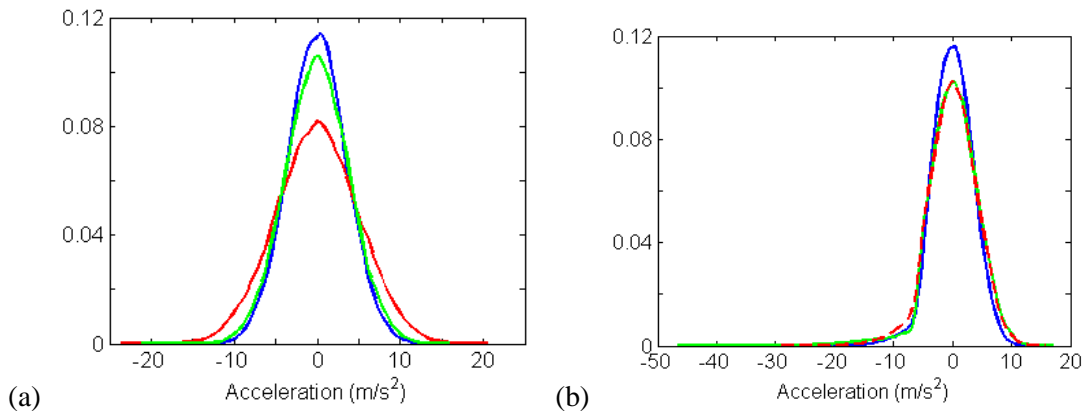


Figure 29: Estimated PDFs; (a) Linear system (Blue: $R1_lin$, Red: $R1_lin_num1$, Green: $R1_lin_num2$), (b) Nonlinear system (Blue: $R1_nonlin$, Red: $R1_nonlin_num1$, Green: $R1_nonlin_num2$).

5.2.3. Crest Factor and K-Factor

Crest factor X^{cf} and K-factor X^{kf} are used to diagnose the deviation from sinusoidal response in a harmonic signal (Mitchell, 1993). These values are defined using peak amplitude X^{peak} and RMS values X^{rms} as

$$X^{cf} = \frac{X^{peak}}{X^{rms}} \quad (11)$$

and

$$X^{kf} = X^{peak} X^{rms}. \quad (12)$$

The crest factor has a theoretical value 1.414 for a complete sine-wave. From these definitions it can be said that the crest factor indicates the local deviation from a sinusoidal profile; on the other hand, the K-factor represents the global amplitude level of the signal.

Figure 30 shows the crest factors derived from the responses from both the linear and nonlinear systems, corresponding to the harmonic base excitations. The error bars are the ± 1 STD from the mean of the values extracted from the ten time histories. All of calculated crest factors from the linear system, presented in Fig. 30 (a), show a value near 1.41. The insensitivity of this feature to the different second mode damping ratios specified in Model #L1 and #L2 is to be expected because the input force frequency is close to the fourth mode resonant frequency. On the other hand, this feature has a significant sensitivity to the nonlinearity. The crest factors from H1_nonlin_num1 clearly show good agreement with those from the experimental data, as shown in Fig. 30 (b). This result is due to the loss of the sinusoidal waveform caused by the impact events at the bumper mechanism. This result implies that this feature can be used to analyze nonlinearities that introduce local waveform distortion under harmonic input.

The calculated K-factors using the same harmonic data are shown in Fig. 31 where again the error bars indicate ± 1 STD from the mean of this feature when extracted from ten time-histories. Note that these values are normalized by the K-factor of the input signals. For the linear system depicted in Fig. 31(a), the K-factors from the two numerical runs are considerably different from those extracted from the experimental data. This result is consistent with the global amplitudes of the harmonic responses in Model #L1 and #L2 being lower than the amplitude of experimental data as seen in Fig. 14. Again, this result is related to the fact that the excited mode here was the fourth mode, for which the two models have the same damping ratio. In the results from the nonlinear system, shown in Fig. 31 (b), the calculated K-factors do not show significant sensitivities to the difference in the models' nonlinearity parameter. This result is attributed to the fact that the nonlinearity associated with the bumper mechanism is a local phenomenon, therefore it does not influence the global amplitude level of the signal.

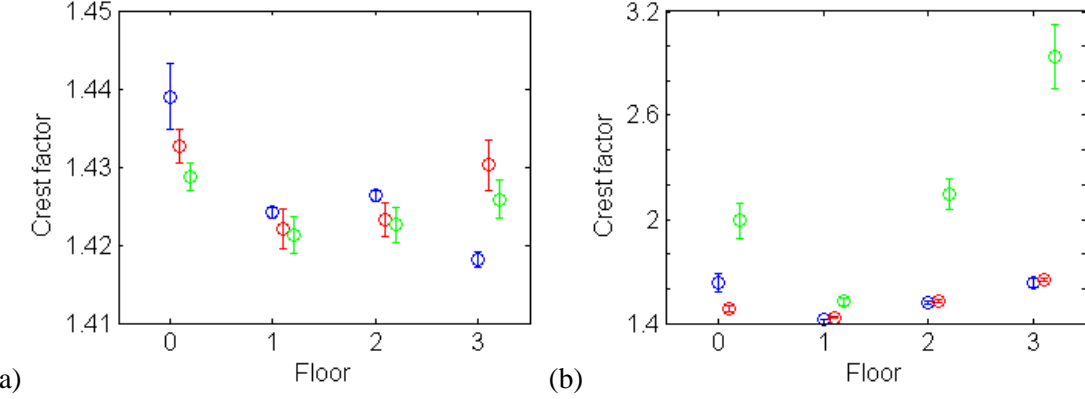


Figure 30: Crest factor; (a) Linear system (Blue: $H1_lin$, Red: $H1_lin_num1$, Green: $H1_lin_num2$), (b) Nonlinear system (Blue: $H1_nonlin$, Red: $H1_nonlin_num1$, Green: $H1_nonlin_num2$).

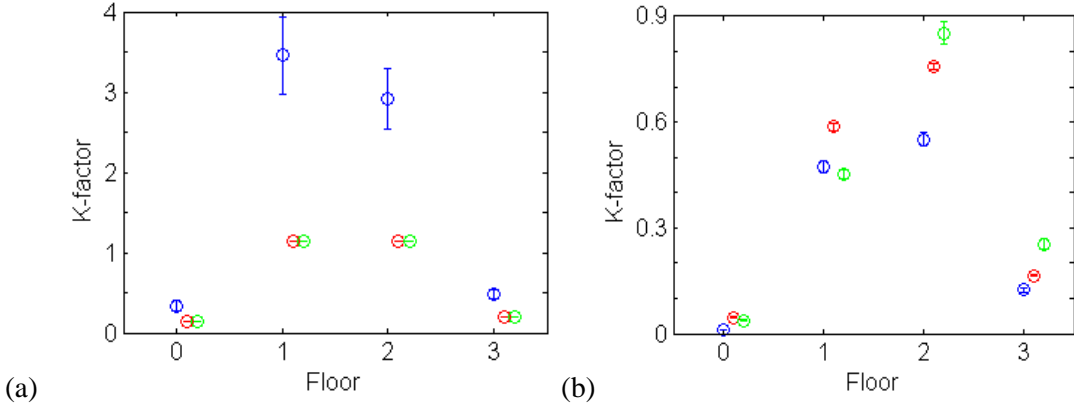


Figure 31: K-factor; (a) Linear system (Blue: $H1_lin$, Red: $H1_lin_num1$, Green: $H1_lin_num2$), (b) Nonlinear system (Blue: $H1_nonlin$, Red: $H1_nonlin_num1$, Green: $H1_nonlin_num2$).

5.2.4. 10% Duration and Exponential Decaying Function Fitting

Two features that can be used to investigate waveforms of responses resulting from transient excitations are presented here. One such feature, the 10% duration feature, is defined as the time between the instant of the peak response caused by the shock arrival at the sensor, and the instant that the waveform has decayed to 10% of the peak value (Mulville, 1999 and NASA Technical Standard Report, 1996). Figure 32 illustrates this feature on the data acquired from the shaker transient experiment. The time duration between the black point and the red point reflects the damping characteristics of structural system. Figure 33 shows the extracted 10% duration extracted from the transient response data, corresponding to the linear structures. The error bars represent ± 1 STD from the mean value of this feature extracted from the ten time histories in each case. In almost all cases, the values from the experimental data are very consistent with the data from the numerical models. It should be noticed that this feature, which is a function of the system's energy dissipation characteristics, is derived from a much more limited amount of data points compared to other energy dissipation measures such as the damping ratios (summarized for the linear system in Table 14) that are estimated from the entire time history.

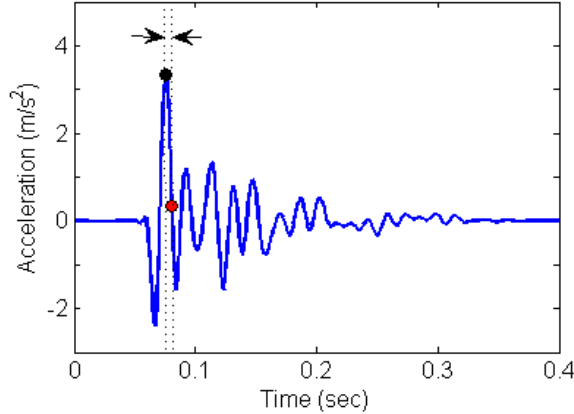


Figure 32: 10% duration of transient signal T1_lin.

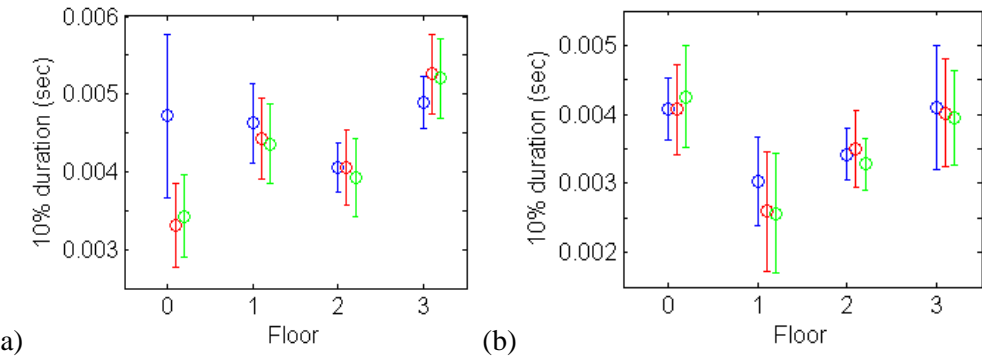


Figure 33: 10% durations from transient signals; a) Shaker transient excitation (Blue: T1_lin, Red: T1_lin_num1, Green: T1_lin_num2), b) Impact hammer excitation (Blue: II_lin, Red: II_lin_num1, Green: II_lin_num2).

A feature based on the decay curve is obtained by fitting an exponential function to data points that represent the local peaks of the transient response signal (Liu and Goetius, 2001 and Feldman, 2011). This feature is expected to provide a more global representation of the system's damping properties. The function that is fit to the transient data is

$$y(t) = y_0 e^{at} \quad . \quad (13)$$

Intercept y_0 and decay constant a represent the peak amplitude level and the global damping characteristic of the transient signal, and they can thus be used together as a low-dimension feature vector. An estimated decay curve for one of the transient signals from Channel #5 is shown in Fig. 34. The Hilbert transform was used here to extract an enveloping decay function and the exponentially decaying function in Eq. (13) was fit to this enveloping function using the least-squares method. Figure 35 is the error bar plot (± 1 STD) of extracted coefficients y_0 and a from the responses of Channel #5 under both the shaker transient and the impact hammer excitations applied to the linear system. From the results in both cases it can be said that the intercept y_0 has little sensitivity to the waveform differences from the two numerical models. However, the extracted decay constant a is sensitive to the difference of damping parameters specified in the two numerical models, especially in the results from the shaker transient excitations. The results here show that these extracted waveform characteristics are significantly different when compared to the values obtained from the experimental data. When comparing

results from the shaker transient and impact hammer excitations these features are affected by the input. In the case of the impact hammer excitation, by virtue of the chosen impact location, the input was exciting the second mode vibration, which the previously discussed experimental modal analysis in Section 5.1, showed had a higher damping value than the third and fourth modes.

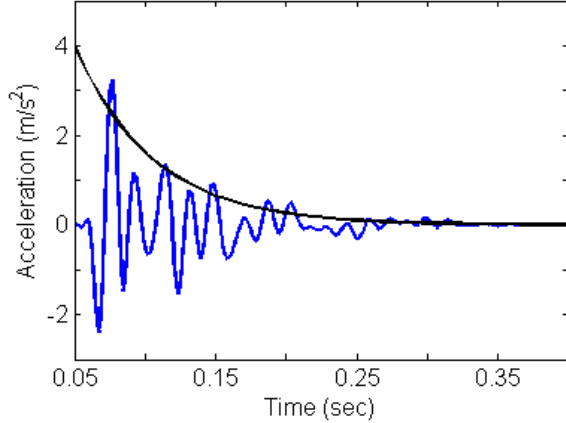


Figure 34: Estimated exponentially decaying function of transient signal T1_lin.

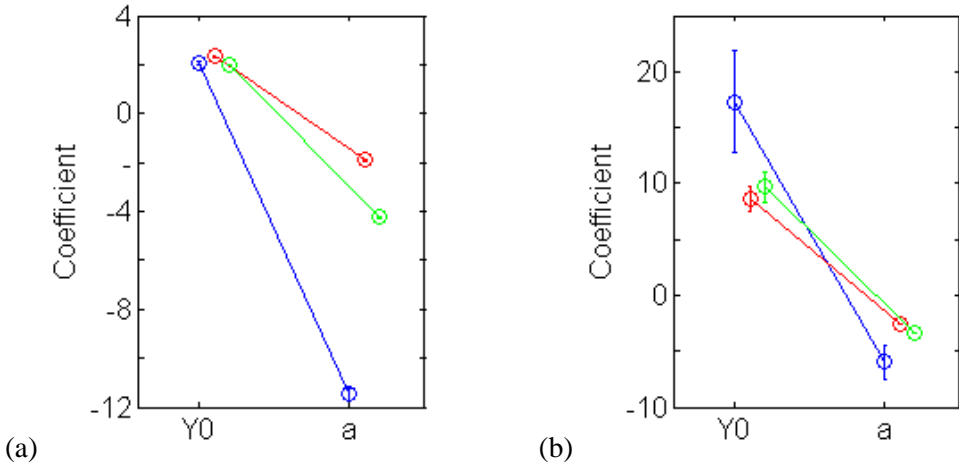


Figure 35: Estimated coefficients Y_0 and a of the Exponential decaying functions; (a) Shaker transient excitation (Blue: T_{1_lin} , Red: $T_{1_lin_num1}$, Green: $T_{1_lin_num2}$), (b) Impact hammer excitation (Blue: I_{1_lin} , Red: $I_{1_lin_num1}$, Green: $I_{1_lin_num2}$).

5.2.5. Temporal Moments

Temporal moments also provide information about the global waveform characteristics (Smallwood, 1994). Although they were initially developed to analyze transient signals, they can be applied to any type of waveform. For a time history, $x(t)$, the k^{th} order temporal moment, M_k , with delay time t_s is defined as

$$M_k(t_s) = \int_{-\infty}^{+\infty} (t - t_s)^k (x(t))^2 dt \quad . \quad (14)$$

For discrete data with the assumption of $t_s=0$, Eq. (14) can be rewritten as

$$M_k = \sum_{i=1}^N t_i^k x_i^2 . \quad (15)$$

The signal amplitudes are squared to define integral quantities that can be interpreted as “energy.” The values that are most often used for investigating waveforms are the zero-th to fourth order temporal moments, as summarized in Table 16. Energy E represents the total energy of the signal, which is also equal to the value of the auto-correlation function R_{XX} at zero delay time. The central time (Centroid) T represents the time shift t_s , when the first temporal moment becomes zero, described as $M_1(t_s=T)=0$. The physical interpretation is that, if the energy of signal is distributed along a pseudo time axis, then the value T is the centroid of this distribution. The RMS duration D describes the dispersion of waveform about central time T . For transient signals, a significant portion of the energy is often within two or three RMS durations of T .

Table 16: Definitions of the first five temporal moments

Energy: E	$E = M_0$
Central time: T	$T = \frac{M_1}{M_0}$
RMS duration: D	$D^2 = \frac{M_2(T)}{M_0}$
Central skewness: S	$S^3 = \frac{M_3(T)}{M_0}$
Central kurtosis: K	$K^4 = \frac{M_4(T)}{M_0}$

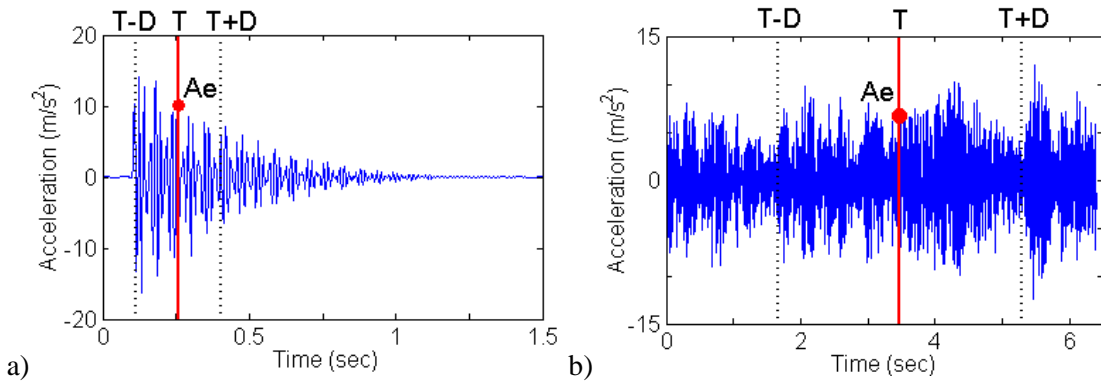


Figure 36: First three temporal moments on time-histories: a) T1_lin, b) R1_lin.

Three temporal moments E , T , and D are shown on the transient and random waveforms as shown in Fig. 36. The red point at $t=T$ in each figure is the root energy amplitude A_e that represents the overall amplitude of the signal; the definition of A_e is:

$$A_e = \frac{E}{D} . \quad (16)$$

By plotting T , D , and A_e , the time-average of the signal's amplitude, time-scale, and dispersion can be visualized. Figure 37 shows the error plots (± 1 STD from the mean of the features extracted from ten time histories) for the first five temporal moments of the response data obtained from the shaker transient excitations applied to the linear system. By observing the extracted temporal moments in this figure, with the exception of energy E , it can be seen that Model #L2 better predicts the structure's experimentally measured response. This result is obtained because these features represent the energy in a signal, which is sensitive to the decay rate of transient signals. Through the experimental modal analysis in Section 5.1 it was shown that Model #L2 provides a better approximation of the system's energy dissipation properties.

The error bar plots (± 1 STD) of the temporal moment features extracted from data in the random input case for the linear system are presented in Fig. 38. Energy E shows especially good sensitivity with respect to the accuracy of the numerical model, and the plot is similar to that of the peak value from the basic statistics shown in Fig. 25. This result is attributed to the peak value being related to the global power of the signal in the random response. The energy E is a more global and time-averaged feature to investigate the peaks of signals. Therefore, the sensitivity of E to the amplitude difference due to the nonlinearity is not significant, as shown in Fig. 39. The singularities imposed by the bumper system are local phenomena in time, and thus, other features that better capture this local time response are required to investigate the characteristics of this nonlinearity. The other temporal moments extracted from signals corresponding to the random inputs have little sensitivity to the different structural models. This result is to be expected because the energy of random signals is distributed almost uniformly across the full range of the time axis.

As a consequence, when using temporal moments to compare measured and predicted responses, one should recognize that they are global features. They are not well-suited to investigate characteristics of events that are local in time, such as the impacts that occur with the nonlinear system used in this study. On the other hand, T and D can be used as the features to describe the global characteristics of the transient signal's waveforms. This result indicates that in some cases these global features are suitable for the validation of structural dynamics models that produce transient signals.

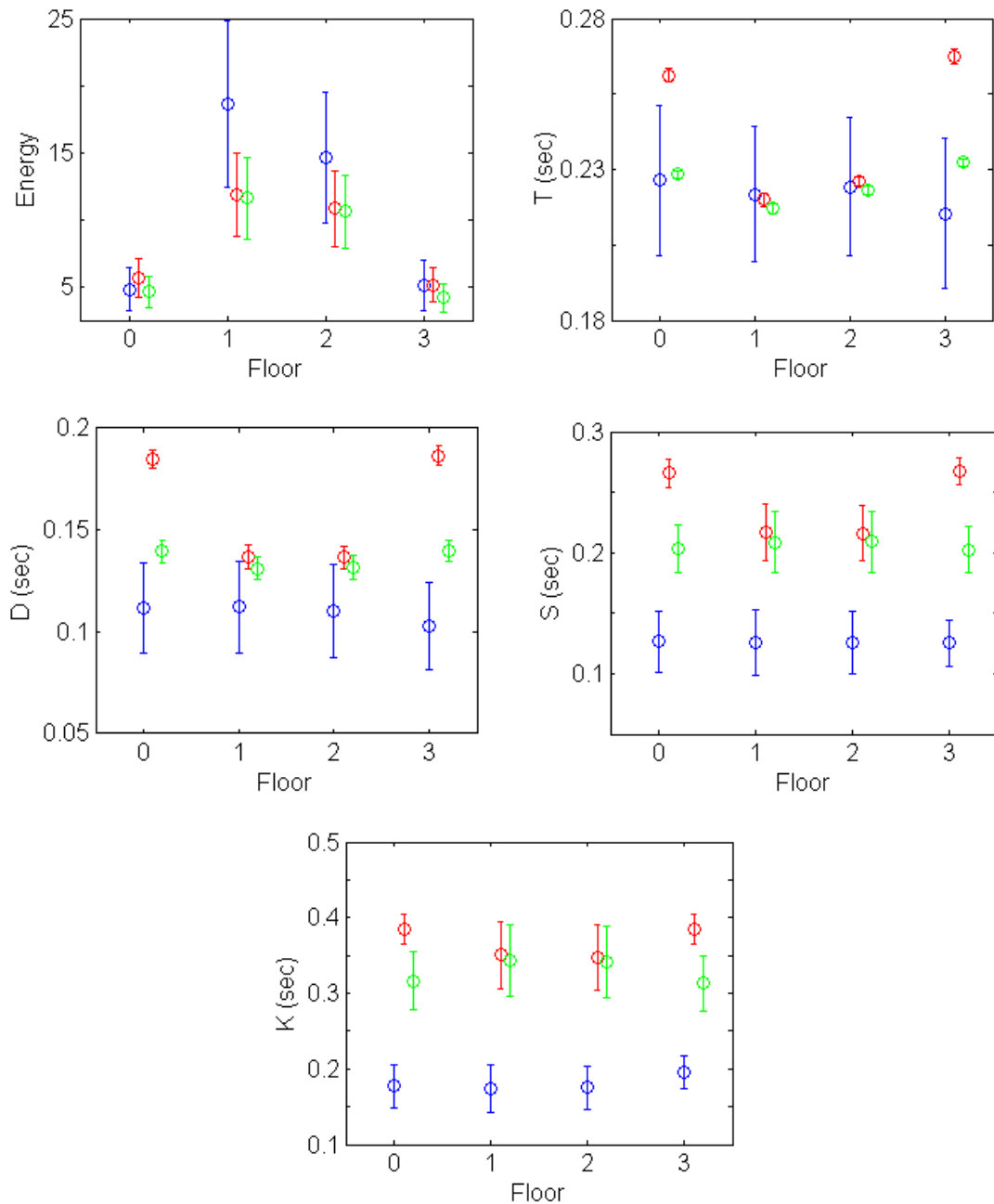


Figure 37: First five temporal moments of the linear system subjected to a transient input (Blue: *T1_lin*, Red: *T1_lin_num1*, Green: *T1_lin_num2*).

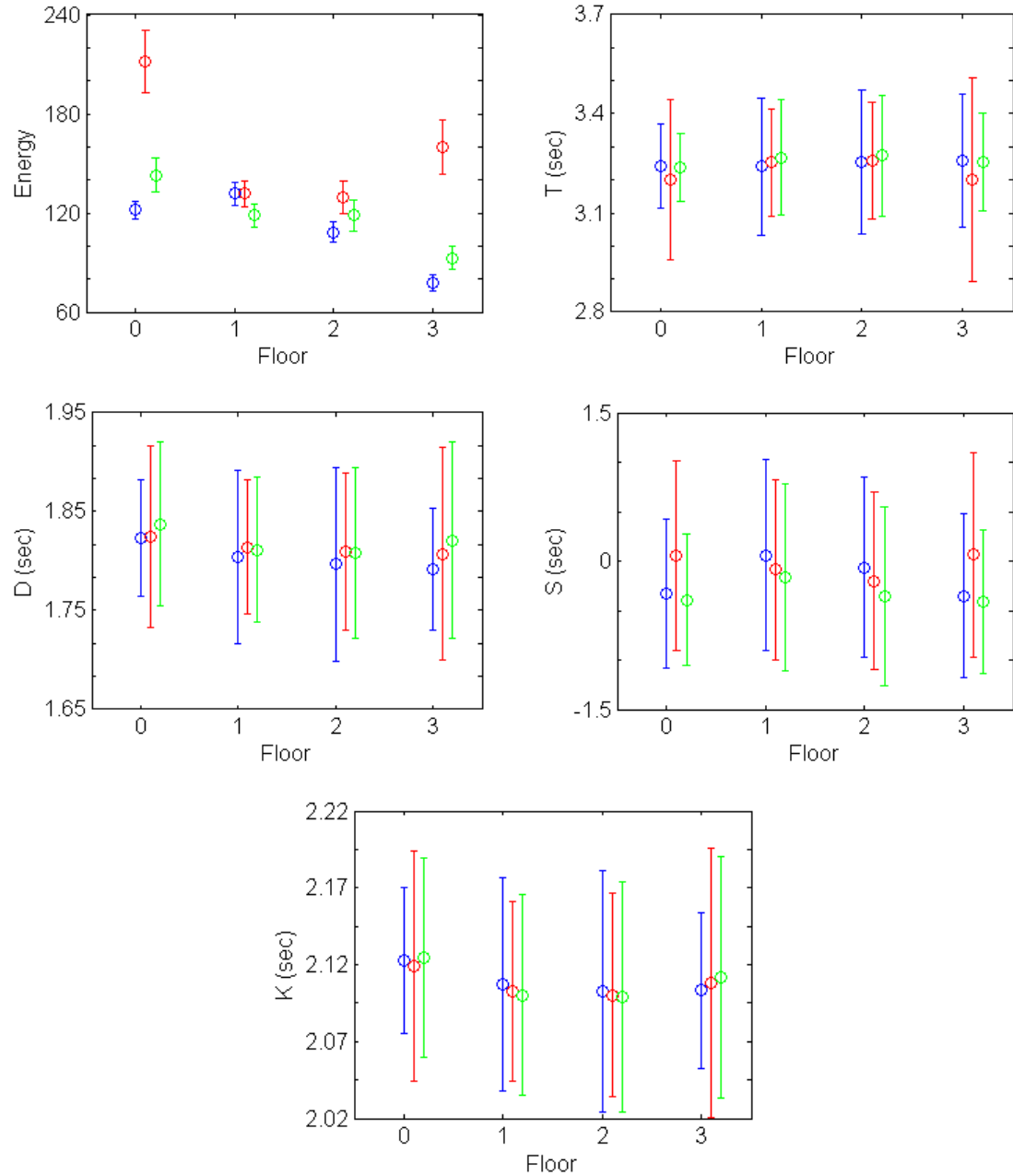


Figure 38: First five temporal moments of the linear system subjected to a random input (Blue: R1_lin, Red: R1_lin_num1, Green: R1_lin_num2).

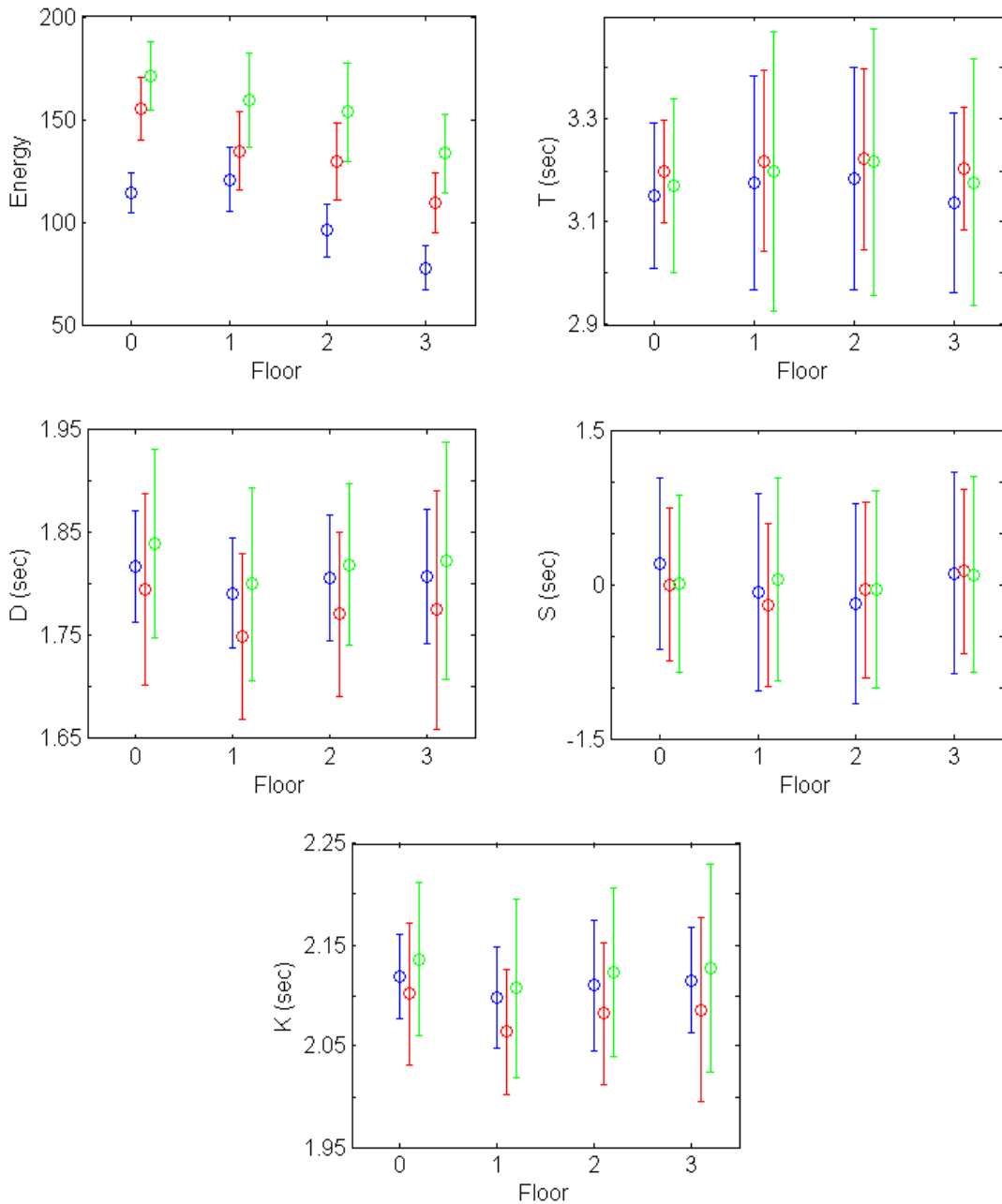


Figure 39: First five temporal moments of random signal in nonlinear system (Blue: R1_nonlin, Red: R1_nonlin_num1, Green: R1_nonlin_num2).

5.2.6. Autocorrelation Function and Correlation Coefficient

Correlation is a statistical technique used in signal processing for analyzing the relationship between two or more signals, or a single signal with itself at different time delays. Cross-correlation is a standard technique of estimating the degree to which two different signals are correlated (Wirsching et al., 1995 and Bendat, 1980). Considering two random variables x and y , the cross-correlation R_{xy} at delay or time lag τ is defined as

$$R_{xy}(\tau) = \frac{E[(x_t - \mu_x)(y_{t+\tau} - \mu_y)]}{\sigma_x \sigma_y}, \quad (17)$$

where μ_x and μ_y are the means of the random variables x and y , respectively, $E[.]$ is the mathematical expectation, and t is an integer representing a discrete-time process. The standard deviations of the variables, σ_x and σ_y , in the denominator, serve to normalize the range of the correlation. For a stationary process, values of the cross-correlation are in the range [-1, 1]. A coefficient equal to 1 indicates perfect correlation; i.e., the variables overlap when they are shifted by τ , whereas a coefficient of -1 indicates perfect anti-correlation, where the variables are completely out of phase when shifted by lag τ . An autocorrelation function is a function that yields the correlation of a signal with itself, and for the response vector x is defined as (Wirsching et al., 1995 and Bendat, 1980):

$$R_{xx}(\tau) = \frac{E[(x_t - \mu_x)(x_{t+\tau} - \mu_x)]}{\sigma_x^2}. \quad (18)$$

This function can be used to uncover repeating patterns within response data, such as the presence of periodic signals hidden by noise. Therefore, it is expected to have sensitivity to the frequency component of signals. As a general rule, it is sufficient to compute the autocorrelation for values of $\tau \leq N/4$, where N is the number of data points in the signal (Montgomery, 1996).

These functions are also expected to be used as features to compare the waveforms from experimental and numerical data. Figure 40 shows the overlays of the autocorrelation functions emanating from the linear system excited by a random input. Qualitatively, it is apparent that the pattern, i.e., frequency, resulting from R1_lin_num2 shows better agreement with the experimental data, than that of R1_lin_num1. The results from the nonlinear system, presented in Fig. 41, shows that the amplitudes of the autocorrelation function from R1_nonlin_num1 are a little closer to those from the experimental data compared with that from R1_nonlin_num2, especially in $\tau > 60$. However, it can be said that this feature is less sensitive to the waveform difference due to the local phenomena, i.e., the impact events in the nonlinear system. Additionally, the correlation function is a high-dimensional representation of the data; therefore, some metric is required to quantify the difference in these correlation measures.

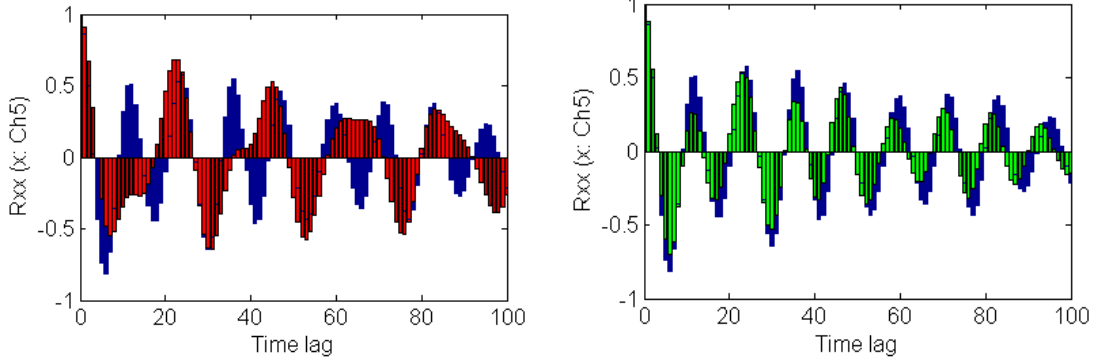


Figure 40: Autocorrelation functions of random signals in the linear system (Blue: $R1_lin$, Red: $R1_lin_num1$, Green: $R1_lin_num2$).

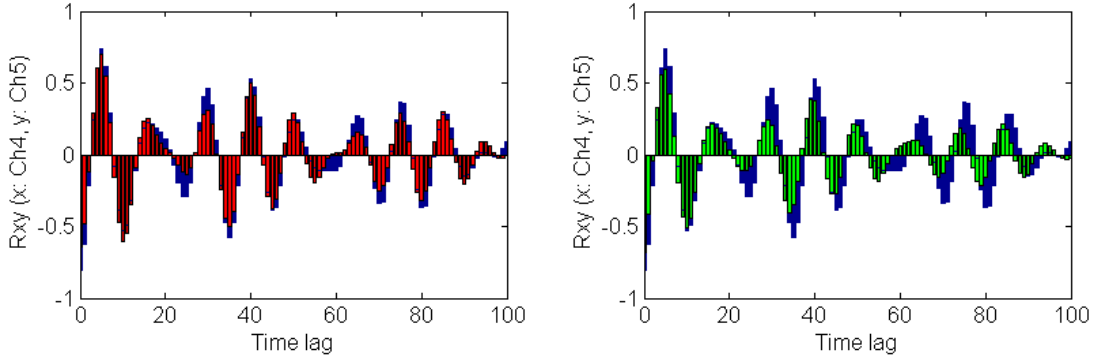


Figure 41: Autocorrelation functions of random signal in nonlinear system (Blue: $R1_nonlin$, Red: $R1_nonlin_num1$, Green: $R1_nonlin_num2$).

A correlation coefficient is a one-dimensional feature used to verify the correlation of two time-histories (Wirsching et al., 1995 and Bendat, 1980). The covariance matrix provides a convenient means of assessing correlation of higher dimension feature vectors and can be thought of as a generalization of the concept of the variance of a scalar-valued random variable to higher dimensions. Considering two random variables x and y , the covariance between those variables is given by

$$\text{cov}(x, y) = E[(x - \mu_x)(y - \mu_y)], \quad (19)$$

where $E[\cdot]$ is the mathematical expectation, and μ_x and μ_y are the means of the variables x and y , respectively. The correlation coefficient is then given by

$$\rho_{xy} = \frac{\text{cov}(x, y)}{\sigma_x \sigma_y}, \quad (20)$$

where σ_x and σ_y are the standard deviations of each variable. The concept of covariance can be extended to p -dimensional random variables in an analogous manner resulting in a $p \times p$ covariance matrix.

The correlation can be interpreted as a standardized covariance. The correlation coefficient is a zero-lag, normalized cross-correlation function given by Eq. (17). The unbiased estimator for the

correlation coefficient between x and y based on two samples of length N , sample standard deviations s_x and s_y , and samples means of \bar{x} and \bar{y} , is given by

$$r_{xy} = \frac{1}{(N-1)} \frac{\sum_{i=1}^N (x_i - \bar{x})(y_i - \bar{y})}{s_x s_y}. \quad (21)$$

This value can be used as the feature to compare two variables; for instance, the variables can be the time-histories from multiple sensor channels. Figure 42 shows three correlation coefficients, namely r_{25} , r_{35} , and r_{45} , calculated from data associated with random input to the linear and nonlinear systems (notice that the subscripts of the coefficients correspond to the channel numbers.) Considering both the linear system in Fig. 42(a) and the nonlinear system in Fig. 42(b), the calculated correlation coefficients from R1_lin_num2 and R1_nonlin_num1 show better agreement with the values from the experimental data, respectively. As in this example, the correlation coefficient is expected to be useful as a low-dimensional feature that can be used to compare the global responses of the structural system.

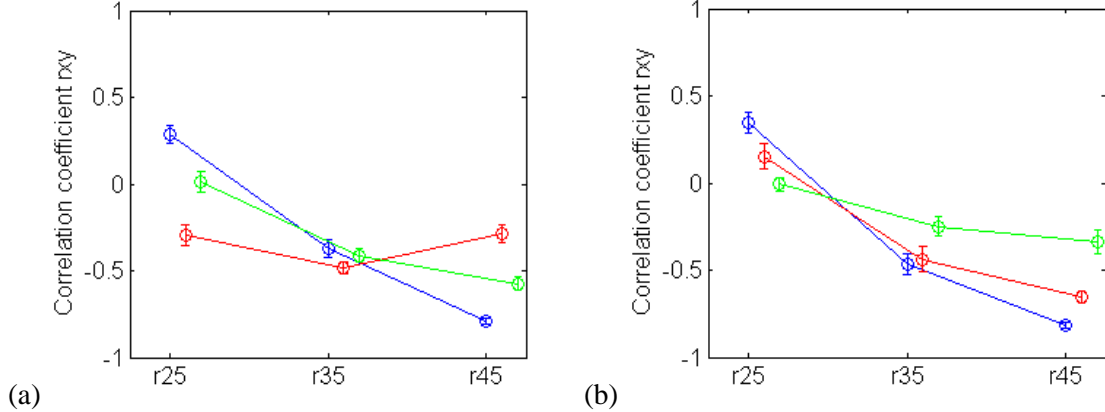


Figure 42: Correlation coefficients of random signals; (a) Linear system (Blue: R1_lin, Red: R1_lin_num1, Green: “R1_lin_num2”), (b) Nonlinear system (Blue: R1_nonlin, Red: R1_nonlin_num1, Green: R1_nonlin_num2).

5.3. Frequency domain analysis

Frequency domain analysis is a common technique used to understand dynamic systems. Therefore, features derived from this technique can be used to compare two dynamic systems’ responses. Most of frequency domain techniques are formulated under the assumptions of a linear system and that the systems are stationary. In addition, the response of nonlinear systems can also be investigated by comparing the frequency spectra of the response and by some other frequency domain techniques; such as Cepstrum or the Holder exponent.

5.3.1. Frequency Response Function and Coherence Function

The FRF is a transfer function expressed in the frequency-domain and normally used to describe the input-output characteristics of a structural system (Wirsching, 1995, Bendat 1980, and Oppenheim and Willsky, 1997). When the assumption of linearity and time invariance are not valid, the FRFs are also dependent upon the independent variables of time and the input to the system. In this way, a conditional FRF is measured as a function of other independent variables in

addition to frequency. When the input forces and the output (e.g., accelerations) are described in the frequency-domain by $F(\omega)$ and $X(\omega)$, respectively, the transfer function $H(\omega)$, which is the FRF, can be written as

$$H(\omega) = \frac{X(\omega)}{F(\omega)} . \quad (22)$$

Theoretically, these frequency domain functions are derived from the Fast Fourier transform (FFT) of time-domain data. The estimated FRF is a complex quantity that represents the amplitude and phase properties of this input-output relation. The plot of the norm of the calculated values is then useful to investigate the structural response in the frequency-domain. When the structure is subjected to a random input, the Hanning window is often applied to the time-domain data to reduce the effects of leakage on the FRF estimate. In addition, the effects of random noise on the FRF estimate can be reduced by averaging (often with overlap in the portions of the signal being used for the FRF calculations). In deriving the FRFs here, the FFT calculation is applied to each of the ten time-histories. By adopting the Hanning window with 0% overlap, a FRF based on ten averages can then be estimated.

The coherence function is a measure of the linear correlation between the output and input signals at each frequency and it can provide a quick visual inspection of the quality of the FRF estimate (Wirsching, 1995, Oppenheim and Willsky, 1997, and Bendat 1980). Additionally, it can be an indicator of noise in the measurements or nonlinear system response. Assuming the noise influencing the input and output measurements is uncorrelated, the definition of the coherence function is:

$$\gamma^2(\omega) = \frac{|S_{xf}(\omega)|^2}{S_{ff}(\omega)S_{xx}(\omega)} \quad (23)$$

where, $S_{ff}(\omega)$ is the power spectrum of the measured input; $S_{xx}(\omega)$ is the power spectrum of the measured output; and $S_{xf}(\omega)$ is the cross-power spectrum between the measured input and output. This quantity represents the fraction of the output power that can be linearly correlated with the input. It can be shown that the coherence takes on a value $0 \leq \gamma^2 \leq 1$ and the coherence for a single average will always be equal to one. If the coherence value is less than one (i.e., $\gamma^2 < 1$), it indicates the presence of noise and/or other factors affecting the linear input-output relationship such as nonlinear system response or additional unmeasured inputs to the system. For lightly damped systems, loss of coherence can occur at frequencies associated with the resonant peaks, where the response in the current time window results from input in the previous time window that has not damped out. If the value becomes zero, it then suggests that none of the output is linearly correlated with the input.

Figure 43 shows an FRF and a coherence function derived from the random input responses for the linear system. Recalling that the first mode is rigid-body mode below 20 Hz, it can be clearly observed that the second mode peak (around 30 Hz) from R1_lin_num2 that almost agrees exactly with that of the experimental data, whereas the peak value in the FRF from R1_lin_num1 is higher than the others. This indicates that the second mode damping ratio in Model #L2 is more appropriate to describe the actual behavior of the structure. Because a linear model was used in the numerical simulations, the loss of coherence observed at the frequencies associated with the resonant peaks are attributed to the issues with the lightly damped system response described above. The additional loss of coherence above 120 Hz associated with the R1_lin_num1 model is

assumed to result from the Matlab interpolation scheme that takes the output of the differential equation solver and produces a signal with data points that are discretized in time at the same sampling frequency as the measured data.

The FRF and the coherence function can be used as an indicator of the presence of nonlinearity in specific frequency bands or resonance regions. The estimated functions from the nonlinear system subjected to the random excitation are shown in Fig. 44. The amplitudes of three FRFs are similar; however, the third mode resonant frequencies from the two numerical data sets are slightly higher than that from the experimental data. In addition, there is a difference in the coherence functions around the third mode resonant frequency (around 55 Hz). Near this frequency the coherence from R1_nonlin_num2, which has the more pronounced nonlinear response characteristics because of the smaller gap at the bumper system, becomes lower than the other numerical data R1_nonlin_num1. This result indicates that the behavior of the bumper system influences the third mode response. In this case, the result in Fig. 44 shows that Model #N1 is a more appropriate model to describe the three-story structure when it responds in a nonlinear manner.

However, it must be recognized that the FRF and the coherence function are high-dimensional features, and some type of dimension reduction scheme is required if these functions are to be employed in model validation studies. In the previous discussion a qualitative dimension reduction scheme has been presented where the discussion focused on a comparison of these functions specifically at the resonant frequency peaks. Because the FRF and coherence functions include a high level of information about the condition of the structure, low-dimensional features based on these functions should be chosen depending on what information is needed for the model validation study. For instance, when the damping ratio is being investigated, the amplitude value of each peak should be extracted. Note that these two functions have sources of variability, and their calculations depend on various parameters (i.e., the frequency resolution, the number of FFT points, the windowing function(s), and the percentage of overlap). Therefore, it is important to use constant values for those parameters in the comparison. Also, noise that may be present in the measurement process typically cannot be duplicated in the numerical simulations, and the interpolation process used in conjunction with the numerical solution of the equations of motion does not exist in the measurement process. One has to be aware of such differences when comparing these functions for the purpose of model validation.

Another technique that may be employed to compare structural conditions (especially in the nonlinear system) is through the FRF and the coherence function acquired under different excitations. Theoretically, in the case of the linear system, these functions should show the same profile even if a different excitation level is applied to the structure. This result is related to the fact that these functions are both normalized by the input spectrum. For a linear system the relationship between input and output signals does not change even if the excitation level becomes larger or smaller. In addition, when the sensing locations of the input and output signals are switched in the linear system, the same FRFs and coherence functions should be obtained. The former property is termed linearity and the latter reciprocity. Figure 45 shows each of these properties by overlaying FRFs and coherence functions corresponding to the measured system response data. The linearity is shown by functions from two random excitations at different levels (i.e., 2.5 V RMS and 1.5 V RMS), and the reciprocity is from two transient excitations caused by impact hammer strikes, in which locations of the impact point and the sensing point were exchanged. The FRF and coherence functions from the two experimental data sets in each of the two figures show good agreements; therefore, it can be said that the test-bed structure without the bumper mechanism is exhibiting linearity and the reciprocity.

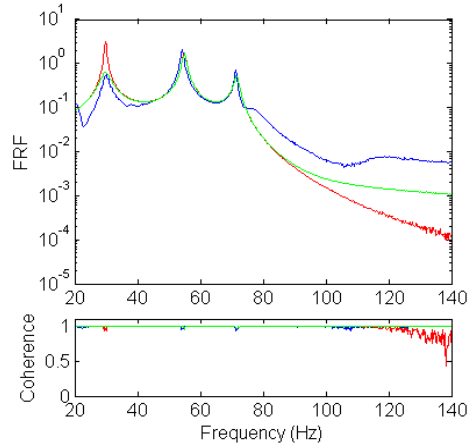


Figure 43: FRF and Coherence function from random data in linear system (Blue: R1_lin, Red: R1_lin_num1, Green: R1_lin_num2).

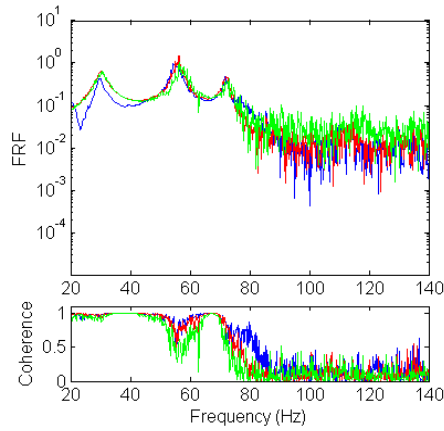


Figure 44: FRF and Coherence function from random data in nonlinear system (Blue: R1_nonlin, Red: R1_nonlin_num1, Green: R1_nonlin_num2).

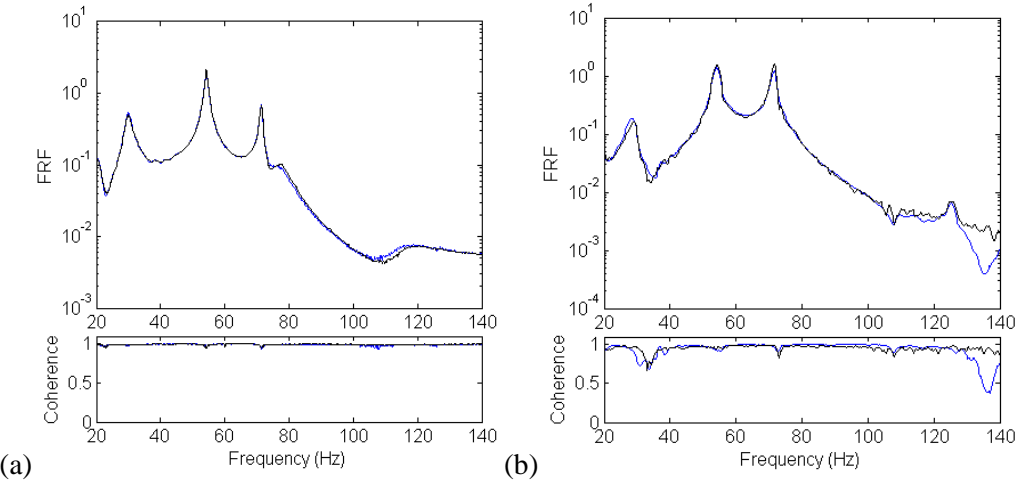


Figure 45: Overlay of FRFs and coherence functions from experimental data in linear system;
(a) Linearity from random signals (Blue: R1_lin (2.5 V RMS), Black: R2_lin (1.5 V RMS)),
(b) Reciprocity from impact hammer signals (Blue: I1_lin, Black: I2_lin).

In the nonlinear system, it is known that linearity and reciprocity are not necessarily satisfied, and the FRFs and coherence functions from different inputs may not overlay. By comparing the degree to which these functions correspond, the validity of nonlinear numerical modes may be investigated. Figure 46 illustrates the linearity check applied to the experimental and numerical data from the nonlinear system. Upon examination of the coherence functions, the agreement between the outputs with different excitation levels at the frequency range around 40 Hz in the figure of Model #N1 (Fig. 47(b)) are closer to those exhibited by the experimental data (Fig. 47(a)). This result was obtained because the outputs from Model #N2 were much more influenced by impact events, and the difference between coherence values associated with the 2.5 V RMS and 1.5 V RMS excitations became large as compared to the other two results. In the result of the reciprocity check shown in Fig. 47, there is a similar difference to that observed in the linearity check at the frequency range around 40 Hz in the coherence functions. The degree of consistency between two correlation functions in Model #N1 is similar to the result from the experimental data compared to that obtained from Model #N2. These results imply that the coherence function comparison can be used to investigate nonlinearity of structural systems. However, because the function itself is a high-dimensional feature, some metric to quantitatively compare the two functions from different excitations is required to adopt it for model validation applications.

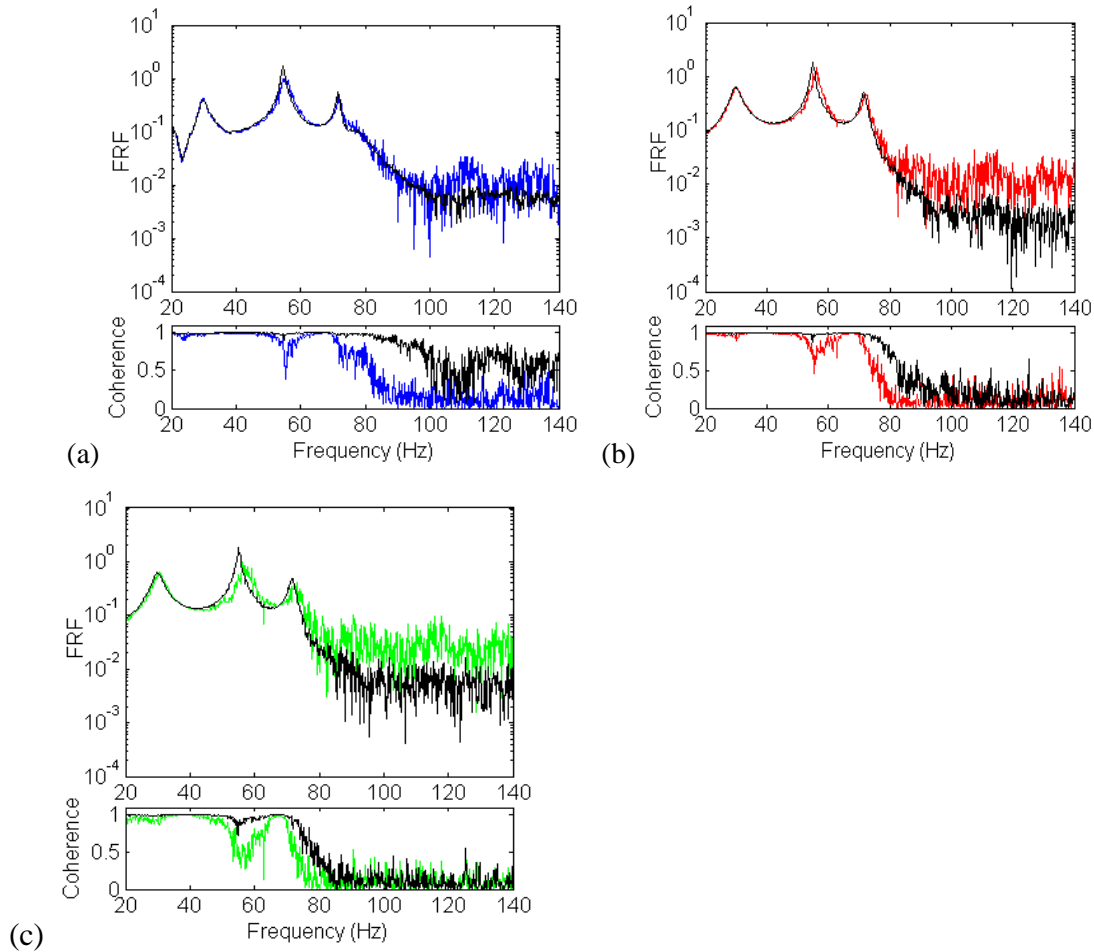


Figure 46: Linearity checks in the nonlinear system; (a) Experimental data (Blue: R1_nonlin, Black: R2_nonlin), (b) Numerical data from model N1 (Red: R1_nonlin_num1,

Black: R2_nonlin_num1), (c) Numerical data from model N2 (Red: R1_nonlin_num2, Black: R2_nonlin_num2).

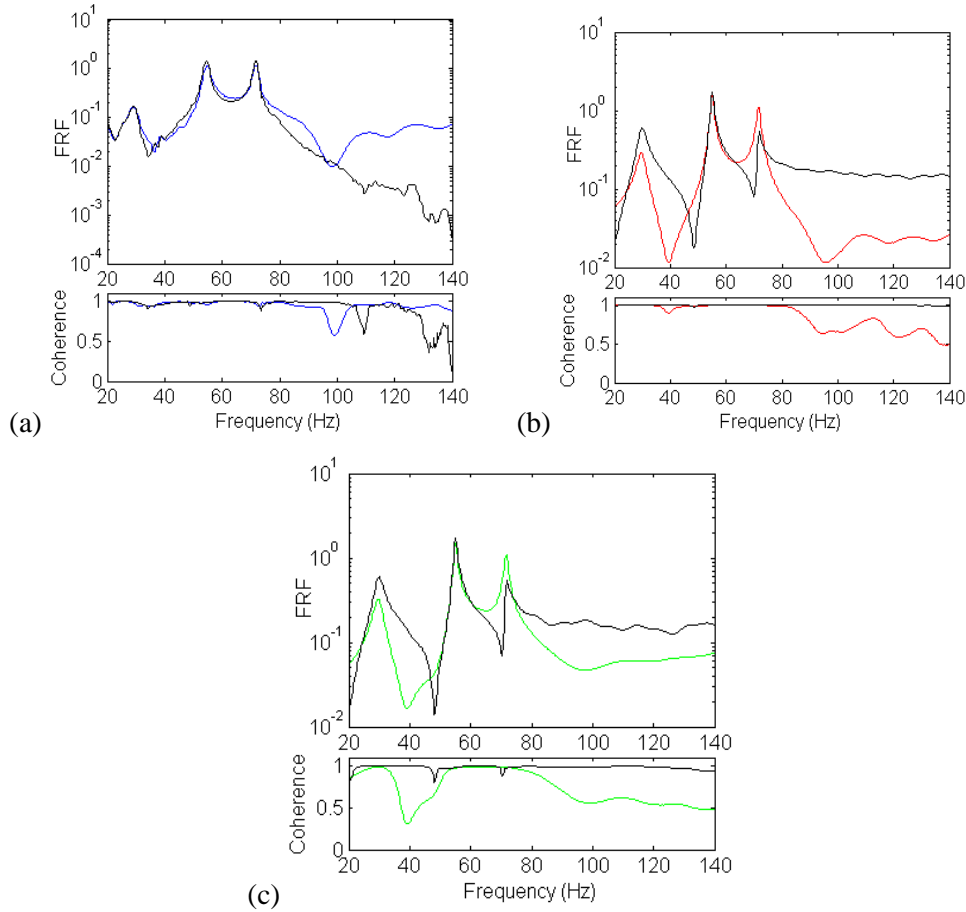


Figure 47: Reciprocity checks in the nonlinear system; (a) Experimental data (Blue: I1_nonlin, Black: I2_nonlin), (b) Numerical data from model N1 (Red: I1_nonlin_num1, Black: I2_nonlin_num1), (c) Numerical data from model N2 (Red: I1_nonlin_num2, Black: I2_nonlin_num2).

5.3.2. Power Spectral Density

The PSD indicates the energy of a signal as a function of frequency and is derived from the FFT of each time-history (Wirsching et al., 1995 and Bendat 1980). The PSD is defined as the FFT of the signal multiplied by its conjugate, and normalized by the frequency resolution of the spectrum. It is possible to compare the power components at each frequency by overlapping the estimated PSD, as was demonstrated using FRFs in the previous section. Moreover, the PSD is also useful to identify strong frequency components contained in the time-history data.

Figure 48 shows the estimated PSDs of data associated with harmonic excitations applied to both the linear and nonlinear systems. The PSDs in this study were derived by using Welch's method (Matlab function "pwelch"). With respect to the numerical and experimental data being considered herein, the length of Hanning window was the same as that of each time-history (i.e., 16,384 points), and ten averages were performed with 0% overlap. The frequency of the input signal is 71 Hz for the linear system (Fig. 48(a)) and 54Hz for the nonlinear system (Fig. 48(b)).

As expected, a spike of the PSD amplitude emerges at the frequency of the input signal in each figure. In addition, there are several smaller amplitude spikes shown in the figure of the nonlinear system response PSD; these spikes indicate that some harmonic distortions emerge in the output signal as a result of the impact events. It is thus expected that the number and amplitude of these spikes reflects the characteristics of the nonlinearity in the structural system. Figure 49 presents the comparison of PSDs obtained from the experimental data and the two numerical runs in the nonlinear system. In these plots, the y-axis has been rescaled to better visualize the smaller amplitude spikes in the spectra. It can be seen that the PSD of the harmonic response from Model #N1 (Fig. 49(b)) shows the four spikes at the same frequencies as in the PSD of the experimental data (Fig. 49(a)) with similar amplitudes. On the other hand, the result from Model #N2 shown in Fig. 49(c) indicates that the harmonic distortions increase considerably, due to the increase of impact events.

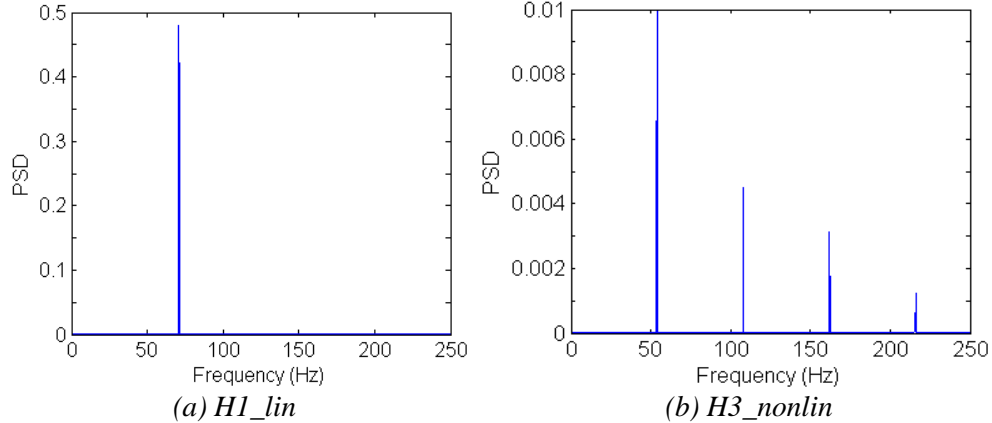
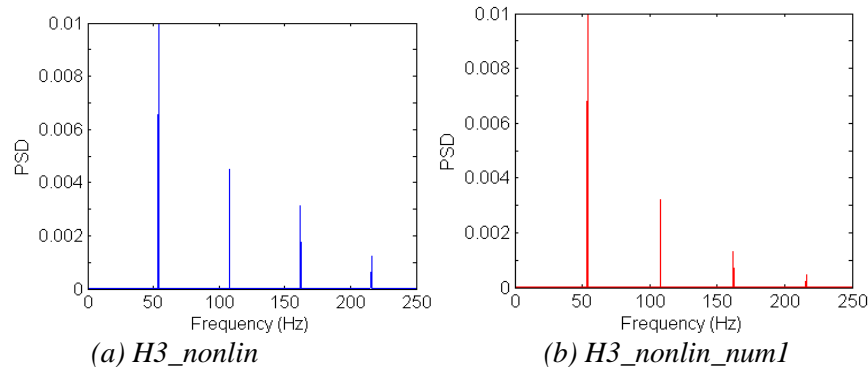


Figure 48: PSDs of the experimental data when harmonic excitations are applied to the linear and nonlinear systems.



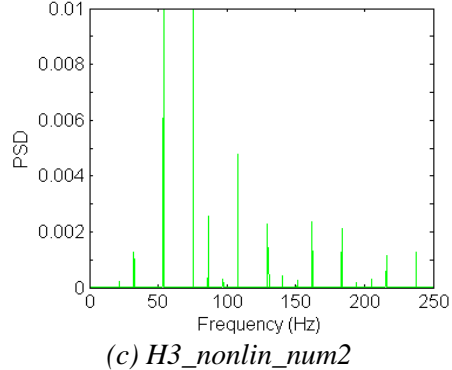


Figure 49: PSDs from the experimental and numerical data when harmonic excitations are applied to the nonlinear system

It is demonstrated that the analysis of PSDs is useful for investigating nonlinearity. For data from harmonic excitations, the number of spikes and their amplitudes in the spectrum can be used as low-dimensional features. It is worth repeating here that the signal processing parameters used to generate the PSDs from both the experimental and numerical data should be constant for comparison purposes, as noted for the FRFs and coherence functions in the previous section.

5.3.3. Response Spectra

The response spectra associated with the responses of a multi-degree-of-freedom (MDOF) system are calculated by treating each response as the input to a series of single degree-of-freedom (SDOF) systems with different natural frequencies. Each SDOF system consists of mass m , damper c , and spring k . From the equation of motion for an SDOF system, the response of each oscillator is calculated and a one-dimensional output quantity is derived (e.g., the peak or RMS value of acceleration). This procedure is repeated for SDOF systems with different natural frequencies while keeping the damping ratio c constant (2% damping ratio was used in this study). The response spectrum is a plot of the output quantity as a function of the system's natural frequency. A response spectrum quantifies the amplification in response for a given dynamic input as a function of the system's natural frequency. However, phase information between the input and response is lost in this process. Because assumptions are very minimal (i.e., only the damping ratio of a SDOF system) the response spectrum can be defined and computed for response measured on both the linear and nonlinear systems, excited by stationary and non-stationary signals (Alexander, 2009 and Clough and Penzien, 1993).

Figure 50 shows the derived response spectra wherein random excitations were applied to the linear and nonlinear systems. The spectra from R1_lin_num2 and R1_nonlin_num1 are closer to those derived from the experimental data for the linear system and nonlinear system, respectively. The significant point here is that the agreement between the numerical models and the experimental data can be investigated not only with respect to the resonant frequencies, but also with respect to the entire frequency range of the spectrum. Considering the nonlinear system, the FRF profiles above 80 Hz are too noisy (see Fig. 44) making comparisons difficult, but the agreement of the response spectra can be more easily verified in the high frequency range in Fig. 50 (b). In the context of model validation in which the response spectra are the features of interest, it is necessary to establish some low-dimension or scalar quantity that indicates the difference between two spectra's profiles over the frequency range of interest.

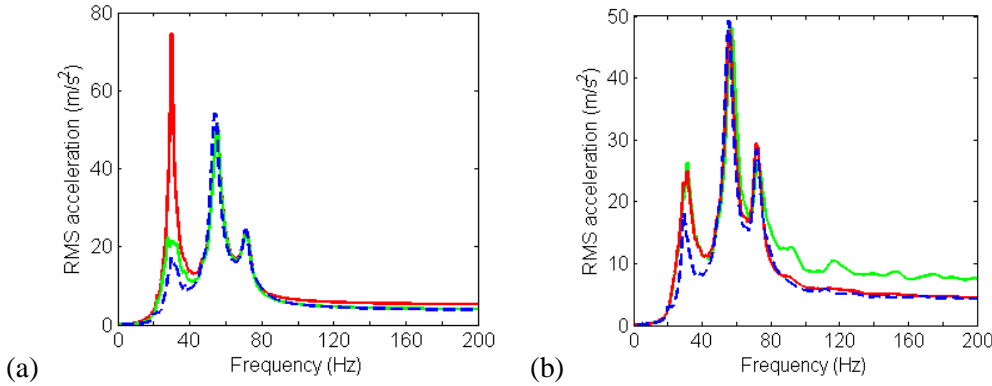


Figure 50: Response spectra corresponding to a random excitation; (a) Linear system (Blue: R1_lin, Red: R1_lin_num1, Green: R1_lin_num2), (b) Nonlinear system (Blue: R1_nonlin, Red: R1_nonlin_num1, Green: R1_nonlin_num2).

5.3.4. Cepstrum

The cepstrum analysis is a signal processing technique that is used primarily in acoustic applications. It provides information about the presence of harmonic components in a spectrum and was originally invented for characterizing seismic echoes in a signal (Randall, 2011). The complex cepstrum is defined as the “Fourier transform of the logarithm of the Fourier transform of a signal,” and is given as follows

$$\hat{x} = \frac{1}{2\pi} \int_{-\pi}^{\pi} \log[X(\omega)] e^{j\omega n} d\omega \quad (24)$$

When an echo emerges in the time-domain signal, the amplitude of the cepstrum becomes large at that time. Notice that the calculated cepstrum is in the time-domain, and this time-scale axis is called the “quefrency.” Additionally, when the inverse Fourier transform is applied to Eq. (24), the logarithm of the Fourier transform can then be reconstructed. By filtering a certain range of quefrency in this procedure, which is like the low-pass filter, the envelope behavior of the Fourier spectrum can then be analyzed; this is named “liftering.”

Figure 51 shows the cepstrums, which are the amplitude plots of Eq. (24), derived from the experimental data and the two numerical outputs arising from the harmonic excitations applied to the nonlinear system. A significant difference is observed: the cepstrum values around quefrency = 550 with the values in this portion of the plot becoming large only for the result from

H1_nonlin_num2. The “liftering” was thus applied to each cepstrum by using the “quefrency” range of 0 to 600, producing the envelope behaviors shown in Fig. 52. It can be seen that the spiky profile at the peak frequencies can be compared with these envelope behaviors. The difference of the cepstrum around quefrency = 550 highlights the differences in the spectrum profiles. The result of “H1_nonlin_num1” is seen to be much closer to that of the experimental data. Although a metric is required to quantitatively assess the difference of the cepstrum (again because it is a high-dimensional feature), it is expected that this feature can be used to compare the predicted and measured responses from nonlinear dynamic systems.

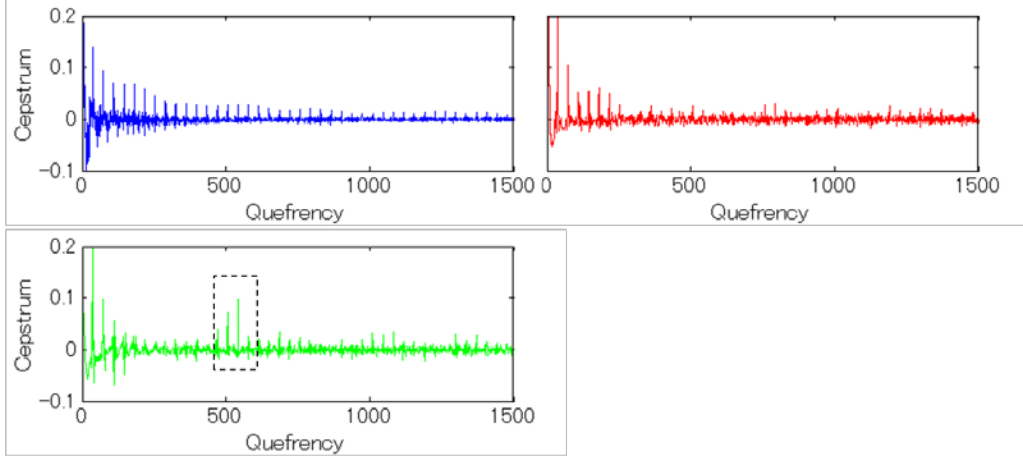


Figure 51: Cepstrum of harmonic signals in the nonlinear system (Blue: H1_nonlin, Red: H1_nonlin_num1, Green: H1_nonlin_num2).

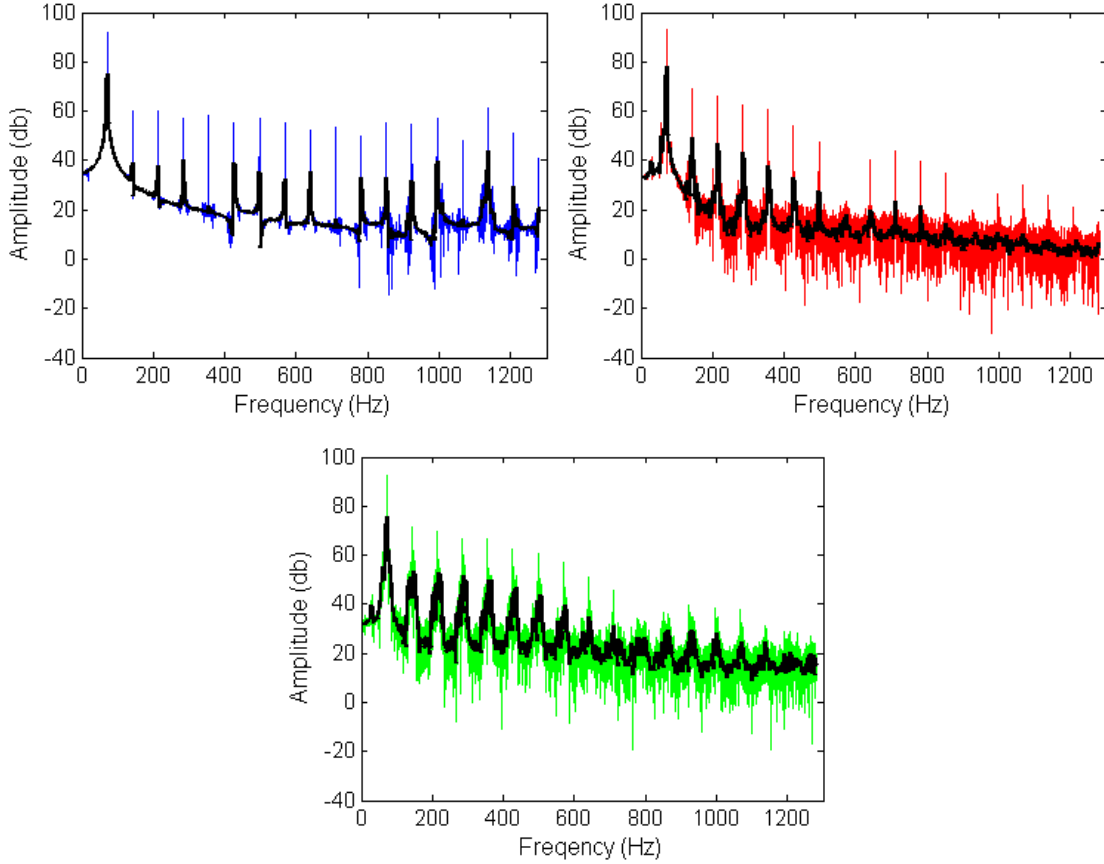


Figure 52: Overlays of the logarithm of the Fourier spectra and the “lifter” spectra (Blue: H1_nonlin, Red: H1_nonlin_num1, Green: H1_nonlin_num2, Black: the “lifter” spectrum for each output).

5.3.5. Holder Exponent

The Holder exponent is a technique that provides information about the regularity of the signal. Because singularity points have no continuous derivatives, they can be identified when the Holder exponent suddenly drops to a value of zero or below. In the SHM field, this feature can be used to identify a damage state that introduces discontinuities into the measured dynamic response (Robertson et al., 2003). For instance, it is possible to identify singularities associated with cracks that open and close during dynamic loading. Also, in the model validation, this feature is expected to be used for comparing numerical and experimental data for modelling nonlinearities, such as those introduced by impact events in this study.

The brief description of the procedure for deriving the Holder exponent is as follows. First, the wavelet transform of the target signal $x(t)$ is calculated, and the absolute value of the resulting coefficients, which are the wavelet transform moduli, are obtained as

$$|Wx(u, s)| = \left| \int_{-\infty}^{+\infty} x(t) \frac{1}{\sqrt{s}} \psi^* \left(\frac{t-u}{s} \right) dt \right|, \quad (25)$$

where ψ is the wavelet function, $*$ indicates the complex conjugate, u is a translation factor, and s is a scaling factor. One may then construct a frequency-domain spectrum at the first time point of

the modulus matrix and plot the absolute value of the coefficients versus the scaling factor s on a log-log scale. A linear function can be fit to this plot, and the slope m of the estimated function is the Holder exponent as shown in Eq. (26).

$$m = \frac{\log|Wx(u, s)|}{\log(s)} . \quad (26)$$

The parameter m is related to the regularity of the signal. To find the Holder exponent at all time points, repeat this process at each time point (columns of the wavelet modulus matrix). The singularity/discontinuous points in the signal can then be detected by identifying time points where the Holder exponent dips suddenly.

The major advantage of using the Holder exponent is that this feature has the same time-resolution as that of the response signal. Figure 53 presents the plots of Holder exponent derived from the experimental data and the two numerical runs, in which the nonlinear system was subjected to the random excitations. It is seen that the number of "drop-off," or singularity points indicated by black circles increases in the result of R1_nonlin_num2, in particular, where three times the number of points are obtained compared to the experimental data. It can thus be said that the Model #N1 is more representative of the actual system.

In Fig. 53 the singularity points from the Holder exponent are indicated by the black circles. Also, for the respective time-histories from the numerical calculations the moments at which the bumper contacts the suspended column are indicated by the red and green dots. The black circles correspond to the times when the impact events occur. The results indicate that the impacts in each time-history are mostly identified. Moreover, the degree of reduction of the Holder exponent value also reflects the relative amplitudes of the time-history at the singularity points. It can be concluded from this brief discussion that the Holder exponent can be used as the feature to investigate the nonlinear response characteristics of a structural system based on the total number of "drop-off" points, the time of each drop-off point, and their amplitudes.

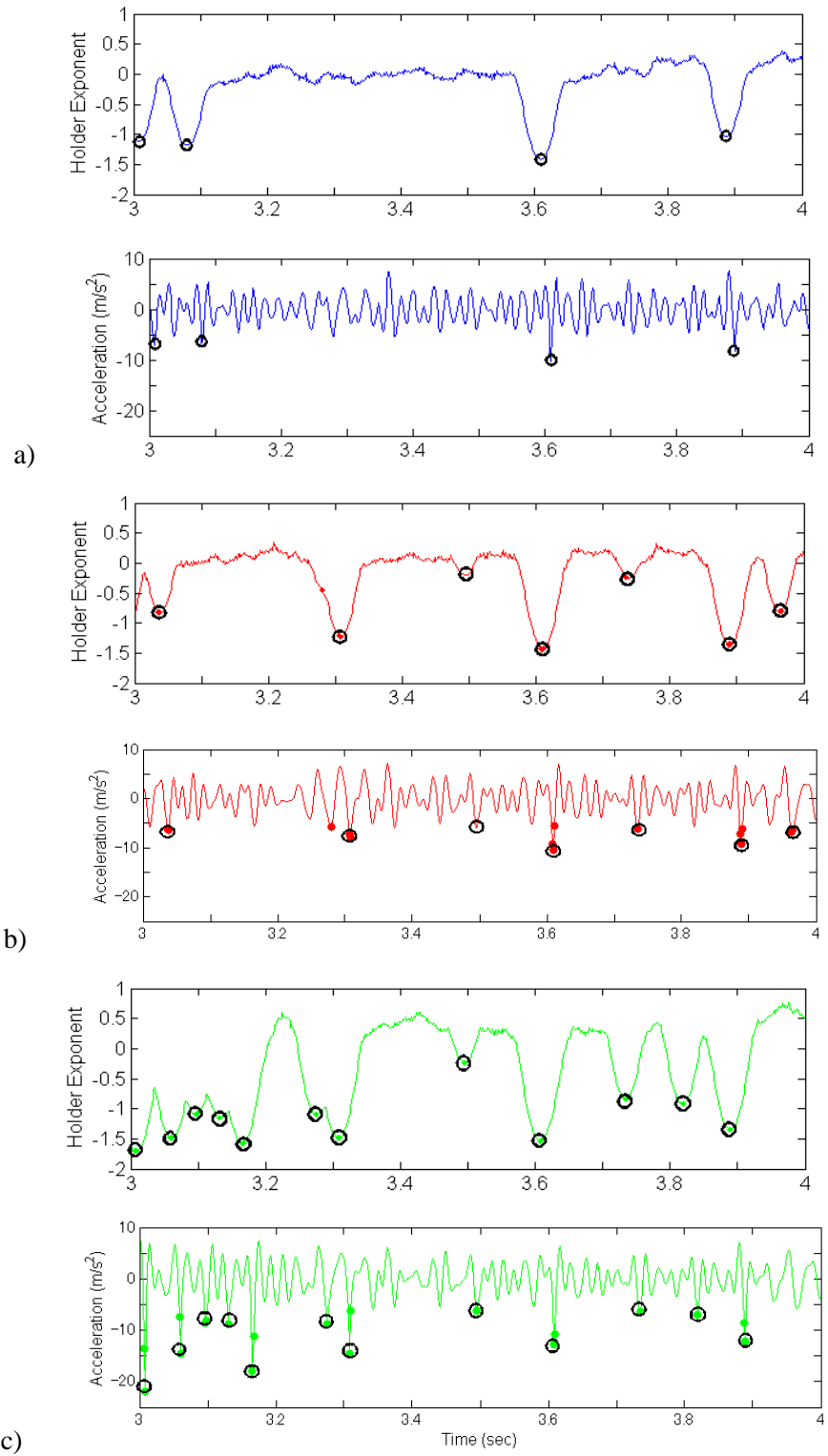


Figure 53: Holder exponent derived from the responses of the nonlinear system, and the time-histories indicating extracted singularity points; a) R1_nonlin, b) R1_nonlin_num1, c) R1_nonlin_num2, Black circles are the drop-off points in the Holder exponent, and the dots in the numerical runs indicate the impact events.

5.4. Time Series Analysis

The dynamic response from a structural system can be regarded as a time series. The time series analysis is a method to understand the statistical characteristics of these signals. In this section parameters of the time series model (e.g., autoregressive moving average [ARMA]) models (Box and Jenkins, 1976) will be used as features for model validation.

5.4.1. Autoregressive Model

The autoregressive model (AR) model of p^{th} order, AR(p), is defined as

$$\hat{x}_i = \sum_{j=1}^p \alpha_j x_{i-j} + \varepsilon_i , \quad (27)$$

where x_i is the measured signal at a discrete time index, i , and ε_i is a white noise process at the i^{th} signal value. The unknown AR parameters α_j can be estimated by using either least squares or the Yule-Walker equations. In this study, the latter method was used. The function in Eq. (27) can be understood as a transfer function to predict the i^{th} signal from previous discrete signal values. Therefore, the AR parameters, α_i , can be used as features to compare the response predicted by the numerical model and the measured system response.

To find the appropriate model order, several techniques can be used, such as the Akaike's information criterion (AIC), the partial autocorrelation function (PAF), root mean squared error (RMSE), and singular value decomposition (SVD). For the AR model estimation conducted herein, the AIC and the PAF are being considered (Figueiredo, Figueiras, Park, Farrar and Worden, 2011 and Figueiredo, Park, Figueiras, Farrar and Worden, 2009).

The AIC has been used to assess the performance of linear models. In a simple way, this technique returns a value that is the sum of two terms as follows:

$$AIC = -2L_m + 2m , \quad (28)$$

where L_m is the maximized log-likelihood of the residual error, and m is the number of adjustable parameters in the model. It assumes a tradeoff between the fit of the model and the model's complexity. The first term is related to how well the model fits the data; the second term is a penalty factor related to the complexity of the model, which increases as the number of model parameters grows (Box et al., 1994; Bishop, 1995; Everitt, 2002).

The coefficients from the PAF are estimated by fitting AR models of successively increasing order, p , to the measured data, then plotting the last estimated coefficient, α_{pp} , as a function of the model order. Thus, the AR model of Eq. (27) can be rewritten as follows:

$$x_i = \sum_{j=1}^p \alpha_{pj} x(i-j) + e_i . \quad (29)$$

For an AR model of a noise-free, order p process, the PAF α_{kk} will be nonzero for $k \leq p$ and zero for $k > p$. For actual structures with measurement noise, the PAF of AR(p) will not be zero after lags greater than p . It is thus necessary to define a confidence interval, in which the derived a_{kk} is considered to be essentially zero (Box and Jenkins, 1976). An approach based on the standard deviation of the error of the PAF, σ_α , is defined as

$$\sigma_\alpha[\alpha_{kk}] = \frac{1}{\sqrt{n}} \quad k \geq p+1 \quad , \quad (30)$$

where the estimated partial autocorrelation coefficients of order $p+1$ and higher are approximately independently distributed, and n is the number of observations used in fitting the AR model. Assigning a confidence interval for statistical significance is helpful for this purpose. For example, the assumption of an approximate 95% confidence interval for the partial autocorrelation coefficients places limits on the error at $\pm 2\sigma_\alpha$.

Figures 54 and 55 show the AIC and PAF plots, respectively, for the AR model estimation in the case of random excitation applied to the linear system; Channel #5 signals of the first histories of R1_lin, R1_lin_num1, and R1_lin_num2 are considered. From the result of the AIC plot in Fig. 54, all distributions from the experimental data and the two numerical runs asymptotically approach their minimum values somewhere in the range of $p = 30-50$. On the other hand, the results of the PAF in Fig. 55 indicate that the appropriate AR order for the experimental data R1_lin is $p = 45$, that for R1_lin_num1 is $p = 40$, and that for R1_lin_num2 is $p = 50$, respectively. These values are evaluated by finding a coefficient which is within the 95% confidence interval represented by the horizontal lines in each figure. For comparing estimated AR models from three time-histories, the same order should be used; therefore, AR (50) was adopted for all AR model estimates presented herein.

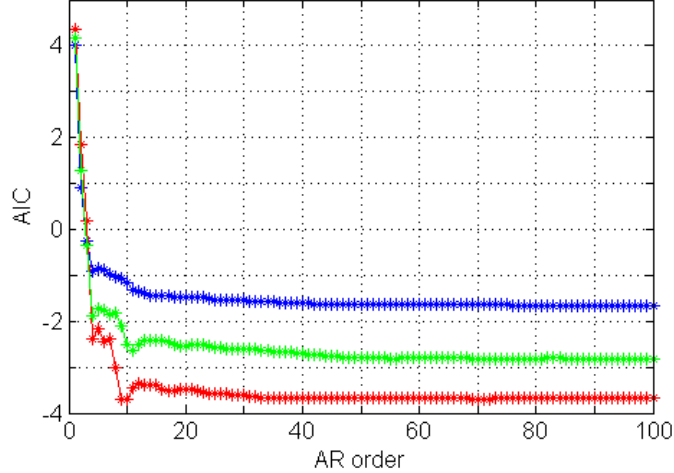


Figure 54: Calculated AIC for AR model of the random signal (Blue: R1_lin, Red: R1_lin_num1, Green: R1_lin_num2).

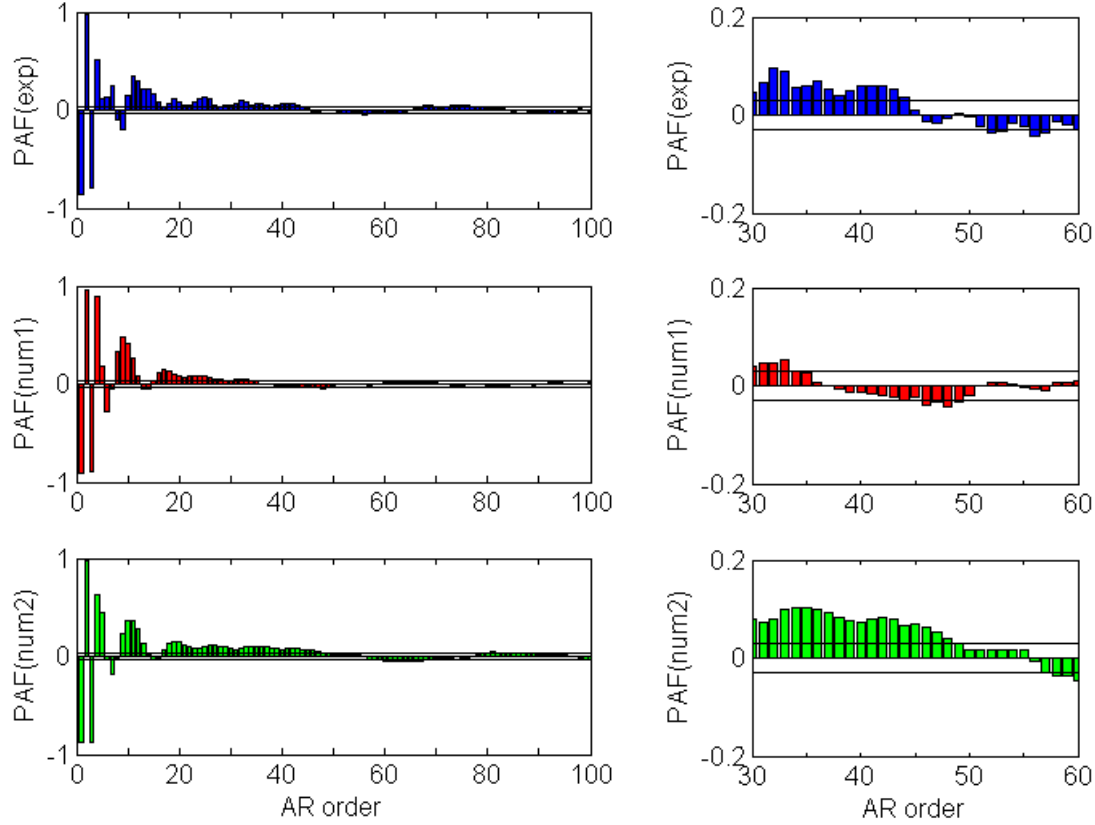


Figure 55: Estimated PAF for AR models from the random signal (Blue: R1_lin, Red: R1_lin_num1, Green: R1_lin_num2).

Figure 56 illustrates the estimated AR (50) model parameters from the experimental data and the two numerical runs. The estimated models show good agreement with the respective time-histories as shown in Fig. 57. The estimated error at time i can be calculated as

$$e_i = \hat{\varepsilon}_i = x_i - \hat{x}_i , \quad (31)$$

where \hat{x}_i is the predicted i th signal value. Notice that, for a AR (p) model, the residual errors can only be computed for $i > p$ time points. If the order of the AR model is appropriately selected, and if the time-series can be accurately described by an AR model, the residual errors should be nearly uncorrelated with no systematic bias (i.e., white noise). Figures 58 and 59 are the plots of the estimated residual errors and their NPPs for each model. All of them indicate that the errors can be approximated as a Gaussian white noise process. The standard deviations of the noise signals from the two numerical models are, in fact, quite smaller than that from the experimental data. This result is attributed to the inherent lack of measurement noise in the numerical models. Upon examination of the PSDs of the residual errors in Fig. 60, no significant correlation is observed because no specific peak is identified in these plots. It can thus be inferred that the order of the three AR models has been appropriately chosen. However, the plots of the estimated AR parameters presented in Fig. 56 show different tendencies between the experimental data and the two numerical runs, and it is difficult to evaluate the differences between Model #L1 and #L2. It

can be inferred from this finding that the sensitivity to damping ratios and other properties of the numerical models cannot be easily diagnosed from the AR parameters alone.

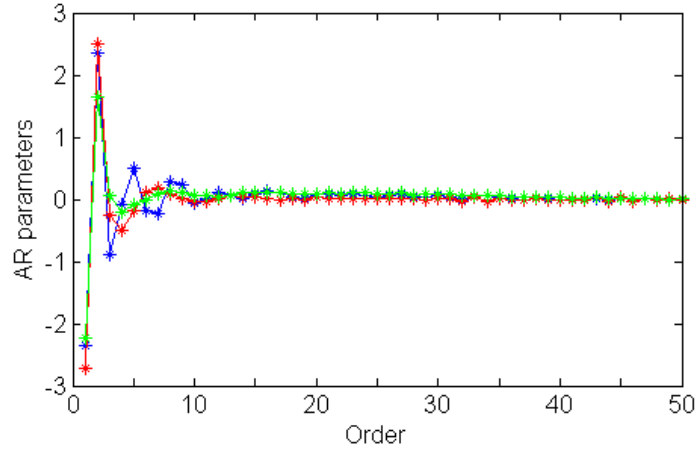


Figure 56: Estimated AR parameters for the linear system (Blue: R1_lin, Red: R1_lin_num1, Green: R1_lin_num2).

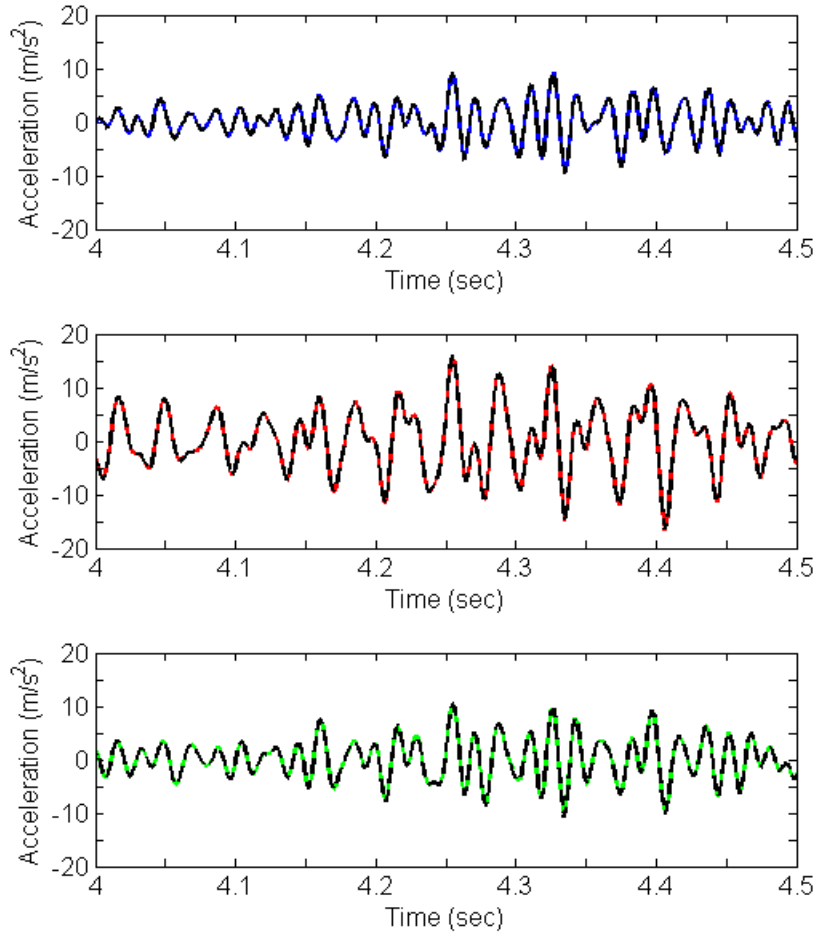


Figure 57: Overlays of original data and time-series from AR model of the linear system (Blue: R1_lin, Red: R1_lin_num1, Green: R1_lin_num2).

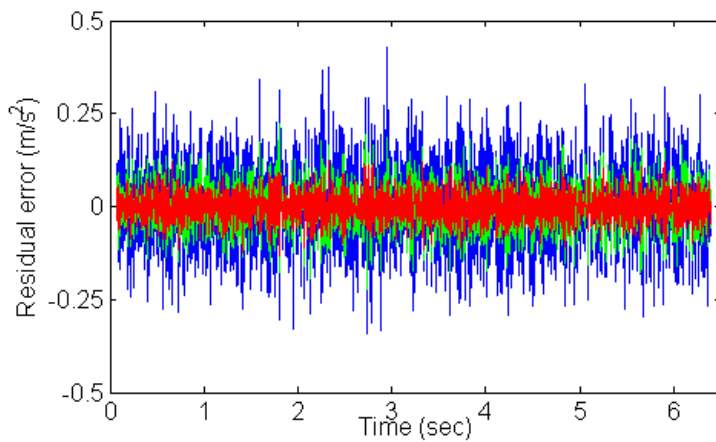


Figure 58: Overlay of estimated residual error of AR model from the linear system (Blue: R1_lin, Red: R1_lin_num1, Green: R1_lin_num2).

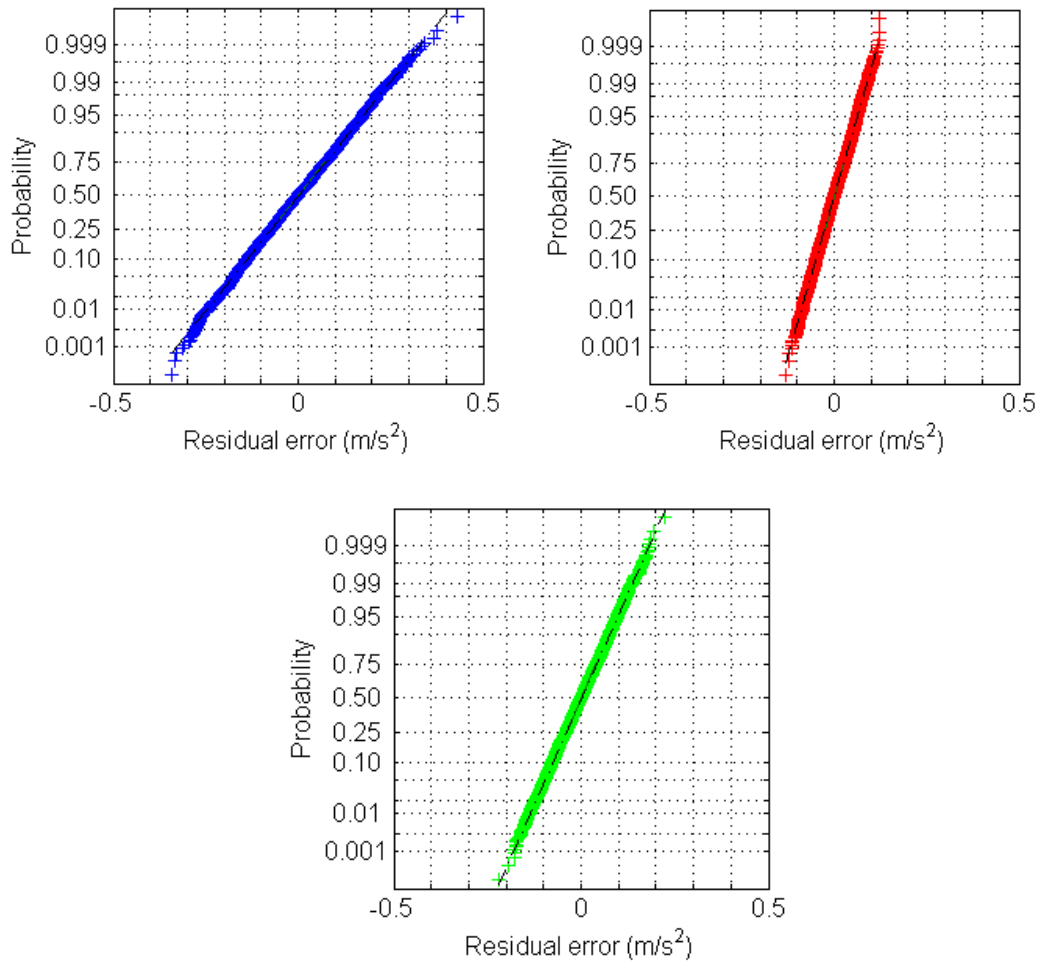


Figure 59: NPPs of estimated residual errors from AR model of the linear system (Blue: R1_lin, Red: R1_lin_num1 , Green: R1_lin_num2).

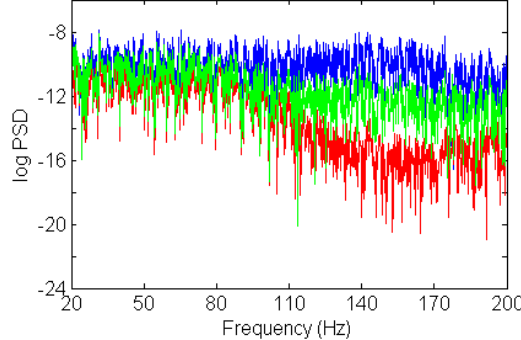


Figure 60: PSDs of estimated residual errors from AR model of the linear system (Blue: R1_lin, Red: R1_lin_num1, Green: R1_lin_num2).

This result is, however, not the case when considering nonlinearity within the structural system. Considering that AR models are linear models, as the nonlinearity increases, the AR model should not predict the data well, and correspondingly, the residual error may not show a normal distribution. In the SHM field, it has been shown that crack damage could be well detected by this mechanism (Sohn et. al., 2001, Farrar et. al., 2007, and Figueiredo et. al., 2009). This result is also expected to be useful in model validation studies applied to nonlinear systems.

Figure 61 shows the estimated AR (40) model parameters from the experimental data and the two numerical runs when the random excitation was applied to the nonlinear system. It can then be seen that the result from R1_nonlin_num1 agrees with that of the experimental data. The overlays of the estimated model and the original time-history shown in Fig. 62 reveal that the agreement at the singularity points, which are the impact events, is influenced by the modeling of nonlinearity; i.e., parameters Gap and Δ . Therefore, the estimated residual error can also be employed to reflect nonlinearity in a structural system. Figure 63 plots the residual errors from three structural systems, where the black dots in the results from the two numerical runs indicate the times when the bumper contacts the suspended column. The outliers of the residual error distribution agree well with the impact events. The profile of the residual error plots and its amplitude from R1_nonlin_num1 (Model #N1) are seen to be much closer to those from the experimental data, and thus can be used as features that have the same time-resolution as the measured or calculated acceleration responses. The comparison of NPPs of the estimated residual errors also indicates that Model #N1 is more appropriate to describe the actual structure as shown in Fig. 64. It can be concluded that estimated AR parameters and residual errors will also be useful for the model validation of nonlinear structural systems.

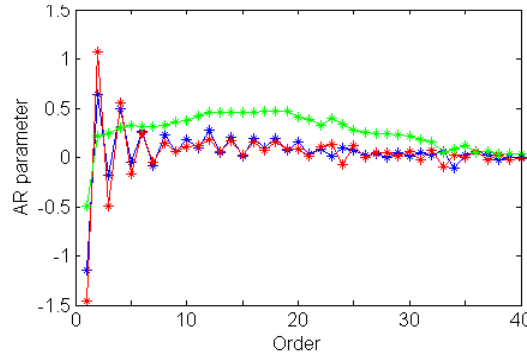


Figure 61: Estimated AR parameters for the nonlinear system (Blue: “R1_nonlin”, Red: R1_nonlin_num1 Green: R1_nonlin_num2

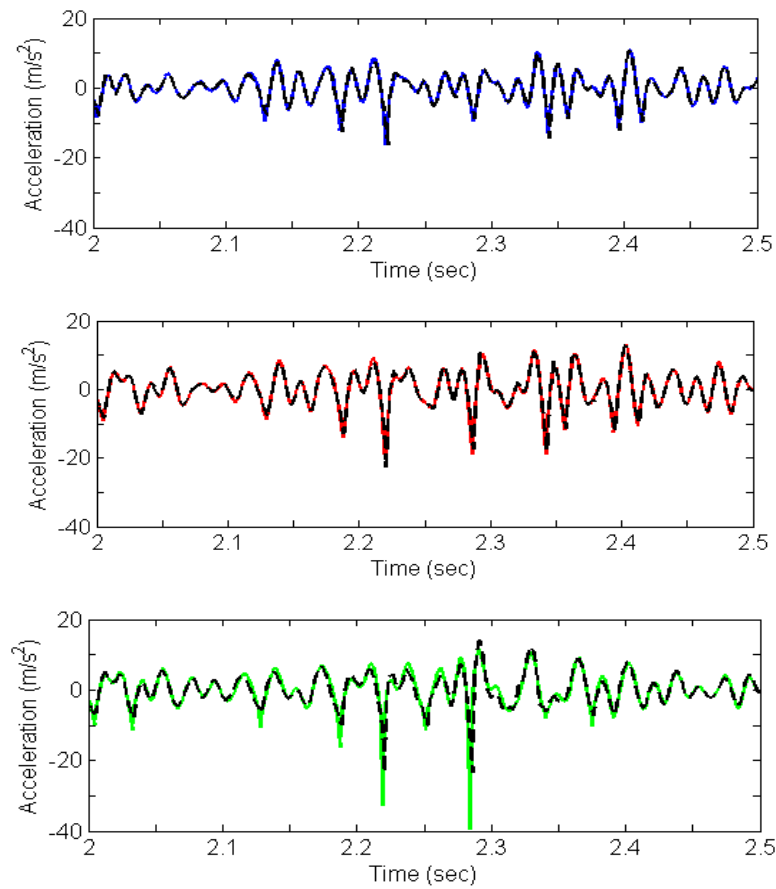


Figure 62: Overlays of original data and time-history from AR model in the nonlinear system (Blue: R1_nonlin”, Red: R1_nonlin_num1, Green: R1_nonlin_num2).

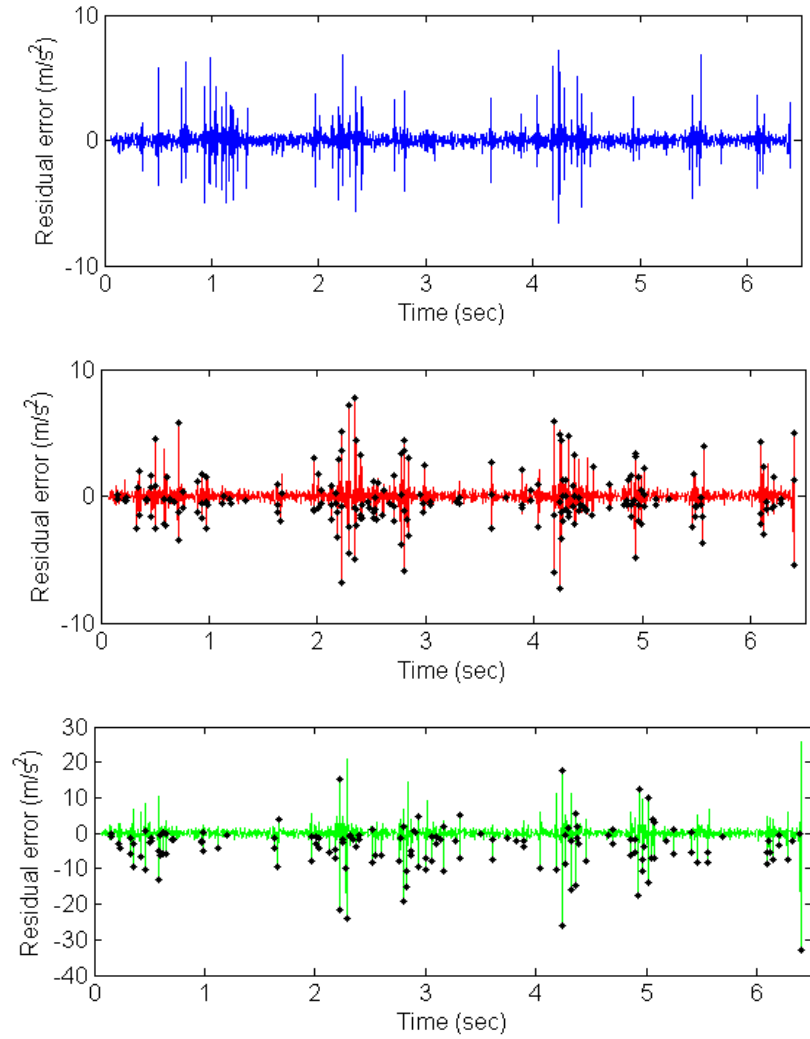


Figure 63: Estimated residual errors of AR model in the nonlinear system (Blue: $R1_{\text{nonlin}}$, Red: $R1_{\text{nonlin_num1}}$, Green: $R1_{\text{nonlin_num2}}$, Black dots: the time of impact event).

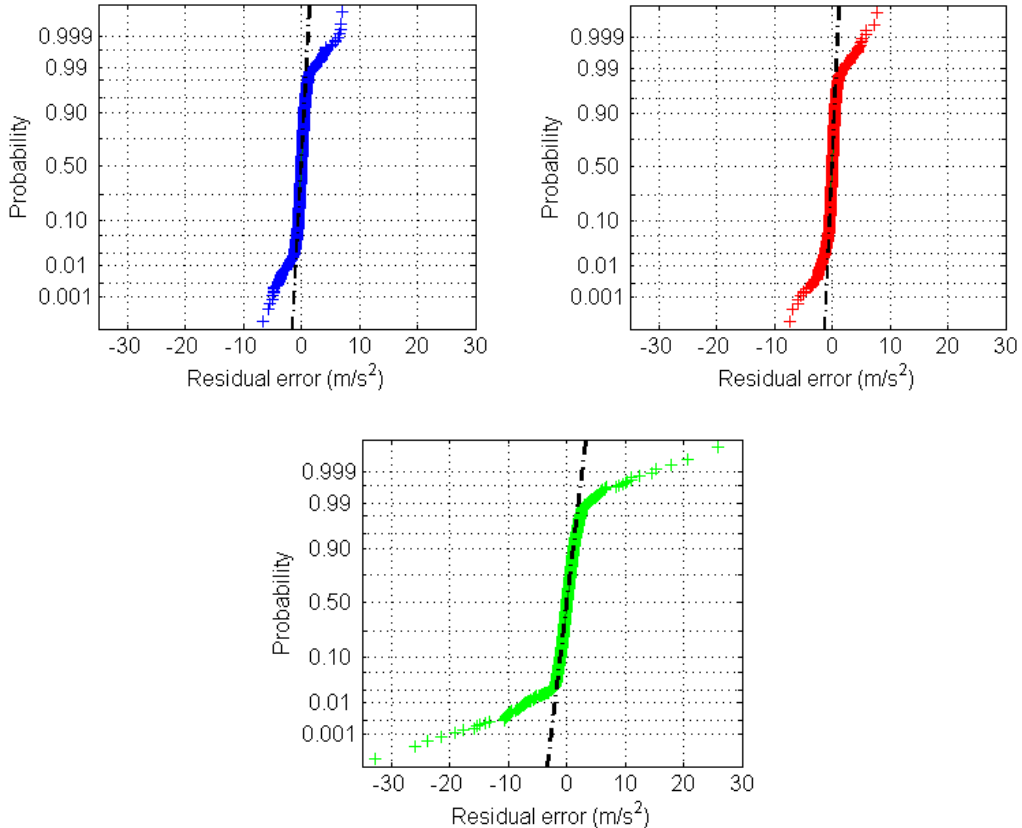


Figure 64: NPPs of estimated residual errors of AR model in the nonlinear system (Blue: R1_nonlin, Red: R1_nonlin_num1, Green: R1_nonlin_num2).

5.4.2. Autoregressive with Exogeneous Input Model

The AutoRegressive with eXogeneous input (ARX) model is formed to estimate the relationship between inputs and outputs of a system. The definition can be described using both the output signal x and the input force f as show in

$$x_i = \sum_{j=1}^a \alpha_j x_{i-j} + \sum_{k=0}^b \beta_k f_{i-k} + \varepsilon_i , \quad (32)$$

where α_j and β_k are the AR parameters and X parameters, respectively, and a and b are their respective orders. This model is appropriate for predicting the dynamic response of a structural system because a discretization of the equation of motion shows that the response is a function of the previous output signals and the input signals. Suppose that one is interested in the previously defined SDOF linear system,

$$m\ddot{x} + c\dot{x} + kx = f(t) . \quad (33)$$

This equation of motion can be converted by a process of finite-difference approximation to the discrete-time form,

$$x_i = \alpha_1 x_{i-1} + \alpha_2 x_{i-2} + \beta_1 f_{i-1} . \quad (34)$$

The coefficients α_1 , α_2 , and β_1 are functions of the original constants m , c , k , and the sampling interval $\Delta t = t_i - t_{i-1}$, where the t_i are the sampling instants. In a more general form, Eq. (34) may be described as

$$x_i = F(x_{i-1}, x_{i-2}, f_{i-1}) \quad (35)$$

When an ARX model is adopted, only the two states, x and f , are required in order to estimate all of the model parameters α_1 , α_2 , and β_1 in Eq. (34). A general MDOF linear system has a discrete time representation:

$$x_i = F(x_{i-1}, \dots, x_{i-a}, f_i, \dots, f_{i-b}) \quad (36)$$

Therefore, the AR parameters, α_j , and X parameters, β_k , are expected to be features that can be used to compare numerical model and the actual structural system. All α_j and β_k can be estimated using the least-squares method.

The AR (25) and X (25) model parameters estimated when the random excitation is applied to the linear system are shown in Fig. 65. In both figures, the parameter distributions from two numerical runs are quite similar, and differ significantly from those of the experimental data. This tendency is similar to the result from the AR model estimation for the linear model as discussed in the previous section. Although the estimated time-history agrees with the original data in each model shown in Fig. 66, Fig. 67 indicates that the estimated residual errors in the two numerical runs are distributed in a smaller range as compared with the result from the experimental data. This large difference between the estimated model of the actual structure and those for two numerical models is considered to be related to the difference in the kind of error in the output data. The experimental data includes random measurement errors (near white noise) due to the sensor system noise and the other random effects. Meanwhile, the error in numerical outputs is related to systematic errors resulting from the mathematical approximation in the modeling process and the numerical calculation algorithm. The ARX model estimation is considered to be more sensitive to such error sources. The significant differences in the AR and X parameters and the residual error are seen when the experimental data is compared to the data from the two numerical runs. Therefore, it is difficult to assess the validity of even the linear numerical model using these features.

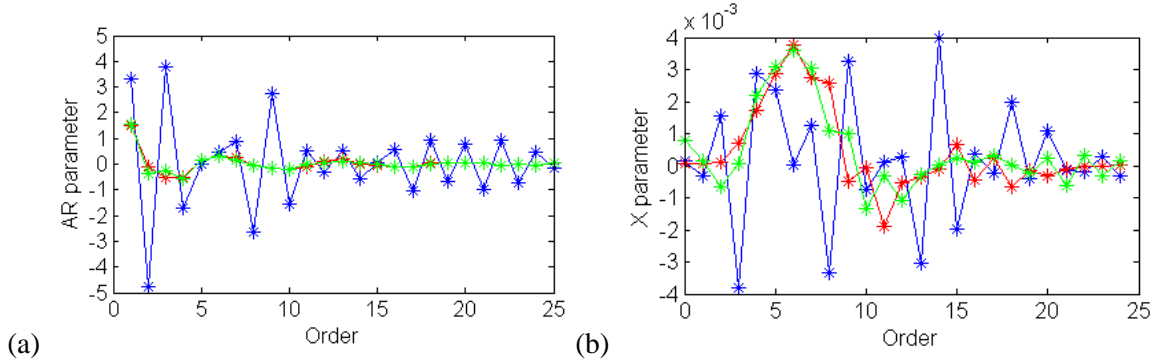


Figure 65: Estimated ARX parameters for the linear system; (a) AR parameters, (b) X parameters, (Blue: R1_lin, Red: R1_lin_num1, Green: R1_lin_num2).

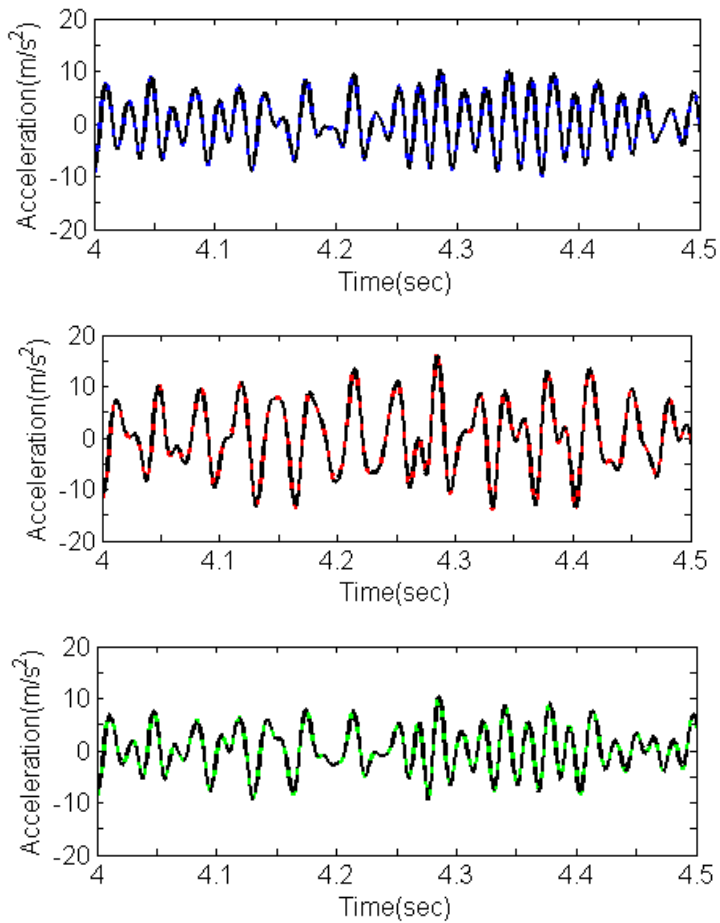


Figure 66: Overlays of original data and time-history from ARX model in the linear system (Blue: $R1_lin$, Red: $R1_lin_num1$, Green: $R1_lin_num2$).

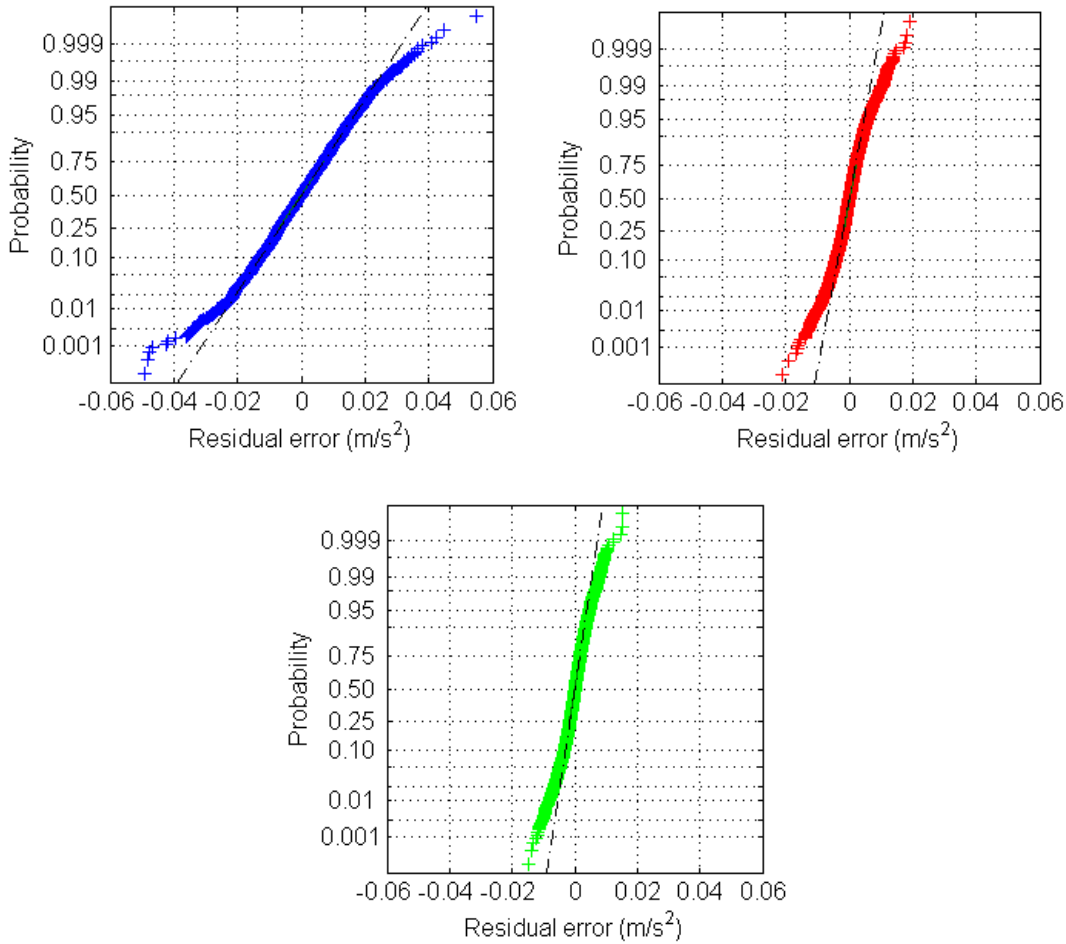


Figure 67: NPPs of estimated residual errors of ARX model in the linear system (Blue: R1_lin, Red: R1_lin_num1, Green: R1_lin_num2).

5.4.3. AR-ARX Model

AR-ARX model estimation is an alternative procedure to derive ARMA model without using a nonlinear parameter identification process. A general ARMA model can be represented by the following equation:

$$x_i = \sum_{j=1}^a \alpha_j x_{i-j} + \sum_{k=1}^b \beta_k f_{i-k} + \varepsilon_i , \quad (37)$$

where α_j and β_k are the AR and MA parameters, respectively, and a and b are their respective orders. The ε_i is an unknown white noise process, and thus, the residual error is estimated at the same time in this model. In the calculation, α_j , β_k , and ε_i must be estimated simultaneously; therefore, this approach generally requires an iterative procedure to solve a general nonlinear optimization problem. Alternatively, the parameters of the ARMA model can be estimated by a two-stage linear identification process (Mayne and Firoozan, 1982). Hannan and Kavalieris (Hannan and Kavalieris, 1984) showed that a high-order AR model was able to approximate any ARMA models arbitrarily well. By fitting a high-order AR(p) model to the output signal x_i in Eq. (27), the estimated residual error e_i , which can be derived by Eq. (31), is obtained and then

considered to be a white noise input. The order of AR model, p , should be larger than the sum of the ARMA orders in Eq. (37), as $p \geq a+b$. Then, an ARX model is formed to estimate the relationship between e_i and x_i .

$$x_i = \sum_{j=1}^a \alpha_j x_{i-j} + \sum_{k=0}^b \beta_k e_{i-k} + \varepsilon_i \quad . \quad (38)$$

The α_j and β_k were then calculated by the least-squares method in this study. Thus, by using a two-step linear approximation procedure, the parameters of the original ARMA model can be estimated without solving a complicated nonlinear optimization problem.

Figure 68 shows the estimated AR and X parameters in the AR-ARX estimation on data associated with random inputs applied to the linear system. In these results, the distributions of both parameters from the two numerical models exhibit completely different tendencies. Examining the first five parameters, the amplitudes of the derived values in Model #L2 are closer to those of the actual structure. Using those parameters, the estimated time-histories agree well with the actual time-history data, as shown in Fig. 69, and the NPPs of residual error, ε_i , in Fig. 70, indicate that all may be described by normal distributions. The deviations of the estimated residual error distributions are significantly smaller than those in the other estimation techniques (i.e., AR and ARX estimations.) As a consequence, the parameters of AR-ARX model are expected to be of use for comparing numerical models with data from the actual structure.

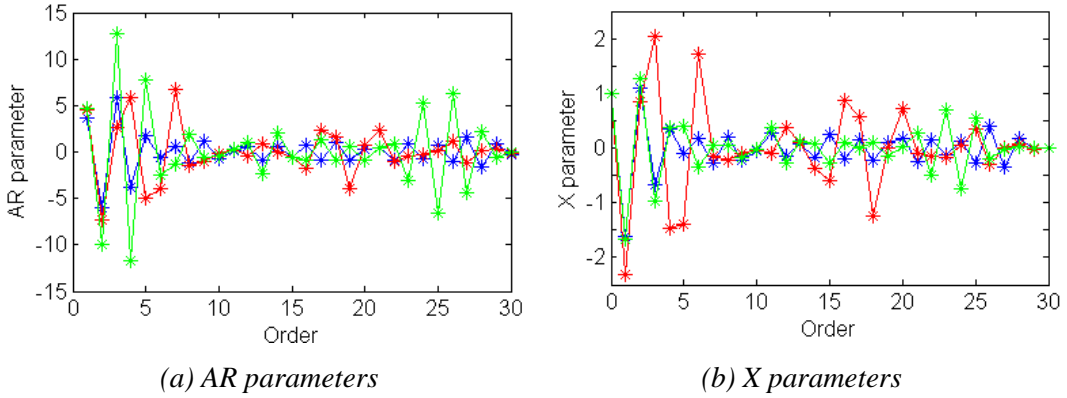


Figure 68: Estimated AR-ARX parameters using estimated residual error from AR (60) model estimation in the linear model (Blue: R1_lin, Red: R1_lin_num1, Green: R1_lin_num2).

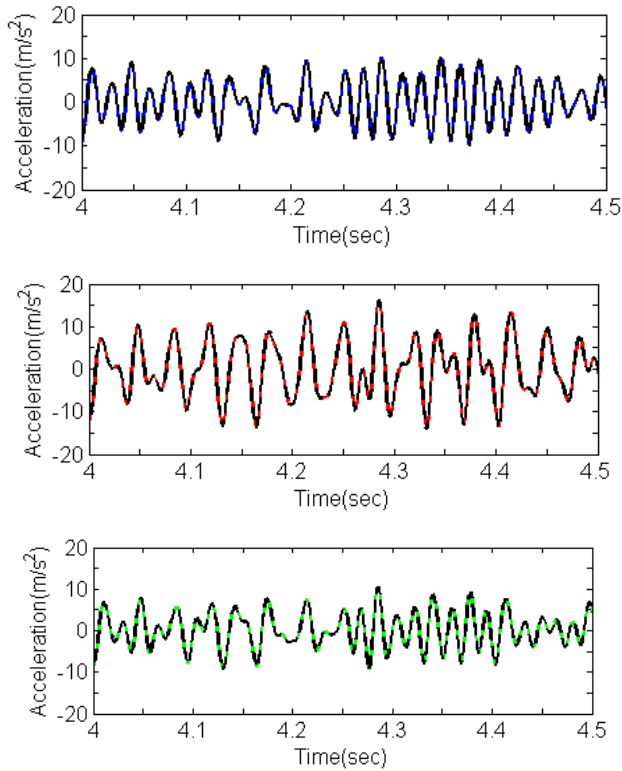


Figure 69: Overlays of original data and time-history from AR-ARX model in the linear system (Blue: R1_lin, Red: R1_lin_num1, Green: R1_lin_num2).

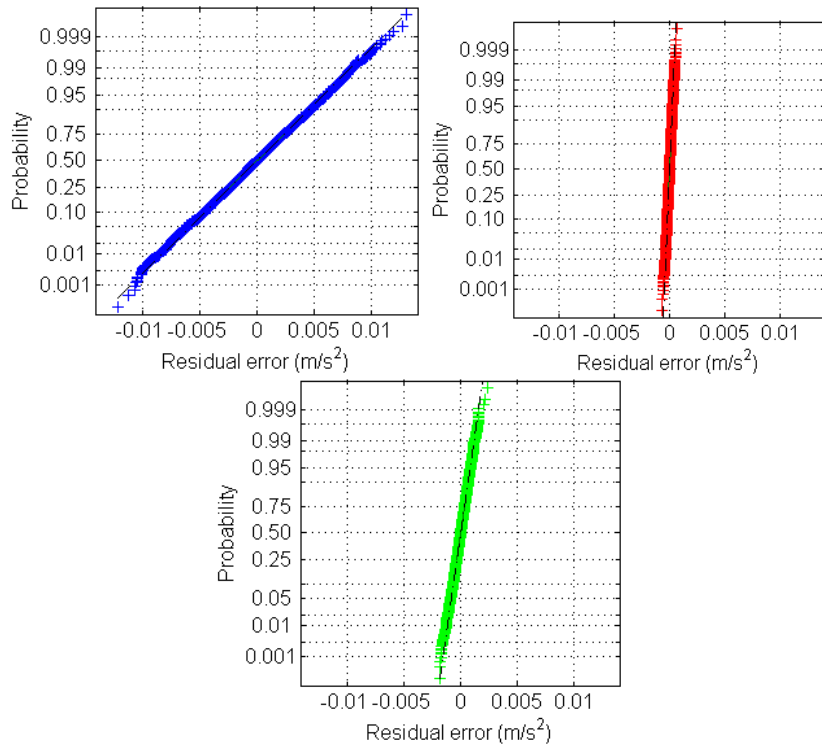


Figure 70: NPPs of estimated residual errors of AR-ARX model in the linear system (Blue: R1_lin, Red: R1_lin_num1, Green: R1_lin_num2).

6. EXAMPLE OF MODEL VALIDATION USING EXTRACTED FEATURES

When multiple aspects of the system response are of interest, the model validation process may require comparing several features that each exhibit their own sensitivity to uncertain model parameters. A multivariate analysis technique is then expected to be useful in this process. Here, the use of the Mahalanobis distance is proposed for the statistical comparison between numerical predictions and experimental measurements using multivariate features. Furthermore, the procedure of quantifying uncertainties of model parameters using the Bayesian inference technique is presented.

6.1. Procedure of Feature Comparison and Uncertainty Analysis

The statistical feature comparison by the Mahalanobis distance for MV described below is based on the outlier detection method established in a previous SHM study (Worden et al., 2000). The procedure for comparing experimental data and numerical runs is first summarized. The procedure of uncertainty analysis is suggested in (Mollineaux et.al., 2011 and Van Buren et. al., 2011). It consists of two procedures; a global sensitivity analysis and an uncertainty quantification process.

6.1.1. Feature Comparison Using Mahalanobis Distance

The Mahalanobis distance is a distance measure for multivariate statistics defined as:

$$D_k = (\mathbf{y}_k - \bar{\mathbf{y}})^T \mathbf{S}^{-1} (\mathbf{y}_k - \bar{\mathbf{y}}), \quad (39)$$

where \mathbf{y}_k is a multi-dimensional feature vector for which the normalized distance from the mean is being calculated, $\bar{\mathbf{y}}$ and \mathbf{S} are a mean vector and a covariance matrix based on all acquired vectors defining the nominal condition, respectively (Mahalanobis, 1936 and Rebba and Mahadevan, 2006). A low distance value D_k can be obtained if \mathbf{y}_k is similar to the set of feature vectors that defines the nominal condition. The five-step procedure to use the Mahalanobis distance is outlined below.

- 1 Acquire experimental data sets from the target structure.
- 2 Create a feature vector for each data set by selecting appropriate features that have sensitivity to the target uncertain model parameters.
- 3 Calculate a Mahalanobis distances for each feature vector from data set k , given as:

$$D_k^E = (\mathbf{y}_k^E - \bar{\mathbf{y}}^E)^T \mathbf{S}_E^{-1} (\mathbf{y}_k^E - \bar{\mathbf{y}}^E) \quad (40)$$

where $\bar{\mathbf{y}}^E$ is the mean vector and \mathbf{S}_E is the covariance matrix of all feature vectors from the experimental data sets. The set of D_k^E is then the experimental baseline distribution of Mahalanobis distance.

- 4 Create a feature vector from the numerical prediction, and calculate a Mahalanobis distance D^N using the mean vector and covariance matrix from the experimental data set; $\bar{\mathbf{y}}^E$ and \mathbf{S}_E ,

$$D^N = (\mathbf{y}^N - \bar{\mathbf{y}}^E)^T \mathbf{S}_E^{-1} (\mathbf{y}^N - \bar{\mathbf{y}}^E) \quad (41)$$

5 Compare the numerical Mahalanobis distance D_k^N with the experimental baseline distribution derived in step 3).

If the feature vector from the numerical output is similar to those from the experimental data set, D^N exhibits a low value. The validity of a numerical model is then investigated statistically by comparing D^N with the experimental baseline distribution.

6.1.2. Uncertainty Analysis of Model Parameters

In a typical uncertainty analysis, the first step is to define the prior uncertainties of model parameters. The second step is to investigate the global sensitivities of numerical outputs to these model parameters. *Uncertainty quantification* usually refers to the propagation of prior uncertainty through the computational model, that is, from model parameters to outputs. Inference uncertainty quantification is the procedure to estimate posterior distributions that indicate the updated uncertainties of model parameters.

6.1.2.1. Global sensitivity of response features to model parameters

Global sensitivity analysis is the procedure used to identify model parameters that exercise significant influence on predictions of the numerical simulation. To do so, we adopt the technique of Analysis-of-Variance (ANOVA) that decomposes the total spread of output predictions caused by varying input parameters (Fisher, 1970 and Saltelli, et al., 2000). The R-squared (R^2) statistic is used to rank individual model parameters, or combinations of parameters, according to the influence that they exercise on model predictions (Draper and Smith, 1998). High R^2 values, relative to the others obtained, indicate effects that significantly influence the output.

The R^2 statistics are estimated from simulation runs performed using sets of uncertain parameters that are configured based on a Design-of-Experiment (DoE) (Myers and Montgomery, 1995 and Kleijnen and Sargent, 2000). First, the comparative feature y_{ij} , which represents the i^{th} ($i = 1, \dots, n$) output prediction under the j^{th} level ($j = 1, \dots, m$) for an uncertain model parameter, is defined as:

$$y_{ij} = \bar{y} + \alpha_j + \varepsilon_{ij} \quad (42)$$

where \bar{y} is the overall sample mean, α_j denotes the deviation of the conditional mean of output predictions under level j : y_j , around \bar{y} , and ε_{ij} is the residual error. Equation (42) can be described as:

$$(y_{ij} - \bar{y}) = (\bar{y}_j - \bar{y}) + (y_{ij} - \bar{y}_j) \quad (43)$$

By squaring both sides of Eq. (43), the total square sum can be represented as the sum of the between-levels square sum and the within-levels square sum. The R^2 statistic then becomes the ratio of the within-level square sum to the total square sum as defined in:

$$R^2 = 1 - \frac{\sum_{j=1}^m \sum_{i=1}^n (y_{ij} - \bar{y}_j)^2}{\sum_{i=1}^n \sum_{j=1}^m (y_{ij} - \bar{y})^2}. \quad (44)$$

Comparing R^2 statistics estimated for each model parameter provides a relative ranking of the influence that each parameter exercises on the output (comparative feature).

6.1.2.2. Inference uncertainty quantification using the GPM/SA software

The Gaussian Process Modeling for Simulation Analysis (GPM/SA) code was developed at LANL (Higdon et al., 2008) and is used here to perform the inference uncertainty quantification. The posterior probability distribution of model parameters is obtained by Bayesian inference, a backward propagation that updates the distribution such that the variability of model predictions becomes statistically consistent with the variability of experimental measurements. To mitigate the potentially high computational expense, the backward propagation of uncertainty is performed using the Metropolis-Hastings method, which is one of the Markov Chain Monte Carlo (MCMC) algorithms (Gilks, 1996). It basically consists of taking random walks within the space of model parameters θ according to their initial probability distribution $p(\theta)$. Model predictions obtained with parameters θ are compared to the experimental measurements using a maximum likelihood criterion to decide whether they should be included in the posterior distribution. A sampling point θ is thus accepted if it yields predictions that are statistically consistent with the measurements.

In order to obtain a sufficiently accurate posterior distribution of model parameters using MCMC sampling, a large number of FE model runs are required to calculate the response features. This process can lead to extremely large and unaffordable simulation times. To address this issue, a surrogate model (or emulator) is developed to replace the expensive FE model by a mathematical function that mimics the relationship between the inputs and outputs. The statistical model for the relationship is defined as a Gaussian process, which offers the benefits of being non-parametric and flexible through the use of a mean term and covariance function. This procedure was proposed for univariate analysis (Kennedy and O'Hagan, 2000) and generalized for multivariate analysis (Higdon et al., 2008). To define the surrogate model, numerical simulations are performed using a Latin hypercube sampling of the model parameters (McKay, Beckman, and Conover, 1979).

6.2. Application to the Linear System Model Validation

The application, here, is the linear model of the test-bed three-story structure, which is also used in the feature extraction study. The uncertain/calibration model parameters are the damping coefficients of the lumped-mass model.

6.2.1. Experimental Data Sets

An experimental baseline distribution is created by acquiring twenty data sets: "Exp. data #1-#20," under the same linear condition (without the bumper-column mechanism) of the test-bed three-story structure. The input force is a band-limited random excitation with frequency range of 20-200 Hz and amplitude of 2.5 Vrms. The acceleration-time responses at each floor were characterized with 16,384 points acquired at a sampling frequency of 640 Hz.

6.2.2. Numerical Predictions

Damping coefficients are influential parameters for the prediction of the time-history response of the linear lumped-mass system. To reduce the number of parameters, a proportional damping model is adopted (Clough and Penzien, 1993 and Weaver and Johnston, 1987). The damping matrix \mathbf{D} can be described by the mass matrix \mathbf{M} and the stiffness matrix \mathbf{K} , as follows:

$$\mathbf{D} = \alpha \mathbf{M} + \beta \mathbf{K} \quad (45)$$

The coefficients α and β can be related to i^{th} -mode damping ratio ζ_i and the resonant frequency ω_i as:

$$\zeta_i = \frac{1}{2} \left(\frac{\alpha}{\omega_i} + \beta \omega_i \right). \quad (46)$$

Therefore, the damping behavior in the entire frequency range can be assigned simply by providing the second-mode and fourth-mode damping ratios.

Table 17: Prior ranges of the Second- and Fourth-Mode Damping Ratios for the Linear Model.

Parameter	Minimum Bound	Maximum Bound
Second-mode damping ratio	0.010	0.080
Fourth-mode damping ratio	0.001	0.020

The simulation set, which consists of 200 runs (Run #1-#200), is created using 200 sets of damping parameter values sampled from the prior uniform ranges of the second and fourth modal damping ratios, as indicated in Table 17. This 200-run Latin hypercube sample is shown in Fig. 71. The input force in all calculations is the same time-history response that was measured in the experimental data set Exp. data #10. The accuracy of each numerical run relative to experimental measurements is described by the root-mean-square of residual errors (RMSE). The value for numerical run k is calculated as:

$$R_k = \sqrt{\frac{1}{n} \sum_{i=1}^n (x_{ki}^N - x_i^E)^2}, \quad (47)$$

where x_{ki}^N is the numerical prediction, x_i^E is the experimental data in Exp. Data #10, and n is the total number of data points.

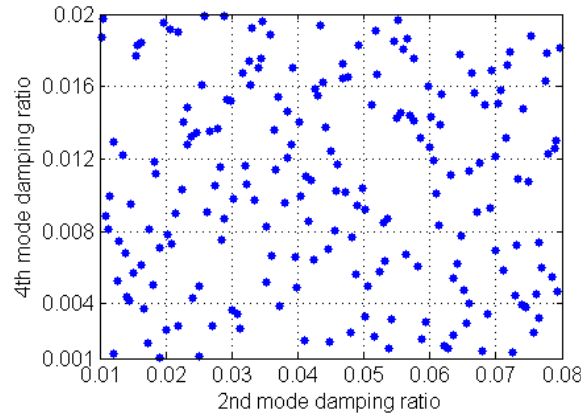


Figure 71: Parameter sets sampled by Latin hypercube for the linear model (200 runs).

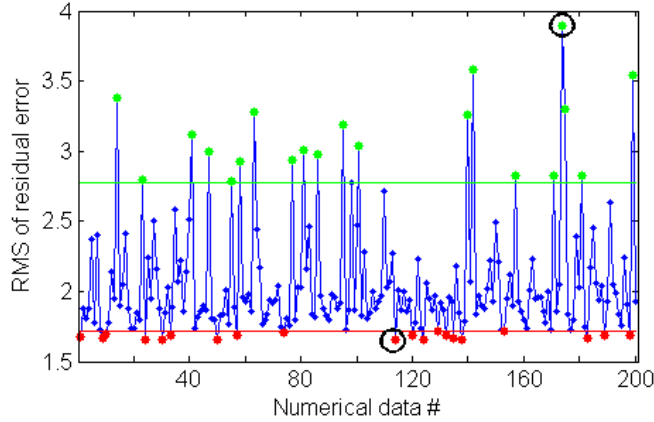
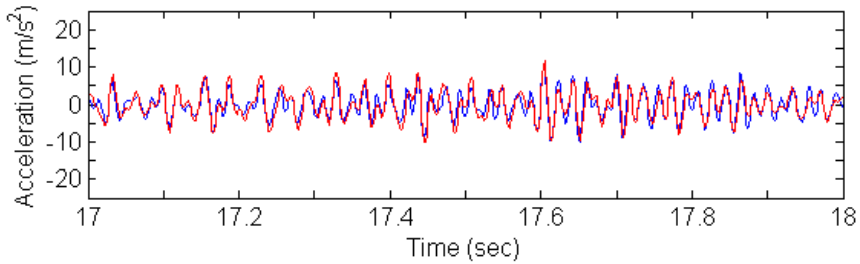
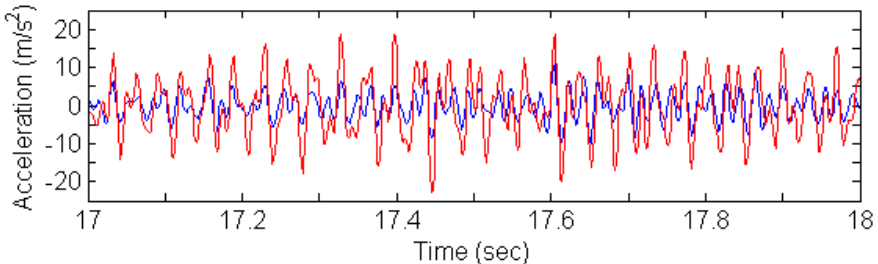


Figure 72: RMSE values of time-histories for the 200 runs of the linear model.

Figure 72 illustrates the accuracy of the 200 runs for the third floor acceleration response. Runs that provides the lowest twenty RMSE values and highest twenty RMSE values are indicated by red points and green circles, respectively. The best accuracy is obtained for Run #114 with damping ratios $(\zeta_2, \zeta_4) = (0.046, 0.070)$. The worst accuracy is obtained for Run #174 with coefficients $(\zeta_2, \zeta_4) = (0.0122, 0.0013)$.



(a) Simulation run #114 (lowest RMSE value).



(b) Simulation run #174 (highest RMSE value).

Figure 73: Overlay of the measured and simulated time-histories (blue: experimental response, red: numerical response).

Figure 73 shows overlays of these numerical runs (#114 and #174) with the reference experimental measurement Exp. Data #10. It is clear that the difference in damping coefficients significantly influences the amplitude level of the global response.

6.2.3. Feature Extraction and Mahalanobis Distance Calculation

Response features for global waveform analysis are used to study the overall amplitude levels caused by different values of damping ratios. Because the power of random signal is distributed uniformly in time, a high time-resolution is not required; therefore, basic statistics and temporal moments are considered to be applicable features.

Figures 74 and 75 plot the Mahalanobis distances derived from the feature vectors consisting of five basic statistics and the first five temporal moments, respectively. Both feature vectors are calculated from the responses of the second and third floors. Blue dots in the figures are the experimental baselines calculated from Exp. Data #1-#20 and black dots represent the distributions of numerical runs Run #1-#200. The red and green circles indicate runs that produce the lowest and highest twenty RMSE values, respectively.

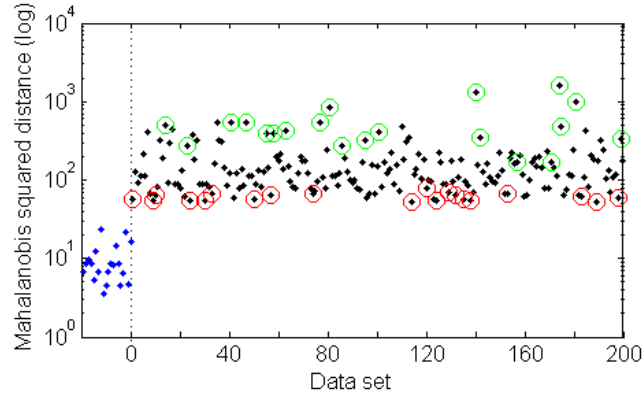


Figure 74: Mahalanobis distances for feature vectors defined with five basic statistics (blue dots: experiments, black dots: simulations, red circles: runs with lowest RMS residual errors, green circles: runs with highest RMS residual errors).

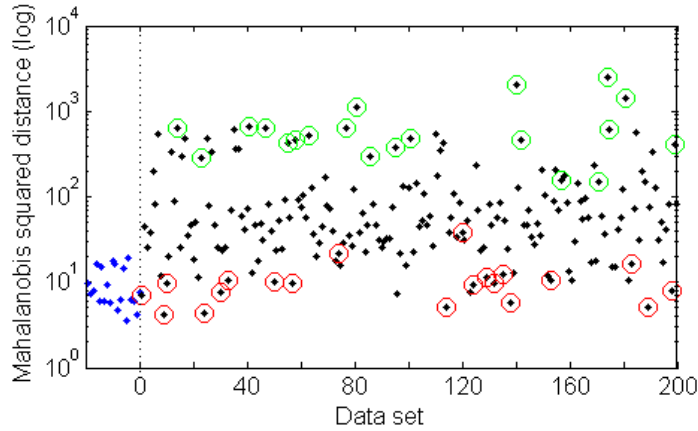


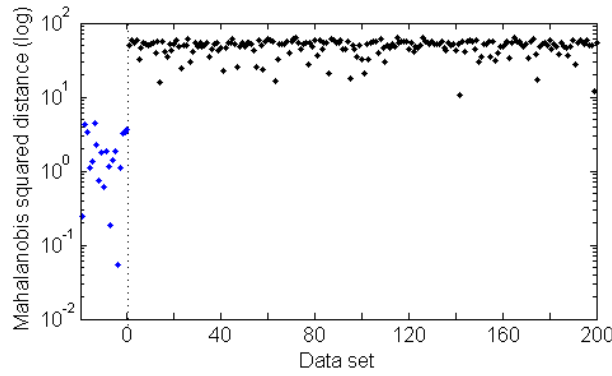
Figure 75: Mahalanobis distances for feature vectors defined with the first five temporal moments (blue dots: experiments, black dots: simulations, red circles: runs with lowest RMS residual errors, green circles: runs with highest RMS residual errors).

A desirable tendency is observed in both figures. The accurate numerical runs indicated by red circles are distributed in low ranges of the Mahalanobis distance. Conversely the inaccurate runs indicated by green circles correspond to high values of the Mahalanobis distance. In comparison

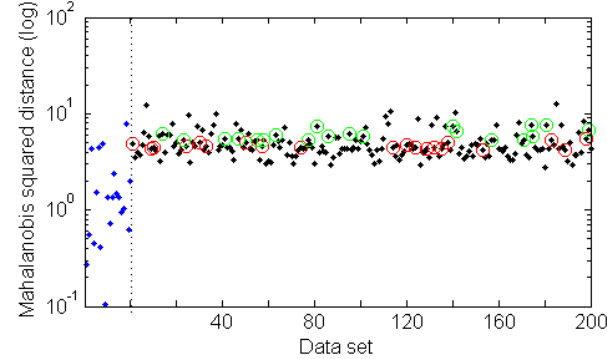
to the experimental distributions, however, the distance values of numerical runs are high especially for some of the feature vectors that collect five basic statistics as shown in Fig. 74. An explanation for this observation is suggested next.

The reason for observing the large spread in the values of the Mahalanobis distance in Figs. 74 and 75 is that the different statistics, or temporal moments, have different orders of magnitude. This result can be observed in Fig. 76 (a) and (b) where the feature vectors used to calculate Mahalanobis distances are limited to skewness statistics and kurtosis, respectively. One can see most of the skewness statistics have a magnitude in the range of approximately 70–80 while the magnitudes of the kurtosis values are approximately in the range of 4–5.

Furthermore, it can be seen that the resulting Mahalanobis distances shown in Fig. 76 (a) and (b) are not too sensitive to variations of the damping coefficients propagated in the Latin hypercube sample. These observations lead to the conclusion that these features should not be included as components of a feature vector.



(a) Mahalanobis distances obtained with the skewness statistics.



(b) Mahalanobis distances obtained with the kurtosis statistics.

Figure 76: Mahalanobis distances obtained with a single type of response features (blue dots: experiments, black dots: simulations, red circles: lowest values of the RMS residual error, green circles: highest values of the RMS residual error).

Figure 77 shows the Mahalanobis distances derived from feature vectors composed of the peak amplitude and standard deviation. These response features are selected because they exhibit similar sensitivities to the accuracy of time-histories. The figure indicates that numerical runs with low and high RSME values are more clearly extracted. In addition, runs that feature the lowest twenty RSME values are distributed in the same range as the experimental distribution.

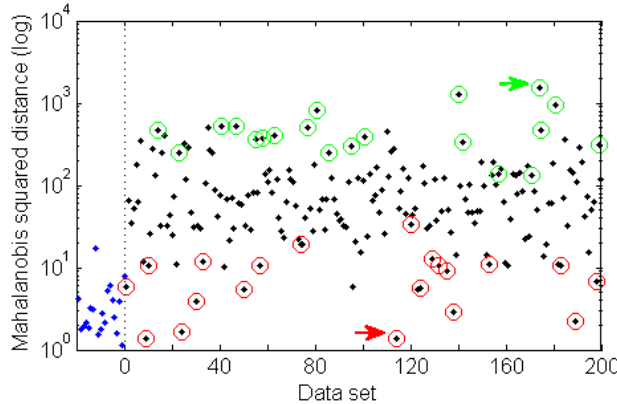


Figure 77: Mahalanobis distances for feature vectors defined with the peak amplitude and standard deviation (blue dots: experiments, black dots: simulations, red circles: runs with lowest RMS residual errors, green circles: runs with highest RMS residual errors).

The numerical runs #114 and #174, which have the lowest and the highest RMSE values, correspond to the lowest and highest Mahalanobis distances, respectively. These results suggest that the response features useful to validate predictions of the linear model are the peak amplitude and standard deviation of time-histories. This application indicates that, to be appropriate and effective, a comparison between experimental measurements and simulation predictions should involve response features that exhibit similar sensitivities to variations of the uncertain model parameters.

6.2.4. Consistency Check of the Mahalanobis Distance Comparison

This section verifies the consistency of Mahalanobis distances, that is, whether the model parameters corresponding to the lowest values of distance provide accurate predictions of time-history responses for any input force.

An additional twenty numerical runs are calculated using the damping parameters that yield the lowest Mahalanobis distance in Fig. 77, i.e., the numerical model of Run #114 for which $(\zeta_2, \zeta_4) = (0.046, 0.070)$. The input force data labeled Exp. Data #1-#20 are used to drive the time response of the system. Figure 78 depicts the RMSE values of the additional twenty runs, shown with green dots and compared to the values obtained with the previous 200 runs (blue line and dots). It is clear that equivalent or better accuracy is obtained in all of the twenty runs.

The Mahalanobis distances obtained for the new set of twenty runs are also presented in Fig. 79. It can be observed that their distribution is similar to that of values obtained for the experimental measurements. This result indicates that model parameter sets that yield low values of the Mahalanobis distance consistently provide accurate predictions of the time-history response. It can then be concluded that the statistical validity of model parameters can be evaluated by the Mahalanobis distance comparison method.

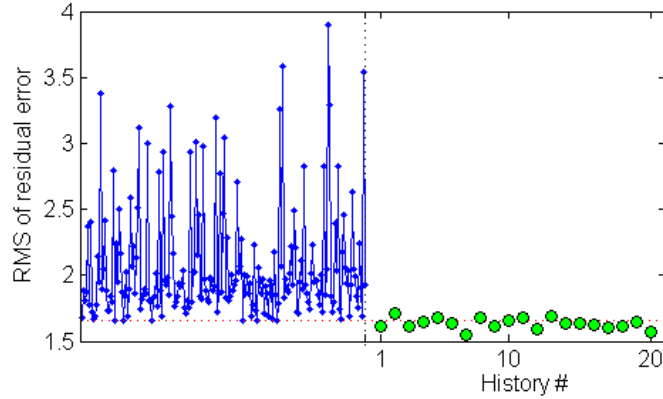


Figure 78: RMSE values of numerical predictions obtained with the calibrated damping ratios and different input forces (blue: predictions obtained with the Latin hypercube sampling set, green: predictions obtained with the calibrated model parameters).

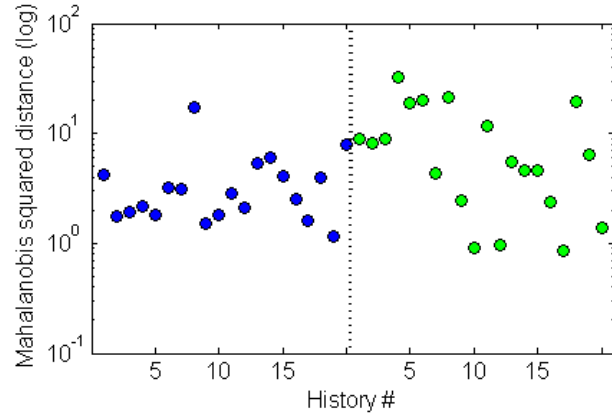


Figure 79: Mahalanobis distances for feature vectors defined with the peak amplitude and standard deviation of time-history responses (blue dots: experiments, green dots: predictions obtained with the calibrated damping ratios).

6.2.5. Uncertainty Analysis and Model Calibration

As mentioned in the previous section, the feature selection is important for comparisons between experimental measurements and numerical predictions. Global sensitivity analysis, which studies the influence that model parameters exercise on response features, can provide meaningful information for feature selection. Moreover, the calibration of model parameters can be formulated as a problem of Bayesian inference uncertainty quantification, solved with the GPM/SA software.

6.2.5.1. Global sensitivity analysis of response features to the damping ratios

This section assesses the global sensitivities of response features to damping coefficients. A design-of-experiments is first executed to provide numerical runs where the damping coefficients are simultaneously varied. The R^2 -statistics are then estimated to assess the sensitivities.

The numerical runs are first executed using parameter sets created by a three-level full-factorial design-of-experiment (see Table 18). Table 18a shows the three levels defined for each damping

coefficient; and Table 18b defines the full-factorial design whereby the lower, nominal and upper levels are combined for each variable. The range of values for each damping parameter is the same range as shown in Table 17.

Table 18: Sampling of Model Parameters for the Estimation of R²-Statistics.

(a) *Levels of damping ratios for the design-of-experiments.*

Damping Ratio	Level = -1	Level = 0	Level = +1
Second-mode damping ratio	0.010	0.0450	0.080
Fourth-mode damping ratio	0.001	0.0105	0.020

(b) *Definition of the full-factorial design-of-experiments.*

Run Number	Second-Mode Damping Ratio	Fourth-Mode Damping Ratio
1	+1	+1
2	+1	0
3	+1	-1
4	0	+1
5	0	0
6	0	-1
7	-1	+1
8	-1	0
9	-1	-1

Table 18 (b) indicates that the two-variable, three-level full-factorial design produces a total of $3^2 = 9$ numerical runs. These runs are executed one-by-one, each one using a different combination of damping ratios. The peak amplitude, standard deviation and five temporal moments are then extracted from the time-history responses for the nine runs.

The resulting R²-statistics are summarized in Table 19. These results clearly indicate that features extracted from the time-history responses of the second floor (Channel #4) have relatively high sensitivities to the fourth-mode damping ratio. Likewise features of the third floor (Channel #5) are sensitive to the second mode damping ratio.

In addition to identifying response features that exhibit high sensitivities to one of the damping ratios, Table 19 also shows that several features have little-to-no sensitivity to one damping ratio or another. Features with low global sensitivities are poor candidates for model validation because varying the model parameters does not change the response predictions.

Table 19: R^2 Relative Influence that Damping Ratios Exercise on Response Features.

Channel	Feature	Second-Mode Damping Ratio	Fourth-Mode Damping Ratio
#4	Peak value	3.8%	96.6%
	Standard deviation	3.8%	96.2%
#5	Peak value	78.2%	21.7%
	Standard deviation	78.4%	21.6%
#4	Energy (E)	3.3%	96.7%
	Centroid (T)	4.4%	95.6%
	RMS duration (D)	2.4%	97.6%
	Skewness (S)	19.9%	80.1%
	Kurtosis (K)	1.3%	98.7%
#5	Energy (E)	79.1%	20.9%
	Centroid (T)	64.1%	35.9%
	RMS duration (D)	66.8%	33.2%
	Skewness (S)	65.8%	34.2%
	Kurtosis (K)	56.5%	43.5%

To validate the values of the second- and fourth-mode damping ratios, the feature vector used for analysis should contain response features that are sensitive to these two model parameters. The Mahalanobis distances shown in Fig. 77, which are obtained with the peak and standard deviation features extracted from the second- and third-floor time-history responses, show sensitivities appropriate for model validation.

6.2.5.2. Calibration of the damping ratios

The uncertain parameters, which are the second-mode and fourth-mode damping ratios of the linear model, are calibrated with the GPM/SA code to improve the test-analysis correlation between response features of the experimental and numerical outputs. A 200-run Latin hypercube design-of-experiments is defined to sample these parameters. The fourteen features listed in Table 19 are extracted from each of 20 experimental data sets and 200 simulation runs of the linear model. These response features are used to develop the statistical emulators of the GPM/SA code mentioned in Section 6.1.2.2.

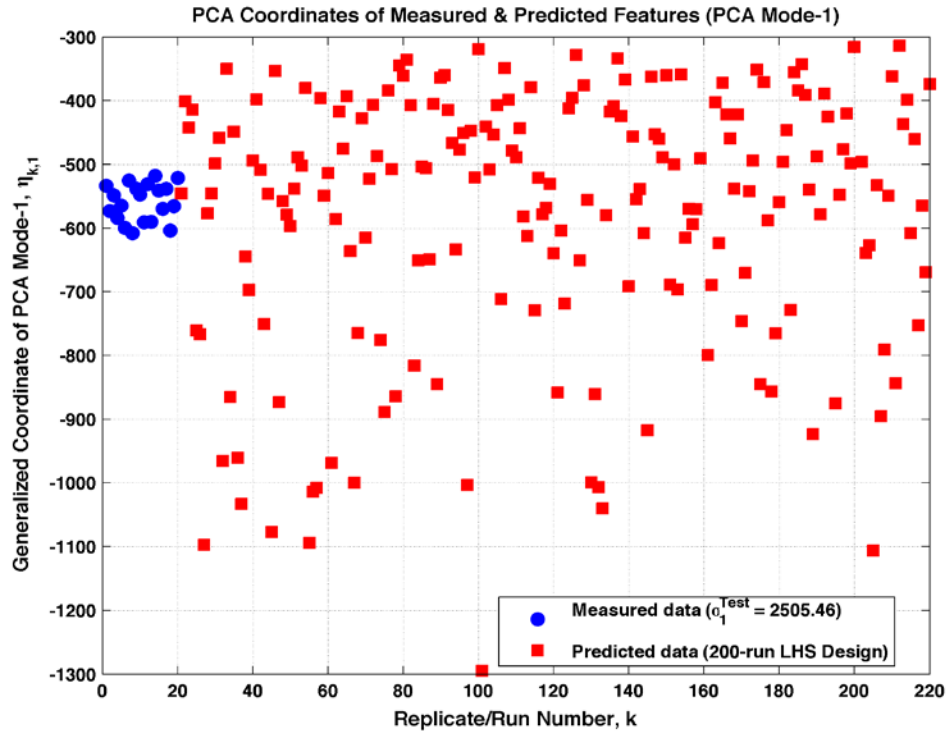
It is observed, however, that some of the fourteen response features are highly correlated. Such a correlation can lead to inefficient inference uncertainty quantification because the algorithm is provided with redundant data. To mitigate this issue and work within a response feature space restricted to independent information, the fourteen features are first transformed using the Principal Component Analysis (PCA) (Hotelling, 1933 and Hasselman, Anderson, and Wenshui, 1998). Table 20 shows that the first two PCA generalized coordinates contain more than 98% of the total information. This means that most of the information given in the initial list of fourteen response features is really only two-dimensional.

**Table 20: Principle Component Analysis of the Feature Vector of 14 Features
(Basic Statistics and Temporal Moments).**

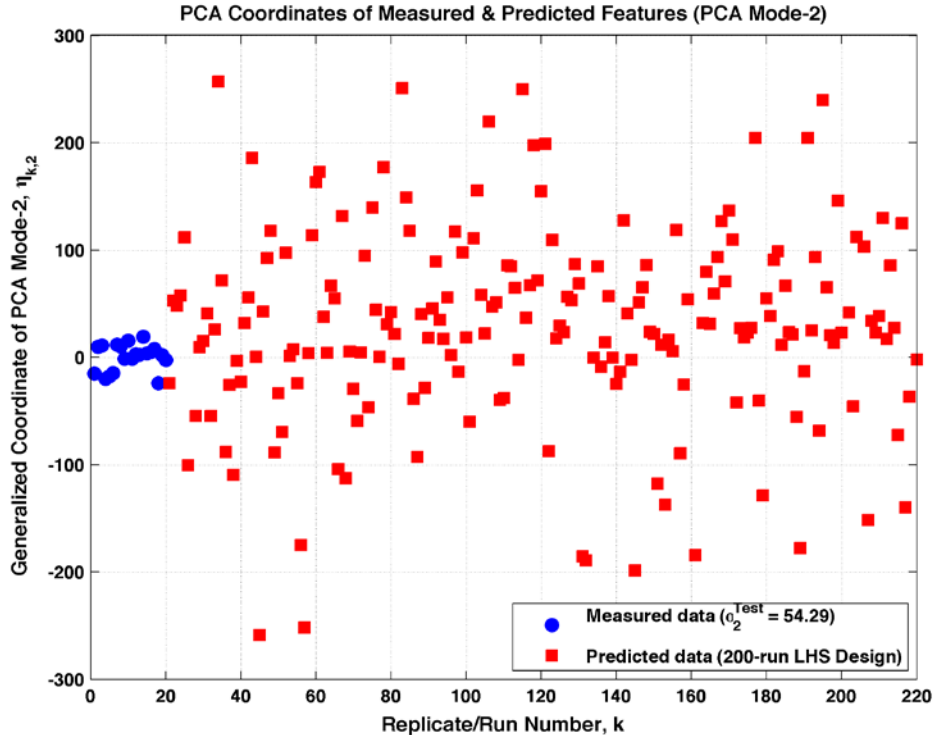
PCA Mode	Measured Singular Value (Percent)	Total Contribution	Measured Coordinate (Mean \pm St. Dev.)	Predicted Coordinate (Mean \pm St. Dev.)
1	2505.46 (96.47%)	96.47%	-559.51 \pm 29.21	-594.07 \pm 235.17
2	54.29 (2.09%)	98.56%	0.26 \pm 12.45	23.46 \pm 106.17
3	16.63 (0.64%)	99.20%	0.06 \pm 3.82	-1.80 \pm 6.20
4	5.56 (0.21%)	99.41%	-0.03 \pm 1.28	-0.02 \pm 3.31
5	5.38 (0.21%)	99.62%	0.03 \pm 1.23	-0.42 \pm 4.25
6	4.12 (0.16%)	99.78%	0.02 \pm 0.94	-3.58 \pm 8.97
7	3.08 (0.12%)	99.89%	0.007 \pm 0.71	-0.30 \pm 3.08
8	1.37 (0.05%)	99.95%	0.001 \pm 0.32	-0.45 \pm 0.75
9	0.58 (0.02%)	99.97%	0.0005 \pm 0.13	-0.06 \pm 0.23
10	0.48 (0.02%)	99.99%	-0.0002 \pm 0.11	0.10 \pm 0.26
11	0.16 (0.01%)	100.00%	-0.00000 \pm 0.04	-0.004 \pm 0.08
12	0.07 (0.00%)	100.00%	0.00009 \pm 0.02	-0.075 \pm 0.16
13	0.05 (0.00%)	100.00%	-0.00002 \pm 0.01	0.059 \pm 0.12
14	0.004 (0.00%)	100.00%	-0.00000 \pm 0.001	-0.010 \pm 0.11

Figure 80 shows the first two PCA generalized coordinates extracted from the measured features (blue circles) and predicted response features (red squares). The ranges of these measured and predicted distributions in generalized coordinates are similar, which is needed for test-analysis correlation. Furthermore, the predicted coordinates bracket the measured coordinates, indicating that the two damping coefficients can be explored to successfully find models whose predictions reproduce the measurements.

The first two PCA components are used in the estimation of the posterior distribution of damping ratios using the GPM/SA code. The calibration of uncorrelated and independent PCA coordinates, as opposed to correlated response features, can significantly reduce the posterior uncertainty. The MCMC iterations are initialized with 150 burn-in iterations and 11 step-size trials. A total of 100,000 iterations are performed to explore the posterior distribution.



(a) Generalized coordinates of the first PCA mode.



(b) Generalized coordinates of the second PCA mode.

Figure 80: Comparison of measured and predicted PCA generalized coordinates of the fourteen-feature vectors (blue circles: experiments, red squares: predictions).

Figure 81 illustrates the exploration of the posterior distribution of damping ratios. The parameters labeled θ_1 and θ_2 represent the second- and fourth-mode damping ratios, respectively. The two inserts on the main diagonal represent the empirical histograms of values sampled by the MCMC iterations. These are the damping ratios that, when used to predict the time-history responses using the linear model, tend to predict response features that match those of the experimental measurements. The off-diagonal insert of Fig. 81 indicates the correlation of values sampled. It shows that the correlation between the two model parameters is not statistically significant, which is a welcome observation to avoid trade-offs between the two damping ratios.

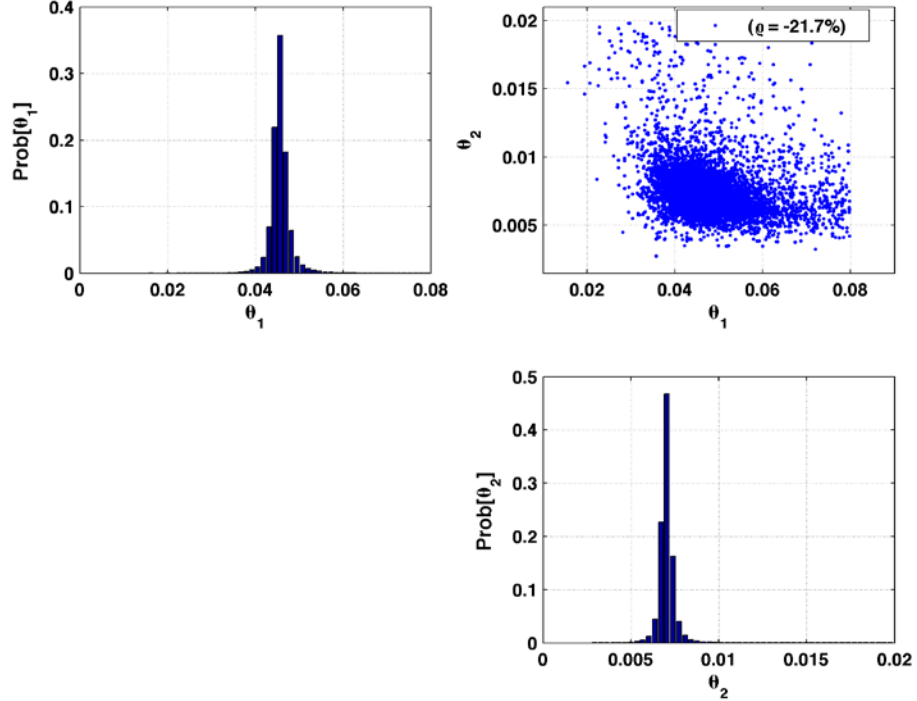


Figure 81: Posterior probability distribution of damping ratios of the linear model.

Table 21: Statistics of two calibrated damping ratios.

Model Parameter	Prior Statistics			Posterior Statistics	
	Minimum	Maximum	Range	Mean	Std. Dev.
Second-mode damping ratio	0.01027	0.07980	0.06953	0.04584	0.00295
Fourth-mode damping ratio	0.00101	0.01992	0.01891	0.00707	0.00067

Figure 81 shows that the uniform prior ranges of damping coefficients are significantly narrowed to smaller intervals that yield good-quality agreement between predictions and measurements. Table 21 summarizes statistics extracted from the posterior distribution of Fig. 81. The reduction of prior to posterior uncertainty is particularly significant for the 4th-mode damping ratio. Six standard deviations of the posterior uncertainty, for example, represent a range of $\pm 3\sigma = 0.0040$, which is a 96% reduction of uncertainty relative to the prior range of 0.0189. The mean values of the posterior distribution are 4.58% and 0.71% for the second-mode and fourth-mode damping ratios, respectively.

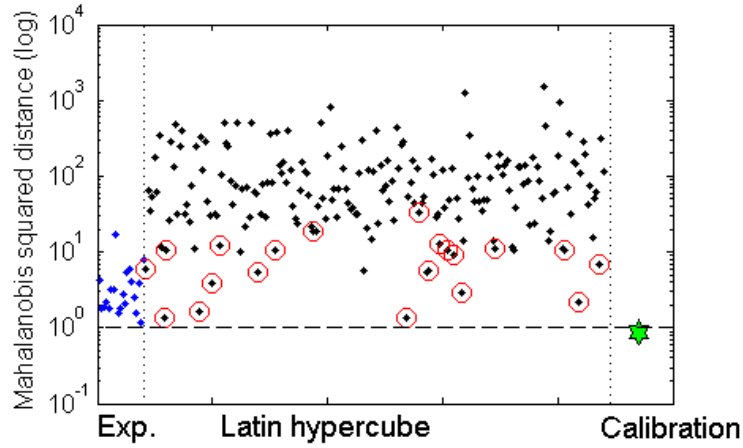


Figure 82: Mahalanobis distances with and without calibrated damping ratios (blue dots: experiments, black dots: predictions from the Latin hypercube sample, red circles: accurate predictions, green star: prediction with the calibrated damping ratios).

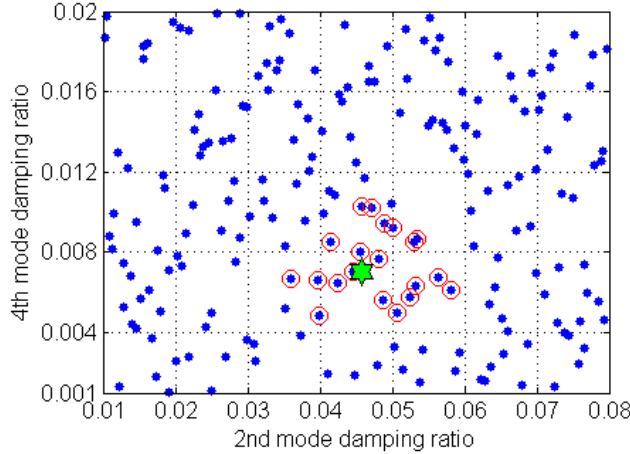


Figure 83: Values of damping ratios used for sampling and calibration (blue dots: Latin hypercube samples, red circles: damping ratios that yield accurate predictions, green star: calibrated damping ratios).

The mean values of the posterior distribution listed in Table 21 are used to define what we refer to here as the calibrated damping ratios. This calibration is fed to the linear model to predict the time-histories from which the same fourteen response features are extracted. Figure 82 indicates how the Mahalanobis distance of the calibrated solution compares to those obtained with the measurements and samples of the (prior) Latin hypercube design. Feature vectors defined to calculate these Mahalanobis distances are composed of peak amplitudes and standard deviation values of time-history signals. Figure 83 illustrates where these different samples are located in the two-dimensional space of damping ratios.

The low value of Mahalanobis distance obtained with the calibrated parameters indicates in Fig. 82 that this solution reproduces the measurements with the best accuracy. In particular the calibrated prediction (green star) is more accurate than most of the predictions provided by damping ratios sampled from the prior distribution (black dots).

Figure 83, which is basically the same plot as Fig. 71, represents the two damping ratios. Blue dots indicate the 200 parameter sets sampled with the Latin hypercube design from the prior ranges of Table 21. Red circles indicate the pairs of damping ratios that yield the lowest twenty RSME values of residual error between measurements and predictions. Because the calibrated parameters are defined as mean values of the posterior distribution, this solution (green star) is located at the center of the area defined by the red circles. This observation demonstrates that the inference uncertainty quantification technique implemented in the GPM/SA code provides, 1) a significant reduction of parameter uncertainty, and 2) a set of calibrated damping ratios capable of accurately reproducing the measurements.

6.3. Application to the Nonlinear System Model Validation

The success of calibrating damping ratios of the linear model using a method of inference uncertainty quantification is realized by the selection of appropriate response features. The importance of feature selection is further confirmed when studying the validation of the nonlinear model, as discussed in this section.

6.3.1. Experimental Data and Numerical Runs

Here, the uncertain parameters are those used to model the bumper mechanism illustrated in Fig. 11. The three parameters considered are Gap , the clearance between bumper and suspended column, also used to define the maximum displacement of the linear force-displacement model; Δ , the displacement of the linear-to-nonlinear transition region; and k_B , the bending stiffness of the suspended column. The two damping ratios of the linear model are kept constant and equal to the values calibrated in Section 6.2.5.2. The goal is to repeat the study discussed previously for the triplet of model parameters (Gap ; Δ ; k_B) and assess if the parameter uncertainty can be reduced using time-history responses of the nonlinear system where the bumper mechanism is engaged.

The experimental baseline of measurements is first created from twenty experiments (Exp. Data #N1–#N20) acquired under the same random excitation as that of the linear system data acquisition. The clearance between the bumper and suspended column is set to $Gap = 0.1$ mm in all measurements. Adjustment of the clearance is carried out before each data acquisition using a feeler gauge. This procedure causes some variability in the actual values of parameters Gap and Δ . The value of bending stiffness k_B is also uncertain because it is difficult to estimate the effect that a short-duration contact of the suspended column against the bumper has in terms of stiffening the system.

In addition to the uncertainty where parameters (Gap ; Δ ; k_B) are unknown or can vary, one could also consider model-form uncertainty in the formulation of the problem. Model-form refers to assumptions made about the equations to be solved, not just parameter values for given fixed equations. One example is which beam theory should be adopted (*Euler-Bernoulli* or *Timoshenko*) to describe the column stiffness k_B . Notice that model-form, even though it can be a dominant form of uncertainty for many applications, is not considered in this report.

Numerical responses (Runs #N1–#N400) are calculated for a set of 400 parameter triplets (Gap ; Δ ; k_B) sampled from the prior ranges given in Table 22 with a Latin hypercube design. All of 400 numerical outputs are calculated by applying the same input force that is one of the force signals acquired in the experiments.

Table 22: Prior Ranges of Parameters (Gap ; Δ ; k_B) of the Nonlinear Model.

Symbol	Model Parameter	Minimum	Maximum
Gap	Bumper-to-suspended-column clearance (mm)	0.05	0.15
Δ	Displacement of stiffening transition region (mm)	0.00	1.00
k_B	Column stiffness ($\times 10^6$ N/m)	0.9625	2.8875

Figure 84 depicts the RMSE values obtained for the 400 simulation runs, where the residual error is defined as the difference between measured and predicted responses for the third floor. Runs that produce the lowest residual errors are identified with red dots and runs that yield the highest residual errors are shown with green dots. Of these, the most accurate (#N256) and least accurate (#N211) models are extracted and compared, in Fig. 85, to the experimentally measured acceleration signal.

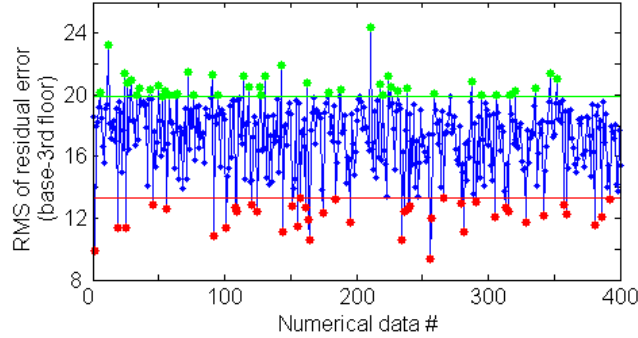
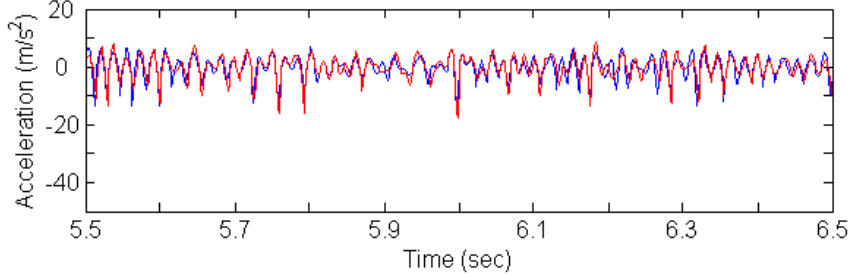
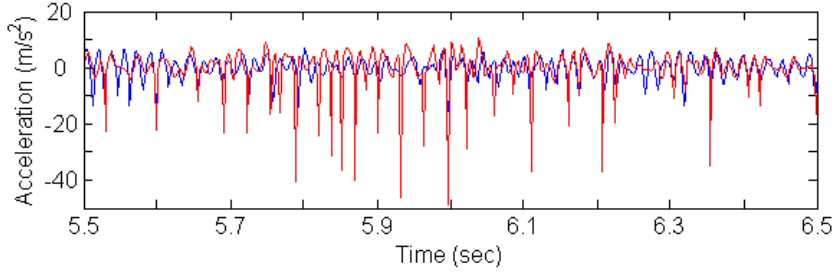


Figure 84: RMSE of time-histories for the 400 simulations of the nonlinear model.



(a) Most accurate nonlinear model (Run #N256) with the lowest RMSE.



(b) Least accurate nonlinear model (Run #N211) with the highest RMSE.

Figure 85: Comparisons of experimental (blue) and numerical (red) time-histories.

It is observed that although the periods of measured and predicted waveforms show agreement in both cases, the difference between the two models originates from the amplitudes of the predicted responses especially at impact events. The predicted signal of Fig. 85(a), which corresponds to the best-case RMSE, matches the measured signal with excellent accuracy. The predicted signal of Fig. 85(b), which corresponds to the worst-case RMSE, features much more pronounced decelerations from the contacts between the bumper and suspended column than those of the measured acceleration signal. From the comparison between these two extreme cases, it is clear that the ability to predict the measurements is greatly influenced by the triplet of uncertain parameters (Gap ; Δ ; k_B).

6.3.2. Feature Selection and Mahalanobis Distance Comparison

Based on the observation of the waveform differences between runs #N256 and #N211 in Fig. 85, it is expected that response features suitable for test-analysis correlation of the nonlinear model are those which assess the waveform amplitude. The standard deviation is selected. This feature, however, is considered to be too global to meaningfully compare not only the amplitude but also the frequency of impact events.

To better resolve the amplitude and frequency information of impacts in the time domain, each time-history signal, the length of which is 4,096 points, is divided into 64 segments labeled Segment #1–#64. Figure 86 illustrates this decomposition. The feature vector defined for test-analysis correlation of each time-history collects the standard deviations estimated within each one of the 64 segments.

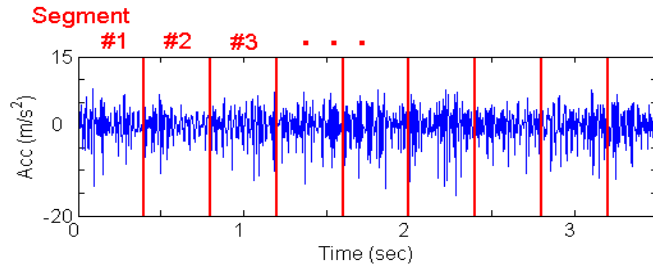


Figure 86: Segments defined for feature extraction in each time-history.

Figure 87 plots the Mahalanobis distances obtained for the 400 training runs of the Latin hypercube design. The twenty lowest RSME values, indicated by red circles, tend to correspond to low values of the Mahalanobis distance. Likewise the twenty runs with the highest RSME values, indicated by green circles, correspond to those which have high values of Mahalanobis distance. This result suggests that the Mahalanobis distance of an appropriate feature vector is a good proxy of the test-analysis correlation of time-history responses for a linear or nonlinear system. It can also be observed that the run with the lowest Mahalanobis distance is the same (Run #N256) as that with the lowest RSME shown in Fig. 85(a). The run with the highest Mahalanobis distance is that with the lowest RSME (Run #N211) shown in Fig. 85(b).

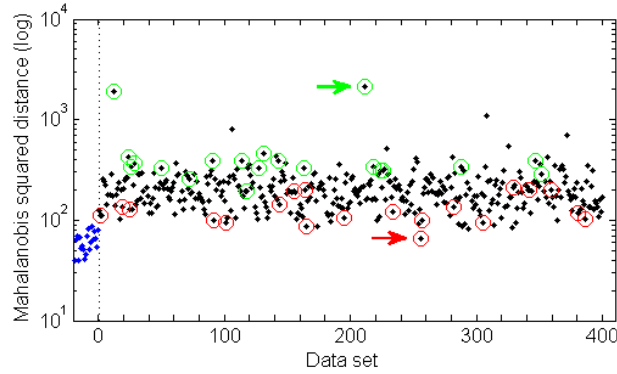


Figure 87: Mahalanobis distances for feature vectors defined with the standard deviations of Segment #1-#64 (blue dots: experiments, black dots: simulations, red circles: runs with lowest RMS residual errors, green circles: runs with highest RMS residual errors).

Figure 88 shows three of the feature vectors used to calculate the Mahalanobis distances of Fig. 87. Each point is one of the extracted features, that is, the standard deviation of one of the 64 time segments illustrated in Fig. 86. The red solid line is run #N256 with lowest RSME value/Mahalanobis distance; the red dotted line is run #N211 with highest RSME value/Mahalanobis distance. Both feature vectors are compared to that of the experimental data (blue solid line). It is clear that the feature vector from run #N256 shows much better agreement with the experimental data than that from run #N211. The Mahalanobis distance, therefore, is able to identify the feature vectors that correlate better with the experimental measurements.

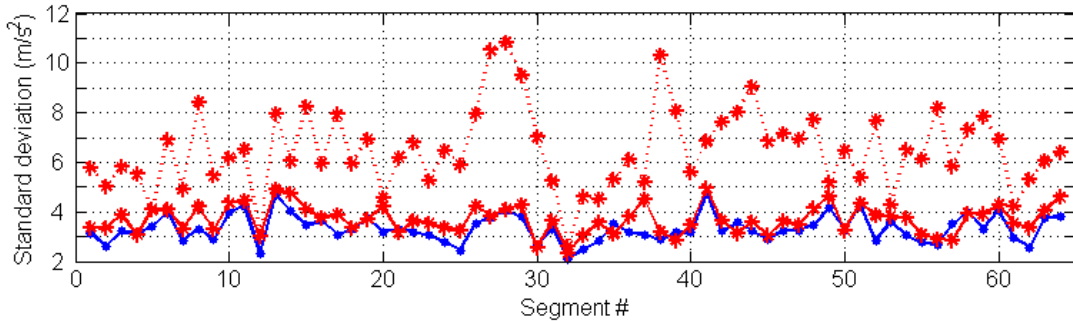


Figure 88: Comparison of feature vectors (blue: experimental measurements, red with a solid line: Run #N256 with the lowest RSME value and Mahalanobis distance, red with a dotted line: Run #N211 with the highest RSME value and Mahalanobis distance.)

Values of the Mahalanobis distance for the Latin hypercube simulation runs in Fig. 87 are different from values obtained with the experimental data, sometimes differing by more than one order of magnitude. A consequence is that, even though the agreement between Mahalanobis distance and RMSE value is overall good, one cannot always rely on the distance measure to identify the most accurate predictions. The main reason is that two of the model parameters considered, Gap and Δ , are strongly correlated in the modeling of the impact behavior.

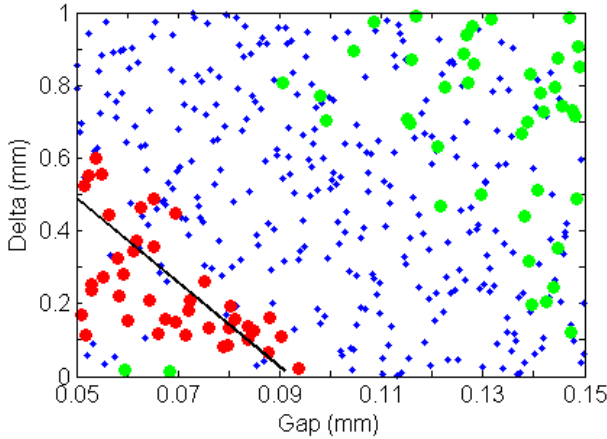


Figure 89: Two-dimensional space of model parameters (Gap ; Δ) sampled by the Latin hypercube design (red dots: accurate models with low RSME values, green dots: inaccurate models with high RMSE values).

Figure 89 is a two-dimensional view of the Latin hypercube design, showing the values of parameters Gap and Δ for the 400 runs of the design. (The third parameter, k_B , is not shown.) The most accurate simulation runs, which are diagnosed by the lowest RMSE values between measured and predicted time-history responses, are indicated by red dots; the least accurate predictions are indicated by green dots. It can be observed that, while the column-to-bumper gap was exactly set to $\text{Gap} = 0.1$ mm in the physical experiments, some of the models defined with smaller values of Gap also give accurate predictions. This happens when small values of Gap are combined with large values of Δ , as indicated by the notional trend (black line) added in the lower left corner of Fig. 89.

This result illustrates that the interaction between uncertain model parameters can be an influential effect in both the numerical modeling and feature selection process. If such an interaction cannot be prevented in the modeling, a recommendation is to select response features that are independently sensitive to different model parameters. Nevertheless, the results obtained confirm, once again, that the Mahalanobis distance comparison method can be effective for statistical model validation, as long as an appropriate set of response features is selected.

7. CONCLUSIONS

This report investigates feature extraction techniques for the Model Validation (MV) of structural dynamics simulation models. Several feature extraction techniques are applied to numerically-calculated and experimentally-measured responses of a test-bed structure. The sensitivity of (output) response features to the (input) model parameters is related to the type of inputs and linearity/nonlinearity of the system. The main findings are summarized below.

- Response features for waveform analysis, such as basic statistics, temporal moments, exponential decays and crest/K-factors, are appropriate to extract overall amplitude, frequency and decay characteristics of time-history signals. It should be noticed that most of these features extract global characteristics of the waveforms; therefore, they are not so useful to validate model parameters that locally affect the responses. Most of these features for waveform analysis are low-dimensional and characterize a single aspect of the time-history response. Effective MV, therefore, necessitates that several response features be combined into a multi-dimensional feature vector.
- The frequency spectrum (e.g., power spectrum, frequency response function) includes all dynamic response information for both linear and nonlinear systems. These features, however, tend to be of high-dimension. Therefore, additional processing is needed to extract low-dimensional metrics for quantitative comparisons.
- Some features based on frequency-domain analysis (e.g., cepstrum, Holder exponent) can characterize singular phenomena that occur in certain types of nonlinear systems. They are expected to be suitable to compare the behaviors of other dynamic systems exhibiting similar types of nonlinearities.
- Parameters and residual errors of estimated time-series models, such as the families of AR, ARX, ARMA, AR-ARX models, are also expected to define effective features to compare measured and predicted time-history responses. These features exhibit significant sensitivities, especially to the degree of nonlinearity represented by impact events in the measurement and prediction of the test-bed structure response.
- The sources of response variability encountered during experimental testing can be different from those of numerical modeling and simulation, which is a challenge for MV. Measurement noise in experimental data is typically random and often with a normal distribution. Systematic bias, such as that coming from instrument calibration error, for example, can also be observed. The variability of numerical predictions, on the other hand, originates from the randomness of model parameters (e.g., input forces, material properties, damping coefficients) as well as systematic errors caused by the mesh discretization and modeling assumptions. The sensitivity of response features to input parameters of the model can be artificially influenced by the procedure used to extract these features from the time-history responses, such as the fitting/estimation algorithms.

Additionally, some procedures for MV and Uncertainty Quantification (UQ) are presented in this report, and their applicability is demonstrated for validation of linear and nonlinear models of the test-bed structure. The conclusions are summarized below.

- Applicability of the Mahalanobis distance comparison method is demonstrated for the linear dynamic system. In particular, the uncertainty of damping parameters can be assessed, and reduced through inference UQ, using feature vectors that collect basic statistics of the time-history responses. It is observed that the Mahalanobis distances of accurate models are distributed within the same range of values as those derived from the experimental measurements. Consistency of this comparison method is also established: the models that provide the lowest Mahalanobis distances give the most accurate predictions of the measured time-history responses.
- UQ and model calibration procedures based on Bayesian inference are presented for the linear system. The posterior distribution of uncertain model parameters is shown to be informative in terms of understanding the most appropriate values of parameters that yield accurate predictions. Model predictions, for example, obtained using mean (average) values of the posterior distribution accurately reproduce the measurements.
- Several difficulties encountered in the validation of the nonlinear model are discussed. Feature selection is essential to identify characteristics of the predicted response that are sufficiently sensitive to model parameter variations. This result is especially important for the nonlinear system. We observe that interactions between different parameters of the nonlinear model make it difficult to unambiguously identify validated models using the Mahalanobis distance comparison method. A recommendation is to work with response features that are each sensitive to different model parameters.

To achieve effective MV using appropriately selected features, the data acquisition is another important issue. Physical experiments should be well-enough controlled so that the analyst developing the simulation model can understand the system linearity, type of inputs, signal stationarity, and noise characteristics of the measurements. Conversely, the experimentalist should understand the objectives of validation, specifically, the initial and boundary conditions that need to be imposed during testing, and the response types that need to be measured. Because data acquisition is plagued with practical limitations (e.g., controlling the input, sensor configuration), especially when it is applied to large-scale structures such as civil engineering structures, acquiring meaningful data for MV becomes a significant challenge.

Finally the modeling strategy is mentioned as another potential difficulty. We show that an effective strategy for feature selection is to include response features that are sensitive to independent model parameters. At the same time, however, the model itself should be developed to describe as many different attributes of the dynamic system response as possible. These two objectives might be antagonistic. Hence, the relationship between feature selection and modeling strategy will become a significant topic in future work.

8. BIBLIOGRAPHY

- Alexander, J. E. (2009). Shock Response Spectrum – A Primer, *Sound and Vibration*, June, pp.6-14.
- Allemand, R.J. (2003). The Modal Assurance Criterion – Twenty Years of Use and Abuse,” Sound and Vibration, pp. 14-21.
- Bendat, J. S., and Piersol, A. G. (1980). *Engineering Applications of Correlation and Spectral Analysis*, John Wiley, New York.
- Bishop, C. (1995). *Neural Networks for Pattern Recognition*, Oxford, UK: Oxford University Press Inc.
- Box, G. and Jenkins, G. (1976). *Time Series Analysis: Forecasting and Control*, Prentice Hall, Englewood Cliffs, New Jersey.
- Box, G. E. P., Jenkins, G. M., and Reinsel, G. C. (1994). *Time Series Analysis: Forecasting and Control (3rd edition)*, Prentice Hall, Englewood Cliffs, New Jersey.
- Browman, A. W. (1984). An Alternative Method of Cross-validation for the Smoothing of Density Estimates, *Biometrika*, 71, pp. 352-360.
- Butler, T., Doebling, S., Hemez, F., and Sohn, H. (2001). Model Validation For a Complex Jointed Structure. *19th IMAC, International Modal Analysis Conference*. Kissimmee, FL.
- Chambers, J., Cleveland, W., Kleiner, B., and Tukey, P. (1983). *Graphical Methods for Data Analysis*, Wadsworth International Group, Belmont, CA.
- Clough, R. W., and Penzien, J. (1993). *Dynamics of structures, 2nd edition*. New York, McGraw-Hill.
- Doebling, S. W., Farrar, C. R., Prime, M. B., and Shevitz, D. (1996). *Damage Identification and Health Monitoring of Structural and Mechanical Systems from Changes in their Vibration Characteristics: A Literature Review (LA-13070-MS)*, Los Alamos, NM: Los Alamos National Laboratory.
- Draper, N.R. and Smith, H. (1998). *Applied Regression Analysis*, Wiley Inter-science.
- Everitt, B.S. (2002). *The Cambridge Dictionary of Statistics (2nd edition)*, Cambridge University Press.
- Farrar, C. and Worden, K. (2013) *Structural Health Monitoring A Machine Learning Perspective*, John Wiley and Sons, Ltd.
- Farrar, C., Worden, K., Todd, M., Park, G., Nichols, J., Adams, D., Bement, M., and Farinholt, K. (2007). *Nonlinear System Identification for Damage Detection (LA-14353)*. Los Alamos, NM: Los Alamos National Laboratory.

Feldman, M. (2011). Hilbert transform in vibration analysis, *Mechanical Systems and Signal Processing*, 25(3), pp. 735-802.

Figueiredo, E., Figueiras, J., Park, G., Farrar, C. R. and Worden, K. (2011). Influence of the Autoregressive Model Order on Damage Detection. *Computer-Aided Civil and Infrastructure Engineering*, 26: 225-238.

Figueiredo, E., Park, G., Figueiras, J., Farrar, C., and Worden, K. (2009). *Structural Health Monitoring Algorithm Comparisons Using Standard Datasets (LA-14393)*. Los Alamos, NM: Los Alamos National Laboratory.

Fisher, R.A. (1970). *Statistical Methods for Research Workers*, MacMillan, 14th Edition.

Fukunaga, K. (1990). *Introduction to Statistical Pattern Recognition*. San Diego, CA: Academic Press.

Gilks, W.R. (1996). *Markov Chain Monte Carlo in Practice*, Chapman and Hall, New York.

Hannan, E. J., and Kavalieris, L. (1984). A method for autoregressive-moving average estimation. *Biometrika*, 71(2), 273-280.

Hanson, K., Cunningham, G., and Saquib, S. (1998). Maximum Entropy and Bayesian Methods. In *Inversion Based on Computational Simulations*. Dordrecht, Germany: Kluwer Academic.

Hasselman, T.K., Anderson, M.C., Wenshui, G. (1998). Principal Components Analysis for Nonlinear Model Correlation, Updating and Uncertainty Evaluation, *16th SEM International Modal Analysis Conference*, Santa Barbara, California, Feb. 2-5, pp. 664-651.

Hedayat, A., Sloane, N., and Stufken, J. (1999). *Orthogonal Arrays: Theory and Applications*. New York, NY: Springer-Verlag.

Hemez, F., and Doebling, S. (2000). 25th ISMA, International Conference in Noise and Vibration Engineering. *Inversion of Structural Dynamics Simulations: State-of-the-art and Orientations of the Research*, (pp. 403-413). Leuven, Belgium.

Higdon D., Gattiker J., Williams B., and Rightley M. (2008). Computer Model Calibration Using High-Dimensional Output, *Journal of the American Statistical Association*, 103, 570-583.

Holger, K., and Schreiber, T. (1997). *Nonlinear Time Series*. Cambridge, U.K.: Cambridge University Press.

Hotelling, H. (1933). Analysis of Complex of Statistical Variables into Principal Components, *Journal of Educational Psychology*, Vol. 24, pp. 417-441 and pp. 498-520.

Hylok, J., Rutherford, A., Maupin, R., Anderson, M., and Groethe, M. (2005). Validation of a Threaded Assembly, Part II: Experiments, *6th European Conference on Structural Dynamics*, Paris, France, September 5-7, 2005.

Kennedy M., O'Hagan A. (2000). Predicting the Output From a Complex Computer Code When Fast Approximations are Available, *Biometrika*, 87, 1-13.

Kleijnen, J.P.C. and Sargent, R.G. (2000). A Methodology for Fitting and Validating Meta-models in Simulation, *European Journal of Operational Research*, Vol. 120, pp. 14-29.

Liu, C., and Goetichius, G. (2001). Estimation Of Damping Loss Factors By Using The Hilbert Transform And Exponential Average Method, *SAE Technical Paper 2001-01-1408*, 2001, doi:10.4271/2001-01-1408.

Mahalanobis, P.C. (1936). On the Generalised Distance in Statistics, *Proceedings of the National Institute of Sciences of India*, Vol. 2, No. 1, pp. 49-55.

Maia, N. M. M., and Silva J. M. M. (1997). *Theoretical and Experimental Modal Analysis*, John Wiley and Sons.

Maupin, R., Hylok, J., Rutherford, A., and Anderson, M. (2005). Validation of a Threaded Assembly, Part I: Overview, *6th European Conference on Structural Dynamics*, Paris, France, September, 2005.

Mayne, D. Q., and Firoozan, F. (1982). Linear identification of ARMA processes. *Automatica*, 18(4), 461-466.

McKay, M. (1999). Sampling Variability of Measures of Input-Variable Importance in Computer Models. *3rd DOE/MICS Workshop on the Predictability of Complex Phenomena*. Los Alamos, NM.

McKay, M., Beckman, R., and Conover, W. (1979). A Comparison of Three Methods for Selecting Values of Input Variables in the Analysis of Output From a Computer Code. *Technometrics*, 21 (2), 239-245.

Mitchell, J.S. (1993). *Introduction to Machinery Analysis and Monitoring*, PenWel Books, Tulsa, OK.

Mollineaux, M., Van Buren K., and Hemez, F. (2011). Simulating the Dynamics of Wind Turbine Blades: Part I, Model Development and Verification, *13th AIAA Nondeterministic Approaches Conference*.

Montgomery, D.C. (1996). *Introduction to Statistical Quality Control (3rd edition)*, John Wiley and Sons, Inc., New York.

Mottershead, J., and Friswell, M. (1993). Model Updating in Structural Dynamics: A Survey. *Journal of Sound and Vibration*, 162 (2), 347-375.

Mulville, D.R. (1999), Pyroshock Test Criteria, *NASA Technical Standard Report NASA-STD-7003*.

Myers, R.H. and Montgomery, D.C. (1995). *Response Surface Methodology: Process and Product Optimization Using Designed Experiments*, Wiley Inter-science, New York.

Naeim, F., and Kelly, J. (1999). *Design of Seismic Isolated Structures: From Theory to Practice*, John Wiley and Sons.

NASA (1996). Loads Analyses of Spacecraft and Payloads, *NASA Technical Standard Report*, NASA-STD-5002.

Nessus. (1996). *NESSUS, User's Manual, Version 2.3*. San Antonio, TX: Southwest Research Institute.

Neyman, J., and Pearson, E. (1933). On the Problem of the Most Efficient Tests of Statistical Hypotheses. *Philosophical Transactions of the Royal Society, Series A*, 231, 289-337.

Oppenheim, A. V. and Willsky, A. S. (1997). *Signals and systems*. Prentice-Hall.

Randall, R. B. (2011). *Vibration-based condition monitoring: industrial, aerospace and automotive applications*. John Wiley and Sons, New York.

Rebba, R., Mahadevan, S. (2006). Validation of Models with Multivariate Output, *Journal of Reliability Engineering and System Safety*, Vol. 91, No. 8, pp. 861-871.

Red-Horse, J., Paez, T., Field, R., and Romero, V. (2000). *Non-deterministic Analysis of Mechanical Systems, Report #SAND2000-0890*,. Albuquerque, NM: Sandia National Laboratories.

Richardson, M. H., and Formenti D. L. (1982). Global Curve-Fitting of Frequency Response Measurements using the Rational Fraction Polynomial Method, *Proceedings of the 3rd International Modal Analysis Conference*, Orlando, FL (Bethel, Conn., USA: Society for Experimental Mechanics), pp.390-397.

Ripley, B. D. (1996). *Pattern Recognition and Neural Networks*. Cambridge, UK.: Cambridge University Press,.

Robertson, A. N., Farrar, C. R. and Sohn H. (2003). Singularity Detection for Structural Health Monitoring using Holder Exponents, *Mechanical System and Signal Processing*, 17 (6), pp. 1163-1184.

Rutherford, B. (1999). A Re-sampling-based Approach to Optimal Experimental Design for Computer Analysis of a Complex System. *3rd DOE/MICS Workshop on the Predictability of Complex Phenomena*. Los Alamos, NM.

Rutherford, A., Maupin, R., Hylok, J., and Anderson, M. (2005). "Validation of a Threaded Assembly, Part III: Validation," *6th European Conference on Structural Dynamics*, Paris, France, September 5-7, 2005.

Saltelli, A., Chan, K., and Scott, M. (2000). *Sensitivity Analysis*, John Wiley and Sons.

Silverman, B. W. (1986). *Density Estimation for Statistics and Data Analysis*, Chapman and Hall, New York.

SHMTools website: <http://institute.lanl.gov/ei/software-and-data/SHMTools/>

Smallwood, D. (1994). Characterization and simulation of transient vibrations using band limited moments. *Journal of Shock and Vibration*, 1(6), 507–527.

Sohn, H., Farrar, C., Hunter, N., and Worden, K. (2001). Applying the LANL Statistical Pattern Recognition Paradigm for Structural Health Monitoring to Data from a Surface-Effect Fast Patrol Boat (LA-13761). Los Alamos, NM: Los Alamos National Laboratory.

Van Buren K., Mollineaux, M., and Hemez, F. (2011). Simulating the Dynamics of Wind Turbine Blades: Part II, Model Validation and Uncertainty Quantification, *13th AIAA Non-deterministic Approaches Conference*.

Walpole, R. E., Myers, R. H., Myers S. L., and Ye K. (2012). *Probability and Statistics for Engineers and Scientists* (9th Edition), Prentice Hall, Boston, MA.

Weaver, W. Jr., and Johnston, P. R., (1987). *Structural Dynamics by Finite Element*. New Jersey, Prentice-Hall, Inc.

Wirsching, P. H., Paez, T. L., and Ortiz, K. (1995). *Random vibrations: theory and practice*. John Wiley and Sons, New York.

Worden, K., Manson, G., Fieller N.R.J. (2000). Damage Detection using Outlier Analysis, *Journal of Sound and Vibration*, 229 (3), 647-667.

This report has been reproduced directly from the best available copy. It is available electronically on the Web (<http://www.doe.gov/bridge>).

Copies are available for sale to U.S. Department of Energy employees and contractors from:
Office of Scientific and Technical Information
P.O. Box 62
Oak Ridge, TN 37831
(865) 576-8401

Copies are available for sale to the public from:
National Technical Information Service
U.S. Department of Commerce
5285 Port Royal Road
Springfield, VA 22161
(800) 553-6847

